THE UNIVERSITY *of* EDINBURGH

High-Pressure Studies of Ammonia Hydrates

Craig W. Wilson

Doctor of Philosophy
The University of Edinburgh
October 2013

Abstract

Ammonia and water are major components of many planetary bodies, from comets and icy moons such as Saturn's Titan to the interiors of the planets Neptune and Uranus. Under a range of high pressures and/or low temperatures known to occur in these planetary bodies, ammonia and water form a series of compounds known as ammonia hydrates. Ammonia and water form three stoichiometric compounds, ammonia hemihydrate, ammonia monohydrate and ammonia dihydrate, which have ammonia-to-water ratios of 2:1, 1:1 and 1:2 respectively. Therefore a good understanding of the three stable ammonia hydrates is required for modelling the interiors of these bodies.

Additionally, the ammonia hydrates are the simplest systems to incorporate mixed (N-H$\cdots$O and O-H$\cdots$N) hydrogen bonds. Such bonds are important biochemically, and along with O-H$\cdots$O H-bonds, mixed H-bonds are responsible for the second-order structure of DNA, and they are also responsible for the proton transfer reactions in enzymic processes. The understanding of these bonds and processes rests on the knowledge of the relationship between bond strength and geometry, and the ammonia hydrates provide a rich range of geometries against which models of such mixed H-bonds can be tested.

X-ray and neutron diffraction techniques have been used to investigate the behaviour of the ammonia-water complex and further the understanding of this system. This includes solving the structure of a phase which was previously thought to be an ammonia monohydrate phase, but has been shown here to be a mixture of an ammonia hemihydrate phase and Ice VII. In addition to this, x-ray and neutron diffraction experiments have been performed to explore how this phase behaves under changing pressure and temperature conditions, and what other implications that this has on the ammonia-water system. It has been found that ammonia hemihydrate can also form a structural phase observed to form in both ammonia monohydrate and ammonia dihydrate within the same pressure

and temperature regime, which opens the possibility of a solid solution existing between all three stoichiometric ammonia hydrates.

Lay Summary

Ammonia and water can form several solid compounds known collectively as ammonia hydrates. These hydrates form under high pressures, pressures which are many thousand times higher than atmospheric pressure, and/or low temperatures. These conditions are the same as the conditions known to occur in the interiors of many planetary bodies such as comets, icy satellites like Saturn's moon Titan, and the planets Neptune and Uranus. Thus the interactions between ammonia and water under a range of pressure and temperature conditions are necessary to make good models of the interiors of these planetary bodies.

Additionally the ammonia hydrates are the simplest systems that have mixed hydrogen bonds. Hydrogen bonds are a type of connection between molecules that have hydrogen atoms in them, like water, which is made up of one oxygen atom and two hydrogen atoms. Mixed hydrogen bonds are hydrogen bonds that connect molecules which are different, such as ammonia and water. Bonds like these are important biochemically, and are partially responsible for the structure of DNA as well as determining how other biological processes operate. Understanding these bonds and processes rests on an understanding of the relationship between bond strength and geometry, and the ammonia hydrates provide a rich range of geometries against which models of such mixed hydrogen bonds can be tested.

The work presented here will aim to further the understanding of the ammonia hydrates, investigating the structures formed by one of these hydrates, ammonia hemihydrate, which contains twice as much ammonia in its structure as water. This structural information is gathered through a process known as diffraction, where radiation is focused on the material to discover the location of every atom within it. Both x-ray and neutron radiation are used in this work as probes, and data gathered by these diffraction techniques are discussed and analysed, as these two different probes give complementary information. This has resulted in finding a new phase of ammonia hemihydrate, along with more information on

how this phase relates, not just to this specific ammonia hydrate, but the other types of ammonia hydrate as well, giving a clearer picture of what is happening in the interiors of icy planets and satellites.

Declaration

I declare that this thesis was composed by myself, that the work contained herein is my own except where explicitly stated otherwise in the text, and that this work has not been submitted for any other degree or professional qualification except as specified.

Parts of this work have been published in [1], this published work forms the basis for Chapter 5.

Signed:

Acknowledgements

I would like to thank the people who have helped me over the years, without whom my thesis would not have reached completion. Firstly I would like to thank my Ph.D. supervisor, John Loveday, for teaching me most of what I know now about experimental hard condensed-matter physics, and being a constant source of support and advice. I would also like to thank Craig Bull for teaching me everything I know about running a successful experiment at central facilities, and most recently, for invaluable feedback on my thesis as is was being written. I would also like to thank Dan Amos, Mary-Ellen Donnelly, Chris O'Neill and Elise Allthorpe-Mullis, who have all helped in the data collection process at various different experiments over the years.

I would also like to thank several friends who have given me valuable support over the years, which has allowed me to reach this point in more or less one piece. I would like to thank Graham Stinton and Donna Morton for being excellent friends who gave me great support when I really needed it. Also I'd like to thank Emma McBride and Dave Mountford who both always made sure that I left my flat for something other than work, and keeping my spirits up through long working weeks. There are several other people that I have met and worked with over the years that have also helped me invaluably, too many to name individually, and I'd like to thank them all as well, I am sure that they all know that I appreciate everything they have done for me.

I would like to thank the CM-DTC, and EPSRC for funding my Ph.D. Without the financial support provided by them I would not have reached this point, and I am very grateful. I would also like to thank the STFC and the Diamond Light Source for awarding me beam time to collect the data presented in this thesis.

Finally I would also like to thank my family, as they have always been there when I have needed them, and I hope they know that I would never have been able to get this far without them.

Contents

List of Figures

List of Tables

Chapter 1

Introduction and Literature Review

1.1 Introduction

Ammonia and water are some of the simplest molecules that form hydrogen bonds. The study of both of these molecules under a number of different conditions is, therefore, of interest to further the understanding of this fundamental bonding process. Ammonia and water are miscible with one another as liquids and form a series of solid materials known as the ammonia hydrates. These hydrates are of interest scientifically because both ammonia and water are present in large quantities in the outer solar system forming the interiors of icy satellites, such as Titan and Triton, and are also present in the interiors of the planets Uranus and Neptune. Additionally, ammonia hydrates contain mixed hydrogen bonds, hydrogen bonds between different species of molecules, and are the simplest systems that exhibit such hydrogen bonding. Studying the evolution of such hydrogen bonds as pressure is applied to them in these relatively simple systems will therefore form a useful basis for the study of more complicated systems with mixed hydrogen bonding, such as DNA. This will all be looked at in more detail later in this chapter.

In this thesis, a high-pressure study of the ammonia hydrates will be presented, looking at the structures formed under several pressure and temperature conditions, and the transitions between them. These structures and transitions have been probed through the process of diffraction, the mathematical basis for which will be addressed in Chapter 2, along with the practical ways in which structures

are solved. Chapter 3 will look at how two different diffraction probes, x-rays and neutrons, are produced as well as their relative merits. Chapter 4 will look at some of the experimental equipment necessary for conducting high-pressure experiments and how samples are prepared. Chapters 5, 6 and 7 will present the data collected as part of this work along with the data analysis and interpretation of the results of the experimental work, and finally Chapter 8 will present the conclusions that can be drawn from this work.

This chapter will briefly introduce the hydrogen bond and its importance before looking at both ammonia and water, and what is known about them as separate systems. A brief overview of planetary bodies and DNA, two areas where knowledge about the ammonia-water system will be of direct interest, will be presented. Finally a review of the previous studies conducted on mixed ammonia and water systems will be looked at in depth.

1.2 The Hydrogen Bond

A hydrogen bond is a chemical bond that can exist between two separate molecules, or within the same molecule, that contains both a covalently bonded hydrogen atom (A–H) as a "donor" and another "acceptor" atom (B) which has an electron lone-pair or polarisable π electrons. This bond is expressed as A–H$\cdots$B [3]. In the "donor" the electron distribution is not homogenous, and the electrons are drawn away slightly from the hydrogen atom, leaving it partially unshielded with a slightly positive charge. This partially unshielded hydrogen atom can then interact with the lone-pair electrons from the "acceptor" atom forming a hydrogen bond. Hydrogen bonds are divided into three different categories which represent the various bond strengths that they exhibit. These are known as strong, moderate, and weak hydrogen bonds [3]. Strong hydrogen bonds typically have the shortest distances between the A and B atoms in the system (2.2-2.5 Å) and an A–H$\cdots$B bond angle which is approximately straight (i.e. 180°). Modetate bonds are slightly longer than strong bonds (2.5-3.2 Å) and can have an A–H$\cdots$B bond angles of between 130° and 180°. Finally, weak hydrogen bonds have the longest distances between A and B (3.2-4 Å) and the largest range of bond angles (90° to 150°) [3]. All three classes of hydrogen bond are dependant on the electronegativity of the molecules involved in the bonding. Strong bonds arise from donors that have a deficiency in electron density, i.e. a missing electron giving the overall molecule a positive charge, which leads to further unshielding

of the hydrogen atom and/or an acceptor which has an excess of electrons, which strengthens its interaction with the partially unshielded hydrogen atom, for this reason these bonds are sometimes referred to as ionic hydrogen bonds. Moderate hydrogen bonds are sometimes called normal hydrogen bonds because they are formed from donor and acceptors that are electrically neutral, which means that neither the acceptor nor the donor has has an excess or deficiency of electrons. Finally weak hydrogen bonds have donors where there is very little redistribution of electron density, or acceptors with only π electrons [3].

1.3 Ammonia

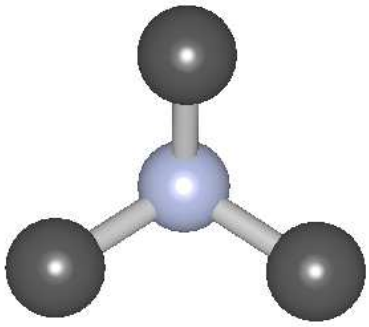

Figure 1.1 *The ammonia molecule. The blue sphere represents a nitrogen molecule, the dark spheres hydrogen or deuterium atoms.*

Ammonia consists of one nitrogen atom and three hydrogen atoms with bond angles of 107.8°. Its main industrial application is in the use of fertilizer for food production. It is also the product of the most wide spread high-pressure synthesis process in the world, the Haber-Bosch process, which generates ammonia for use in fertilizers [4] as well as for other applications. In addition to its importance to food production ammonia is also of fundamental interest scientifically. It is a strong hydrogen bonding acceptor molecule while also being a rather poor hydrogen bond donor [5]. This manifests in weak non-linear hydrogen bonds in both solids and liquids. Ammonia also has six solid phases, the pseudo close packed phase I, the disordered close packed phases II and III, phase IV and the closely related phase V and the superionic phase which has been observed at temperatures over 700 K and pressures above 50 GPa [6].

Of these phases ammonia IV is of particular interest because it exists in the area of the phase space that is relevant to the work presented in Chapters 5, 6 and

7. At 5 GPa and room temperature ammonia IV has an orthorhombic structure with lattice parameters $a = 3.2495(4)$ Å, $b = 5.6576(6)$ Å and $c = 5.3556(5)$ Å with the $P2_12_12_1$ space group [7]. The nitrogen atoms themselves are in a pseudo-hexagonal close packed (hcp) arrangement with the novel hydrogen bond arrangement whereby each lone pair of the nitrogen atoms form a weak bond to three of the deuterium atoms of adjacent ammonia molecules, as also witnessed in ammonia I [8]. The ammonia pressure-temperature phase diagram is shown in Figure 1.2.

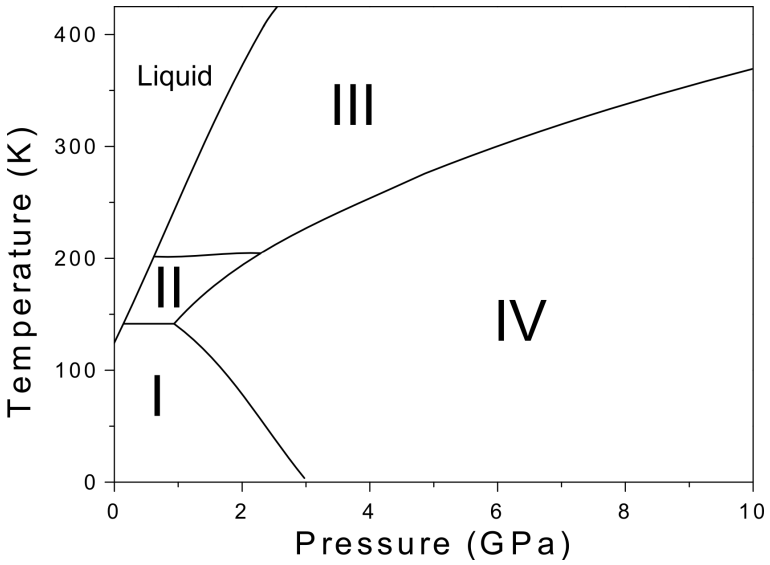

Figure 1.2 *The ammonia phase diagram from 0 to 10 GPa. Adapted from reference [9]*

1.4 Water

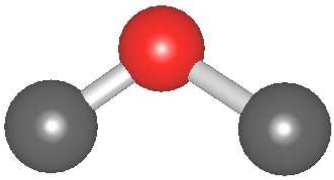

Figure 1.3 *The water molecule. The red sphere represents an oxygen molecule, the dark spheres hydrogen or deuterium atoms.*

Water is another molecule which is abundant in the universe, and consists of one

oxygen atom and two hydrogen atoms with a bond angle of 106.5°. Water has been studied much more extensively at high pressure than ammonia and is known to form strong hydrogen bonds as both the acceptor and donor molecule [10]. There are also many more solid phases of water known compared to ammonia, although not all structures have been structurally characterised. Water, like ammonia, also has a superionic phase [11].

While water is one of the most abundant materials on earth and the solar system it also displays a number of strange properties when compared to other hydrogen containing compounds with atoms close to oxygen in the periodic table (N, C, F) [10]. The melting line for ice at low pressure and temperature is negative, which means the liquid is denser than the solid under these conditions. Above pressures of approximately 1 GPa the phase diagram of ice simplifies dramatically, containing only three solid phases up to nearly 1 MBar (100 GPa), these phases are ice VI, VII and VIII. Of those three phases only two are of particular interest as they exist at similar pressures to the work presented in Chapters 5, 6 and 7. These are the disordered pseudo-bcc ice VII, which is the phase mostly seen at higher temperatures [12], and the phase ice VIII which is its fully ordered counterpart observed at lower temperatures, however there is known to be some considerable hysteresis observed when transitioning between one phase and the other [13]. Figure 1.4 shows the phase diagram for water.

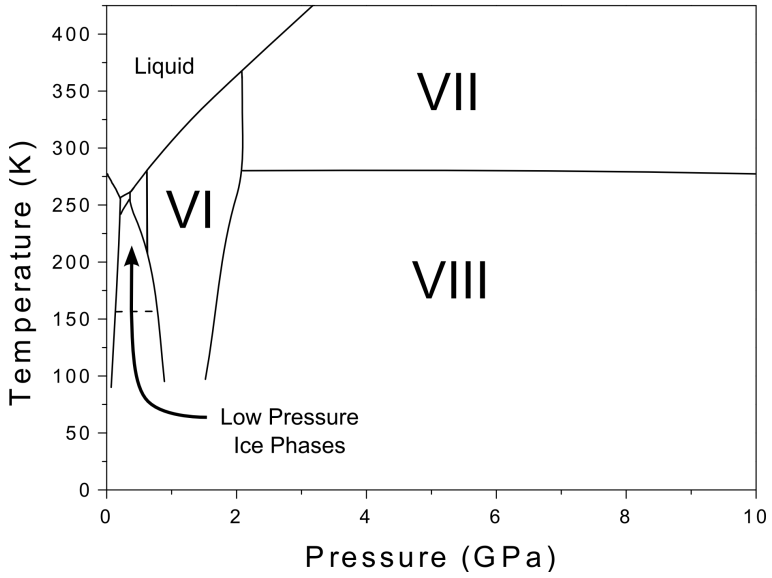

Figure 1.4 *The phase diagram of ice from 0 to 10 GPa highlighting the high-pressure phases VI, VII and VIII. Adapted from reference [14]*

1.5 Titan, Europa, and Other Icy Satellites

Liquid water is integral to the existence of life [15] and it is also found in abundance in the solar system [16]. Europa, a moon of Jupiter, and Titan, a moon of Saturn, are thought to have a liquid water sub surface ocean [17] and are therefore of particular interest. Titan is of interest in particular because not only does it have liquid water present, but it has a mostly nitrogen atmosphere as well as a proportion of methane, which through photochemistry yields much more complicated molecules up to and probably beyond C7 molecules (long-chain hydrocarbon molecules containing 7 carbon atoms) [18, 19]. This is exciting as this means that Titan has all the necessary components for the emergence of life (water, hydrocarbons and energy) [15] and there is also evidence that Titan's atmosphere produces many molecules thought to be important in the chemistry of the early Earth [19, 20].

The presence of methane in the atmosphere of Titan poses other questions that need to be answered. The concentration of methane in the atmosphere is too high, as the gravitational force of Titan is not sufficient to retain its own atmosphere. To explain the abundance of methane observed, there must be a source within the interior to resupply the methane which is lost to space. One model describes three main outgassing periods during Titan's history and formation [21]. This model involves trapping methane in a clathrate under a thin ice layer, which is then periodically released through the surface through cryovolcanism. However, this model does limit the role of ammonia within the interior of Titan to act only to depress the freezing point of water.

Ammonia is thought to have been a major component of Titan at some point of its history. The presence of Titan's nitrogen rich atmosphere is thought to be mainly due to the photolysis of ammonia, which was first captured during the accretion of Titan. This means at some point in the history of Titan the ratio of ammonia to water would have been much higher than at present and the interaction between all three molecular ices would be extremely important in understanding the evolution of Titan from accretion to the present day [22].

1.6 Uranus and Neptune

Uranus and Neptune are two of the largest planets in the solar system and are located at the furthest edge of the solar system. These two planets are sometimes known as the "ice giants" because they both contain large amounts of water and ammonia in their interiors [23]. These two planets produce peculiar magnetic fields when compared to the other planets in the solar system, even compared to the other large gas giants Jupiter and Saturn [24]. Both Uranus and Neptune have magnetic fields dominated by quadrupole magnetic terms rather than the dipole terms that dominate in the other planets in the solar system [16]. The best models that explain these strange magnetic fields in the ice giants require the magnetic dynamo to be generated in a thin shell within the planets [24, 25]. This thin shell is located within the ice layer, and thus the interactions of the major components of the ice layer, ammonia and water, are important for validating whether these models are physically possible.

1.7 Hydrogen Bonding in DNA and other Biological Materials

In addition to liquid water being needed for the existence of life [15], the hydrogen bond also plays an important role in biological processes [26]. DNA is the blueprint of life and is formed from a combination of base pairs held together in a helix through mixed hydrogen bonds [27]. A mixed hydrogen bond is a hydrogen bond between an acceptor atom which is part of one molecule, such as a water molecule, with a donor atom from a different type of molecule, such as an ammonia molecule.

With the recent discovery of bacteria that can live and continue to operate in high-pressure environments [28], understanding how mixed hydrogen bonds evolve under changing pressure environments is required. This can be used as a fundamental basis for understanding these very complicated systems. Such an understanding can be gained from studying the evolution of mixed hydrogen bonds in simpler systems that contain these mixed hydrogen bonds and exist over a large pressure range. One of these simpler systems are the ammonia hydrates, which exhibit mixed hydrogen bonds between ammonia and water molecules.

1.8 Ammonia and Water Mixtures: The Ammonia Hydrates

Ammonia and water along with methane are known as molecular ices. Molecular ices is a term used most extensively in planetary science to refer to these molecules collectively in either pure (single species) or mixed (multiple species) materials which form solids that are less dense and solidify at temperatures much lower than silicates and other rock forming minerals. When ammonia and water are mixed together they form a series of materials known collectively as the ammonia hydrates, with the exact compound being formed depending largely on the ratio of ammonia-to-water in the original sample, as well as the temperature and pressure they are formed at. There are three stoichiometric ammonia-water compounds, ammonia dihydrate (ADH, $NH_3{\cdot}2H_2O$), ammonia monohydrate (AMH, $NH_3{\cdot}H_2O$) and ammonia hemihydrate (AHH, $2NH_3{\cdot}H_2O$).

Under ambient conditions ammonia is miscible in water in concentrations up to 33% volume. This miscibility can be enhanced by cooling the mixture [29]. The miscibility can also be enhanced at higher temperatures by increasing the pressure of liquid samples, and under certain P-T conditions ammonia and water become fully miscible. The situation is very different when it comes to forming solids.

By cooling ammonia solutions of varying concentrations, determined by the weight of ammonia and water in the solution from near zero percent up to pure ammonia, Rupert [30, 31] determined the freezing behaviour of the ammonia-water system as well as observing two eutectic points. At ammonia concentrations of 80.3% and above, pure ammonia tends to freeze out of the liquid. Between 56.5% and 80.3% ammonia concentrations a compound corresponding to a chemical composition of $2NH_3{\cdot}H_2O$, known at the time as ammonium oxide, would freeze out from the liquid. Between approximately 34% and 56.5% concentrations a different compound, with chemical composition $NH_3{\cdot}H_2O$, at the time known as ammonium hydroxide, would crystallise. At concentrations of 34% and less pure ice was observed to crystallise out of the solution. The eutectic points determined by Rupert were at an ammonia concentration of 80.3% between ammonia and ammonium oxide at 179 K, and between ammonium hydroxide and ammonium oxide at an ammonia concentration of 56.5% at 186 K. The eutectic between ice and ammonium hydroxide was not observed by Rupert but from the results published could be approximated to be 153 K [31]. The eutectic formed

between ice and ammonium hydroxide was later observed by both Postma [32] and Elliott [33] separately to be formed at approximately 173 K. Later work by Rollet and Vuillard [34] showed evidence for a further compound, at the time referred to as ammonia dihydrate, that was found to exist near the eutectic point of ammonium hydroxide and ammonium oxide.

Ammonium oxide and ammonium hydroxide were later renamed to ammonia hemihydrate and ammonia monohydrate to better represent their chemical nature and better show their relation to ammonia dihydrate [35]. The low-temperature structure of ammonia hemihydrate and ammonia monohydrate was first measured by Siemons and Templeton [36] with x-ray diffraction using both powder and single crystal techniques. They reported structures for ammonia hemihydrate as orthorhombic with lattice parameters $a = 8.41(3)$ Å and $c = 5.33(2)$ Å and space group *Pbnm*. The structure they reported for ammonia monohydrate was determined to be hexagonal with lattice parameters of $a = 11.21(5)$ Å and $c = 4.53(2)$ Å, but were not able to determine the space group for AMH. Nitrogen and oxygen positions were also determined for the AHH structure and hydrogen positions deduced from bond length and bond angle constraints to make a plausible hydrogen bonding network.

The low temperature AMH structure was revisited by Olovsson and Templeton again with x-ray diffraction [35]. Their measurements revealed that AMH also had an orthorhombic structure with space group $P2_12_12_1$ and lattice parameters $a = 4.51(1)$ Å, $b = 5.587(3)$ Å, and $c = 9.700(5)$ Å. The nitrogen and oxygen positions were determined from the recorded structure factors and again hydrogen positions were deduced from bond angle and length constraints.

Several studies investigating the infrared spectra associated with the above mentioned low temperature structures [37, 38] and investigating proton transport properties of ammonia hemihydrate [39, 40] were conducted by Bertie *et al.* Work by the same group also produced the first structural x-ray study on crystalline ammonia dihydrate [41]. This work, which also recorded the infrared spectrum of ADH, reported a cubic structure with lattice parameter a = 7.118(15) Å with a space group of $P2_13$. From the infrared spectra, bond lengths were obtained and a structure that could potentially fit with the suggested space group and the infrared data was also given.

Loveday and Nelmes [42, 43] also found the structures of ADH-I, AMH-I and AHH-I *via* neutron diffraction with deuterated samples of the three ammonia

hydrates. The structures found agreed with those that had already been reported from x-ray diffraction [35, 36, 40]. However, the hydrogen positions were determined directly from analysis of the data rather than deduced from bond angle and length constraints, as had been done in the earlier x-ray studies. This work showed that the structures of AHH-I and ADH-I both contained significant orientation disorder for some of the molecules in the structure. For AHH-I there was a slight correction to the lattice parameters, where a and b are very similar in length but still unique unlike what was reported previously by Siemons and Templeton [36, 43], the lattice parameters reported in this study were $a = 8.3220(3)$ Å, $b = 8.3526(3)$ Å and $c = 5.2799(2)$ Å. The disorder in one of the ammonia molecules in the structure proposed by Siemons and Templeton was also confirmed, but only over two distinct orientations rather than a freely rotating molecule. The AMH-I phase was found to be exactly the same as that reported by Olovsson and Templeton [35, 43] but with the lattice parameters and atomic positions determined more precisely (lattice parameters $a = 4.51108(14)$ Å, $b = 5.58691(20)$ Å and $c = 9.71452(34)$ Å). ADH-I was found to have a cubic structure as reported by Bertie and Shehata [41, 43] with the more precise lattice parameter $a = 7.1272(8)$Å determined. The structure has the space group $P2_13$ as determined by Bertie and Shehata with disordered hydrogen sites for the water molecules. While Bertie and Shehata reasoned that the hydrogen sites should be ordered, reducing the space group to either orthorhombic $P2_12_12_1$, or monoclinic $P2_1$ [41], this type of ordering was not seen, and models with full hydrogen order produced significantly poorer fits [43]. Fortes *et al.* [44] looked at the potential for ordering in ADH-I, and found the orthorhombic $P2_12_12_1$ structure to be most favourable from *ab initio* density functional theory calculations at temperatures below 140 K, however a neutron diffraction study also performed by Fortes *et al.* [45] could not find any ordering down to a temperature of 4.2 K. This was thought to be due to inhibited kinetics over the time-frame of the experiment, but remains unverified.

1.9 High-Pressure Studies of the Ammonia Hydrates

The first high-pressure studies on solid ammonia hydrates was performed by Nicol and co-workers [46–49] who concentrated on compositions with a water content of 50% and greater. The first high-pressure studies on both ammonia

monohydrate and ammonia dihydrate were performed by Johnson and Nicol [46, 47]. However Cynn *et al.* [48] corrected much of this data, taking into account reactions of the samples with the gasket materials used, revisiting the previous experiments with gold electroplated gaskets. The work by Cynn *et al.* also shows the first evidence of a phase decomposition of ADH at pressure into a mixture of ammonia monohydrate and water ice [48]. Characterisation of samples was achieved primarily by optical observations. However, as a result of the similar optical properties of ADH and AMH [48] distinction between these phases was also determined by their characteristic Raman spectra. Along with these observations, the effects of increasing pressure at different ammonia-water ratios of 1:1 and greater water content were recorded. Data were recorded for ammonia concentrations of 10% up to 50% , and in all of these samples only solid AMH and phases VI and VII of ice were observed either mixed together or in equilibrium with the liquid [48].

Boone and Nicol [49] extended the work already done by Cynn *et al.* and also measured the melting lines of both AMH and ADH. The observed phases were categorised through optical comparison to the known phases of water ice and the ambient-pressure structures of AMH and ADH. While several ADH single crystals were obtained from samples with high water content ($\sim$ 63% - 66%), x-ray data were not obtainable from those samples. Boone and Nicol also were the first to present high pressure data on AMH from a single sample in slight excess of 50% ammonia content producing a melt line curve for AMH. Finally in a sample which was far from an ideal stoichiometry for either AMH or ADH (41% ammonia content) data across a large range of P-T space was recorded. This mapped out the different areas where ADH and AMH were stable, and what phases of ice appeared along side. These data showed clearly for the first time where ADH became unstable and broke apart into a mixture of AMH and ice VIII, while a mixture of AMH and ADH is stable at lower temperatures.

Neither Boone and Nicol or Cynn *et al.* considered the possibility of a phase change from the ambient-pressure low temperature structures in their measurements [48, 49]. However, Hogenboom *et al.* [50] found evidence of high-pressure polymorphs of both ammonia monohydrate and dihydrate and were able to collect very precise volumetric, pressure and temperature data, but only over the range of 0-0.4 GPa. From this, a very accurate melting curve for both the low pressure and high pressure phases of ADH and AMH were able to be determined, and combining their own data with those of Boone and Nicol and Cynn *et al.*,

produced the very first high pressure phase diagram of AMH and ADH which acknowledged this phase change and plotted the transition boundary [50].

1.9.1 High-Pressure Neutron Studies on Ammonia Monohydrate

Loveday and Nelmes [42] were the first to study the structural changes of AMH at high pressure with neutron diffraction techniques. Their study mapped out several areas of P-T space and found several other high-pressure polymorphs of AMH. These five new phases were labelled III, IV, Va, Vb and VI. Va and Vb were noted to have very similar diffraction patterns with minor peak height changes. In addition to this, the low-pressure, low-temperature structures of deuterated AHH, AMH and ADH were also solved from neutron diffraction data, confirming the earlier structures where the hydrogen locations had to be deduced [35, 36, 41]. This was expanded upon in later work [43]. Figure 1.5 shows the results of this work, the melt line is an extrapolation from the work of Hogenboom *et al.* [50] and the lines between the different phases are of one way transitions unless otherwise noted. Significant hysteresis was seen between several of the phases of AMH, with only the transitions between phase I to II and phase II to IV being fully reversible transitions. The direction of observed phase transition is noted by the arrows in Figure 1.5, but these arrows do not represent the pressure and temperatures these transitions occur, only whether they were observed to be reversible or not. The only transition not noted in the figure is the decompression of cold AMH VI to phase II. No transitions were observed between AMH phase III and phase IV, phase Va/Vb and phase VI, phase Va and Vb, or between the liquid and phase III on cooling at 2 GPa [43].

The novel structure of phase VI was also noted and its structure solved in work by the same group [51]. The comparatively simple diffraction pattern arose from a body-centred cubic (bcc) structure where each bcc site had a 50% occupancy of both ammonia and water molecules, which also had orientation disorder of the deuterium atoms in the structure. This phase was determined to be the very first example of a disordered molecular alloy (DMA). AMH VI has a very similar structure to that of ice VII, but with larger lattice constants. The full structure also includes some deuterium occupancy in the $\langle 110 \rangle$ crystal lattice direction as well as the $\langle 111 \rangle$ direction which is the only direction shown in all figures of this structure (see Figure 1.6). The omission of these deuterium atoms in figures of

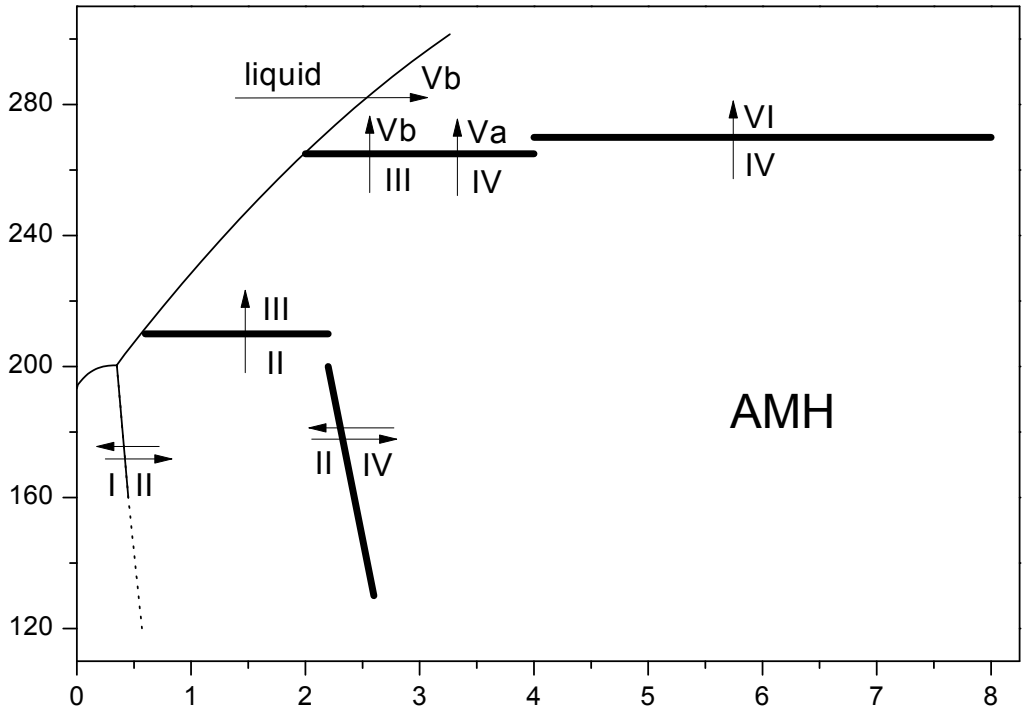

Figure 1.5 *The phase diagram of ammonia monohydrate after Ref. [42]. The melting line is taken from Hogenboom et al. [50] and the lines show the P or T conditions under which the transformations are observed when changing the pressure or temperature. The arrows show the direction in P-T space that the transition was observed, double arrow show reversible transitions. The thicker lines shown are not thermodynamic phase boundaries but simply provide a guide to the conditions under which transformation occurs. The transition between cold AMH-VI to AMH-II is not shown on the diagram.*

the structure in the literature provide a more accessible representation of the structure. It was also noted that, as the structure was disordered, it seemed plausible that samples with any ratio of ammonia to water should be able to form this phase [42].

The crystal structure of ammonia monohydrate phase II was solved by Fortes *et al.* using a combination of computational and Rietveld refinement methods [52]. The unit cell of AMH-II was first determined from previously attained data using the LeBail peak fitting method [53]. This gave starting unit cell parameters, the volume of the unit cell also provided the likely number of AMH formula units contained within, and through analysis of systematic absences, a number of candidate space groups for the structure were also deduced. These parameters

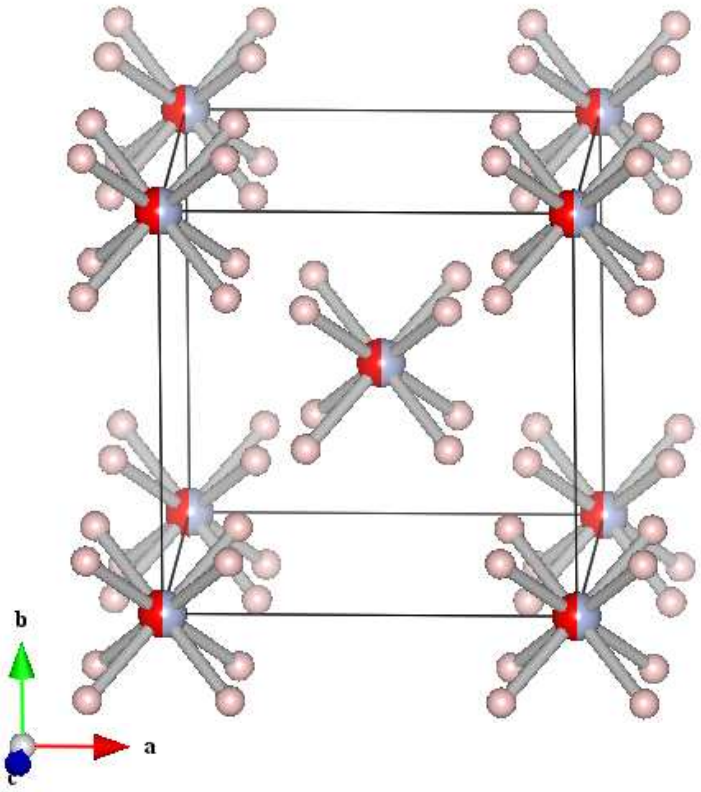

Figure 1.6 *The Disordered Molecular Alloy (DMA) phase of ammonia monohydrate. The central atom in the tetrahedral molecule is a 50/50 split between oxygen and nitrogen, and the hydrogen(deuterium) sites are only partially occupied (see text).*

were then used as inputs for *ab initio* random structure searching (AIRSS). AIRSS is a density functional theory (DFT) method of predicting stable structures of materials developed by Pickard and Needs [54]. AIRSS requires only the number and types of the atoms within the unit cell to be known, firstly relying on a randomly determined unit cell with sensible unit cell volume where the atoms in the structure are then inserted at random before being allowed to relax to hopefully find the structure of lowest energy. Through the combination of both of these processes several candidate structures for AMH-II were then tested against a phase-pure sample, which then allowed the structure to be solved. The structure has the orthorhombic unit cell parameters of $a = 18.8285(4)$Å, $b = 6.9415(2)$Å and $c = 6.8449(2)$Å with the space group *Pbca*. The structure is fully ordered and consists of several tessellated pentagons which was noted to be quite similar to the arrangement also seen in argon clathrate hydrate [52].

The equation of state (EOS) of AMH-I was first measured by Loveday and Nelmes

[43] up to a pressure of ∼2.8 GPa. Their measurements were conducted at 130 K where AMH-I transforms directly into AMH-IV (see Figure 1.5). Their data were fitted with a Murnaghan equation of state fit, with the bulk modulus parameter $K_0 = 8.9(4)$ GPa, and the bulk modulus pressure derivative $K_0' = 4.2(3)$. Here the value of V_0 was not stated explicitly but could be approximated to be close to the volume of the unit cell of AMH-I at ambient pressure. These values were observed to be in fairly good agreement with DFT calculations and preliminary data analysis conducted by Fortes *et al.* [55] on data previously collected by Nelmes *et al.* in a different experiment [56]. Fortes *et al.* revisited the EOS of AMH-I over a lower pressure range (0-0.5 GPa) at a higher temperature (180 K) [57]. Due to a lack of a sufficient number of data points to precisely fit K_0' to their collected data, they preferred to use a fixed value for K_0' determined by their previous *ab initio* DFT calculations [55] which gave a much higher precision on their fitted parameters. The fitted parameters were $V_0 = 248.00(2)$ Å^3, and $K_0 = 7.33(3)$ GPa using a fixed K_0' value of 5.3.

Griffiths *et al.* [58] used AIRSS to attempt to find an energetically stable ionic phase of AMH at low temperatures. The fully ionic structure was predicted to become stable relative to the other known structures of AMH-I and AMH-II from as little as 3 GPa up to approximately 10 GPa depending on the choice of exchange correlation functional. The structure predicted has the orthorhombic space group P4/nmm and lattice parameters $a = b = 5.006$ Å and $c = 3.385$ Å predicted for a pressure of 3 GPa. Comparisons between this predicted ionic phase and the observed but unsolved phases of AMH-III and IV were made, but the ionic structure did not successfully represent any of the known diffraction patterns. A comparison was also made to the structure of AMH-VI, noting that the predicted structure appeared to be an ordered variant of AMH-VI [58]. While they were not able to give a direct computational comparison between the stabilities of their ionic structure and AMH-VI due to the difficulty of modelling a disordered system in their calculations, they did note that it would be very difficult to tell the difference between a disordered molecular and a disordered ionic solid, suggesting that perhaps AMH-VI itself was ionic.

1.9.2 High-Pressure Neutron Studies on Ammonia Dihydrate

A phase-space exploration study on ADH, similar to that already conducted on AMH, was performed by Fortes *et al.* [59]. Their work catalogued three new

phases, ADH III, IV and a body-centred cubic phase that was very similar in structure to that of the DMA AMH VI [51, 59]. Also the dehydration boundary was confirmed through the decomposition of ADH samples into a mixture of AMH V or VI and ice VII or VIII, depending on pressure and temperature, by matching their diffraction patterns or structures to that observed by Loveday and Nelmes [42]. ADH III was later found to be a mixture of AMH II and ice II [60]. Figure 1.7 shows a collection of this information, the black lines show solid phase boundaries, the red lines show areas where both an ammonia-water liquid and solid pure water ice phases can be seen together.

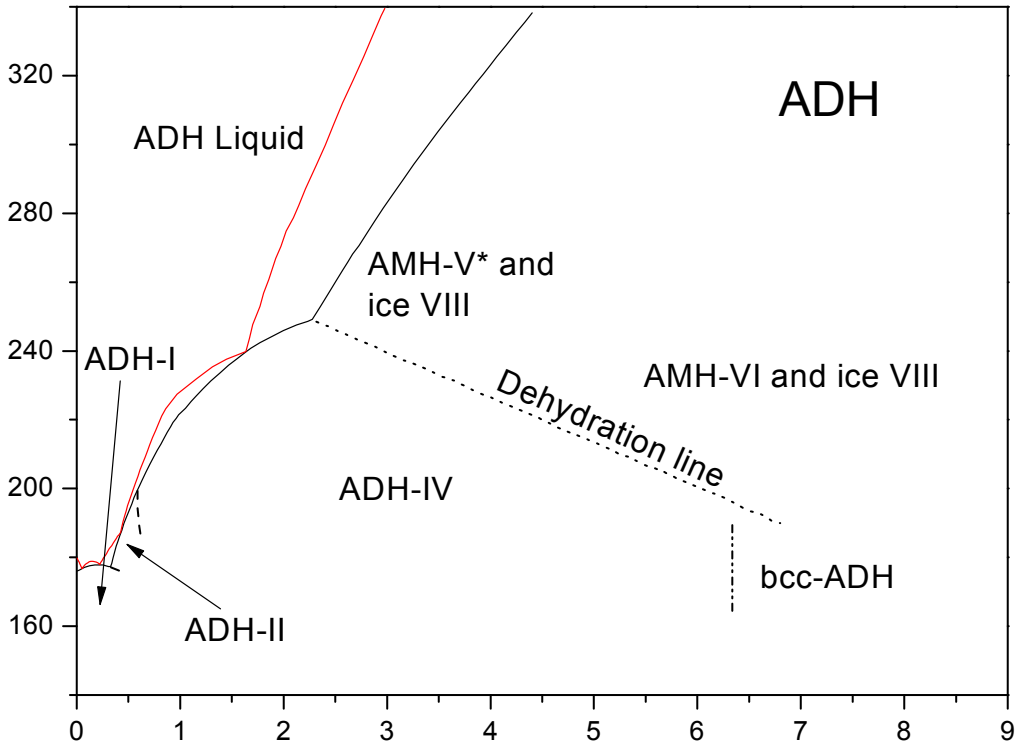

Figure 1.7 *The phase diagram of ammonia dihydrate after Ref. [61]. The diagram has been updated from the source to take into account the fact that Fortes et al. [60] showed that ADH III was a mixture of AMH-II and ice II (see text). The black solid line denotes where the entire sample becomes solid, the red line shows where a solid water ice phase and liquid co-exist, see Fortes et al. [60] for details.*

A cubic phase was observed in one sample in the study by Fortes *et al.* [59] which was determined to have a structure that was very similar to the DMA phase AMH VI. Fortes *et al.* were only able to observe this phase once, but another study by Loveday *et al.* [61] also managed to form this phase of ADH from a low temperature amorphous sample of ADH. Their ADH sample was flash

frozen to a solid from a liquid to prevent decomposition to a mixture of ammonia monohydrate and ice, as had already been observed by Bertie and Shehata [41]. This formed an amorphous solid which then transformed into a bcc phase on warming without decomposing into AMH VI plus Ice VII as was seen by Fortes *et al.* [59]. The room temperature ADH DMA was observed in the presence of other phases [61], these extra phases were thought to correspond to a small amount of Ice VII and a variant of the AMH-Vb structure. This conclusion was reached with comparison of the unfitted peaks to the structures of Ice-VII and Ice-VIII and to the diffraction pattern of AMH-Vb which had been observed previously [42, 43].

The equation of state of ADH-I was also examined both computationally [44] and experimentally [45] by Fortes *et al.* Their computational work, which again was *ab initio* DFT calculations, was also concerned at looking at resolving the issue that the crystallographic structure appears to be cubic [40, 43] while the infrared spectra observes peaks forbidden by cubic symmetry. This was explained by allowing local order which varies dynamically via proton exchange and rotations over the entire crystal lattice. This mechanism allows for both the symmetry breaking observed via infrared spectroscopy [40] and the cubic structure seen with both x-ray and neutron experiments [40, 43]. The equation of state for ADH-I was reported from the experimental work [45] as a third-order Birch-Murnaghan EOS with parameters $V_0 = 365.69(16)$ Å^3, $K_0 = 7.02(25)$ GPa and $K_0' = 10(1)$ for a temperature of 174 K. The large K_0' value was reasoned to be due to the sample being near its melting point and also concluded that at lower temperatures K_0' would have a value much closer to their previously calculated value of 5.44(19) [57, 60].

The crystal structure of ADH-II was investigated in a similar manner to AMH-II by Griffiths *et al.* [62]. Again neutron diffraction data was combined with the AIRSS method to provide a structure for refinement, where the initial unit cell used to constrain the AIRSS run was provided by previous data collected on ADH-II by Fortes *et al.* [60]. The work by Fortes *et al.* found two versions of ADH-II, defining them ADH-IIa and ADH-IIb. These phases were found to have very similar unit cell parameters, and this was hypothesised to be due to a very similar heavy atom (N and O) arrangement while the deuterium positions varied greatly between the structures. These different variants of the ADH-II structure were suggested to arise from the rapid compression of the samples, ADH-IIa forming from melted samples and slow compression through the ADH-I/ADH-II

phase boundary, and ADH-IIb forming through rapid compression through the boundary [60]. The unit cell parameters of phase IIa from Fortes *et al.* and potential space groups deduced from systematic absences were used by Griffiths *et al.* as constraints for running AIRSS. The IIa structure that was preferred had a monoclinic space group of $P2_1/n$ and was fully ordered, and found to agree very well upon Rietveld refinement to the data collected by Fortes *et al.* [62].

1.9.3 High-Pressure Studies on Ammonia Hemihydrate

Ma *et al.* [2] reported two high pressure polymorphs of ammonia hemihydrate at room temperature. Two experiments were performed, one Raman study was carried out on a sample up to 41 GPa and a powder diffraction study up to 36 GPa, both pressures measured with the ruby fluorescence method. Two transitions were reported, one to a bcc phase much like that already seen in AMH and ADH [2, 51, 59, 61] at a pressure of 19.1 GPa, with a further transition observed at the higher pressure of 25.8 GPa. These transitions were observed via discontinuities in both the Raman spectra and the powder diffraction patterns at these pressures. The lower pressure phase was reported as having orthorhombic symmetry with space group *Pnma* from the five visible diffraction peaks, but no lattice parameters were given. The transition to the bcc phase was stated to occur at 19.1 GPa before transforming again to a different phase at 25.8 GPa [2]. However, the peak attributed to the bcc phase does not fully disappear in any of their published powder patterns.

1.10 Concluding Introductory Remarks

The ammonia hydrates have been studied extensively since 1909 [30]. However the system has only been studied at high pressure since 1985 [46]. Since then, many solid phases of both AMH and ADH have been found, and only two identified for AHH. The crystal structures have only been fully solved for a handful of these solid phases; AMH-I, AMH-II, AMH-VI, ADH-I, ADH-II, bcc-ADH and AHH-I. However, there still remains much that is unknown about the ammonia hydrate system, such as the crystal structure of the phase of AMH-V, which is of direct importance to modelling the evolution and interior dynamics of icy planetary bodies such as Titan and Europa. The work presented here is intended

to extend the knowledge about the ammonia hydrate system further through the combined efforts of both neutron and x-ray diffraction studies, as both methods have supplied complementary results on the system so far.

Chapter 2

Diffraction Theory and Structure Determination

The principal methods for determining the crystal structure of a material are based on diffraction. Both x-ray and neutron diffraction operate using the same underlying mathematics. This chapter will set out the mathematical basis of diffraction and describe how crystal structures are derived from data collected using x-ray and neutron diffraction techniques. This chapter will also introduce the different methods of collecting x-ray and neutron diffraction data, and the strengths and weaknesses of these different techniques. Finally this chapter will review some of the different methods of solving structures from the collected diffracted data, and review some of the software used in these methods.

2.1 Crystal Lattices

2.1.1 The Direct Lattice

All crystal structures can be constructed from a lattice, a basis and a space group. A lattice is an array identical and regularly repeated points throughout the entire space that the crystal occupies [63], Figure 2.1 shows an example of a two dimensional lattice. A set of vectors can be defined to allow translation from one point on the lattice any other point on the lattice, these vectors are known as lattice vectors. If there is no set of lattice vectors which can be found that give a

smaller volume between them, then these vectors are known as primitive lattice vectors [64]. An example of primitive lattice vectors are also shown in Figure 2.1.

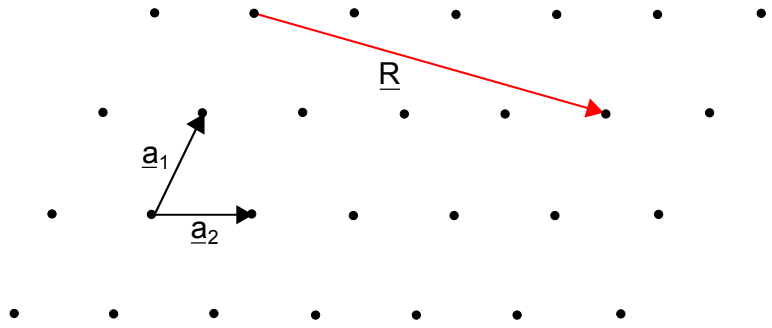

Figure 2.1 *A diagram of a lattice in two dimensions. Vectors* $\underline{a}_1$ *and* $\underline{a}_2$ *are primitive lattice vectors for the reasons highlighted in the text. The red vector* $\underline{R}$ *is a general lattice vector that can be expressed as* $4\underline{a}_2 - \underline{a}_1$

These primitive lattice vectors can then be used to define any vector which points from one lattice point to another as an integer sum of the appropriate primitive lattice vectors. Equation 2.1 gives an example of a general lattice vector $\underline{R}$ expressed as a sum of three lattice vectors $\underline{a}_1$, $\underline{a}_2$ and $\underline{a}_3$ which describe a three dimensional crystal lattice in a similar fashion to the example vectors in Figure 2.1, the scalar quantities x_1 to x_3 are integers [64]. An example of a two dimensional general lattice vector also features in Figure 2.1.

$$\underline{R} = x_1\underline{a}_1 + x_2\underline{a}_2 + x_3\underline{a}_3 \tag{2.1}$$

The lattice describes a series of symmetrically identical points, such that at any of these points the crystal would look identical, the grouping of atoms found at each lattice point is then described through a combination of the basis and the space group [65]. A space group is a theoretical construct of a group of operators that relates the positions of atoms of the same type within the bounds of the primitive lattice vectors [66]. These operators form a closed group. There are only 230 distinct three dimensional space groups [67]. As well as describing the related positions of the atoms within the unit cell the space group have a number of extinction and equivalence conditions that are unique and help determine the space group of a unit cell. Certain reflections will never be seen in diffracted data as a result of the structure having a particular space group, these are known as systematic absences. Some reflections will have the identical reflected intensity which varies depending on space group, these are known as equivalent reflections.

The basis is the smallest number of distinct atoms at distinct locations required to fully describe the layout of the crystal structure. The basis combined with the space group describes the structural arrangement of atoms within a "box" whose edges are defined by the primitive lattice vectors, this box is known as the unit cell of the structure [63, 64]. The unit cell is the element which is repeated across the entire lattice, and for this reason, primitive lattice vectors are also known as basis vectors when referring to the direct lattice. The locations of the basis atoms are usually given in terms of fractional co-ordinates of the basis vectors, and since the unit cell comprises of both the atomic basis, the space group and the lattice vectors, when all parts of the unit cell are known the structure is said to be "solved".

2.1.2 The Reciprocal Lattice

Another, more abstract, construction that is related to the direct lattice is the reciprocal lattice. The reciprocal lattice is defined by direct lattice, and as such, one reciprocal lattice corresponds to one, and only one, direct lattice. If a reciprocal lattice is known, the corresponding direct space lattice is also known and vice versa. This section will show the derivation of the relationship between the reciprocal lattice and the direct lattice, which will be necessary in later sections. The mathematics presented in this section follows that presented in Chapter 6 of Solid State Physics by Ashcroft and Mermin [68], which present an elegant and easy to follow derivation of the reciprocal lattice.

If we consider a general plane wave interacting with a general point in the crystal lattice we can represent this mathematically as $e^{i(\underline{k}\cdot\underline{r})}$. Here $\underline{r}$ is the positional vector of a lattice element defined from the origin and $\underline{k}$ is the wave vector of the general plane wave with arbitrary period, its magnitude being given by $|\underline{k}| = \frac{2\pi}{\lambda}$. While this is rather straight forward, this very general case is not really useful, so instead of considering a plane wave of arbitrary period, consider a plane wave that has a period that is coincident with the identical points in the crystal lattice. What this means is that the plane wave will have a 2π phase shift by the time it reaches the next point in the crystal lattice along its direction of travel. This situation is shown in Figure 2.2. Remembering that this distance between the two lattice points can be described through the general lattice vector $\underline{R}$ this special

plane wave must satisfy the following condition:

$$e^{i(\underline{k}\cdot\underline{r})} = e^{i(\underline{k}\cdot(\underline{r}+\underline{R}))} \tag{2.2}$$

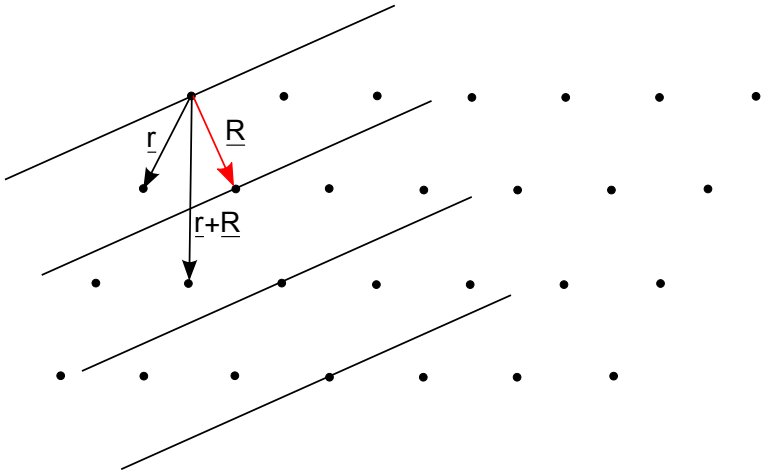

Figure 2.2 *A diagram plane wave incident on a lattice. Here the period of the plane wave coincides with the lattice vector $\underline{R}$ shown in red. This means that any lattice element described by $\underline{r}$ will be identical to the lattice element described by $\underline{r}+\underline{R}$ as shown in the diagram.*

Remembering that $\underline{R}$ is a general vector that can potentially describe any point in an infinite lattice as described in equation 2.1, for each individual $\underline{R}$ there is a wave vector $\underline{k}$ that is associated with it. By replacing the individual wave vector $\underline{k}$ with the general wave vector $\underline{K}$, which is the wave vector associated with the general lattice vector $\underline{R}$ and factoring out $e^{\underline{K}\cdot\underline{r}}$ from equation 2.2 we are left with equation 2.3.

$$1 = e^{i(\underline{K}\cdot\underline{R})} \tag{2.3}$$

By substituting in our definition for $\underline{R}$ from equation 2.1 and representing $\underline{K}$ in a similar fashion ($\underline{K} = y_1\underline{b}_1 + y_2\underline{b}_2 + y_3\underline{b}_3$) we are left with:

$$1 = e^{i(y_1\underline{b}_1+y_2\underline{b}_2+y_3\underline{b}_3)\cdot(x_1\underline{a}_1+x_2\underline{a}_2+x_3\underline{a}_3)} \tag{2.4}$$

And from here it can be shown mathematically that for this condition to hold for the general vectors $\underline{b}_i$ each will have to be related to the primitive lattice vectors

$\underline{a}_i$ in the fashion described in equation 2.5.

$$\begin{aligned}
\underline{b}_1 &= 2\pi \frac{\underline{a}_2 \times \underline{a}_3}{\underline{a}_1 \cdot (\underline{a}_2 \times \underline{a}_3)} \\
\underline{b}_2 &= 2\pi \frac{\underline{a}_3 \times \underline{a}_1}{\underline{a}_1 \cdot (\underline{a}_2 \times \underline{a}_3)} \\
\underline{b}_3 &= 2\pi \frac{\underline{a}_1 \times \underline{a}_2}{\underline{a}_1 \cdot (\underline{a}_2 \times \underline{a}_3)}
\end{aligned} \tag{2.5}$$

These $\underline{b}_i$ vectors describe another lattice, one which the general lattice vector is $\underline{K}$ or the set of plane waves which satisfy the condition in equation 2.3. This lattice is called the reciprocal lattice and depends entirely on the direct lattice that it is derived from [68, 69]. In addition, a rotation of the direct lattice (and hence a rotation of both primitive lattice vectors $\underline{a}_i$ and general lattice vector $\underline{R}$) leads to an identical rotation in the reciprocal lattice.

2.2 Diffraction

The fundamental principle that underpins all crystallographic experiments is the process of diffraction. Diffraction is an effect that occurs when an energy wave passes through a gap with a size comparable to its wavelength. For crystallography however, diffraction is most easily thought of in the Bragg construction. Figure 2.3 shows the Bragg construction of a crystal lattice consisting of several periodic atoms. Through these atoms a series of straight lines can be drawn indicating a collection of identical lattice planes at a distance d apart, known as Bragg planes [70]. Radiation that is incident on these planes is diffracted back out with the same angle as the incident beam. Constructive interference can occur between these incident beams if and only if the path difference between the rays reflected by the different lattice plane are and integral number of wavelengths. This is the Bragg condition, also known as Bragg's law which is shown in equation 2.6. From Figure 2.3 it is quite easy to see that the path difference is $2d\sin\theta$, which has already been substituted in for the path difference in equation 2.6. These points of constructive interference are known as

Bragg peaks.

$$2d\sin\theta = n\lambda \tag{2.6}$$

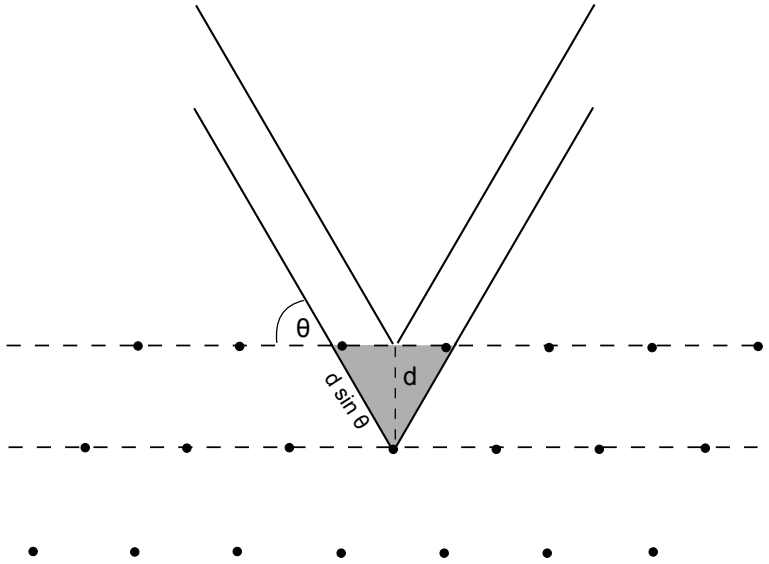

Figure 2.3 *A pictorial representation of Bragg diffraction. The two incident rays diffract from two different planes of atoms. The shaded area shows the extra path length travelled by the lower ray, which is equal to* $2d\sin\theta$

The Bragg construction proves useful for visualization into the diffraction process through its similarity to classical optics where the main difference between the two are that angle θ is measured between the lattice plane and the and the incident beam rather than the normal of the lattice plane and the incident beam as in classical diffraction optics [68]. While this is useful conceptually, it relies on the assumption of the angle of reflection being the same as the angle of incidence, and it also singles out one lattice spacing at a time, while in practical crystallography it is necessary to contemplate several different sets of lattice planes (distinguished by their different separation lengths d). The Laue construction is instead a vector based construction and does not require predefined lattice planes and neither does it assume that the radiation is scattered so that incident and reflected beam have the same angle. It considers the entire crystal to be a series of identical atoms which can allow incident radiation to scatter in all directions, and Bragg peaks only occur at points where the scattered radiation constructively interferes. The mathematics below is again based on the line of argument given by Ashcroft and Mermin [68].

Thinking of an x-ray beam as a combination of several wave vectors, corresponding to separate photons instead of a continuous ray, we can start to pictorially represent the Laue construction as it appears in Figure 2.4. Taking some lattice that these wave vectors are incident on, separated in one direction by distance d and in the other direction by a distance c, the reflected portion of the x-ray beam can only constructively interfere if the path difference between the incident beams is equal to an integral number of wavelengths and that the wavelengths of both scattered and incident wave vectors are the same (i.e. the interaction was elastic and $|\underline{k}| = |\underline{k}'|$). Figure 2.4 shows this situation and again for constructive interference to be observed the path difference between wave vectors $\underline{k}_1$ and $\underline{k}_2$ have to be an integral number of wave lengths leading to equation 2.7.

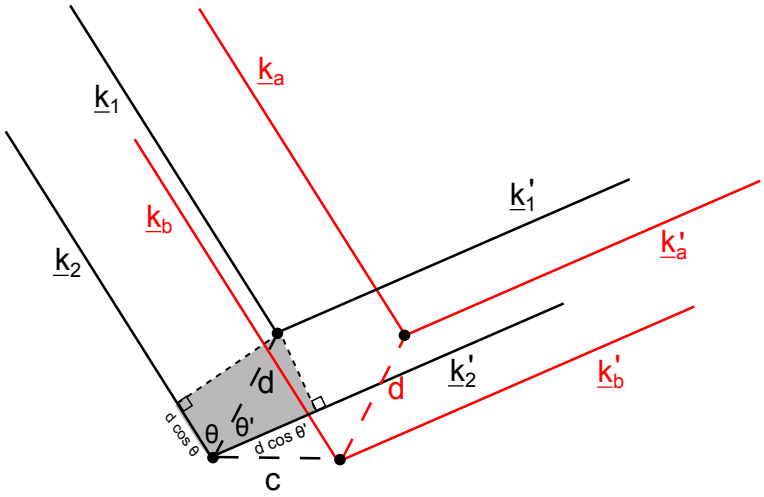

Figure 2.4 *An illustration of the Laue construction. Incident wave vectors $\underline{k}_1$ and $\underline{k}_2$ share the same magnitude and are diffracted at the same angles (giving diffracted wave vectors $\underline{k}'_1$ and $\underline{k}'_2$) a distance d apart. Constructive interference only occurs when the path difference (the shaded grey area) is an integer number of wave lengths. The red vectors $\underline{k}_a$, $\underline{k}_b$, $\underline{k}'_a$ and $\underline{k}'_b$ show the same situation displaced along the lattice by c*

$$d\cos\theta + d\cos\theta' = n\lambda \tag{2.7}$$

This also requires that wave vectors $\underline{k}_1$ and $\underline{k}_2$ arrive in phase with one another, and this means that we can achieve diffraction across every possible in phase pair of incident x-ray photons, as an in phase pair are required for diffraction. The width of the x-ray beam also determines how many of these pairs of scatterers will be illuminated simultaneously. This is in fact a set of separate wave vectors

arriving at the same time t as the other pair, such that these different wave vectors are also contributing to the total scattered beam constructively. Essentially the physical separation of the arriving wave vectors can also be thought of as just a phase separation. Providing all incident wave vectors of the same magnitude arrive at the same time t and the same angle of incidence, constructive interference will occur between all the scattering pairs. One such pair are also illustrated on Figure 2.4 as wave vectors $\underline{k}_a$ and $\underline{k}_b$. The two pairs of wave vectors in Figure 2.4 are just separated by a distance c, which can also just be thought of as a lattice vector. If Figure 2.4 was extended to all pairs of scatterers accessible by the x-ray beam, all will be separated by some general lattice vector $\underline{R}$ providing the distance between the scattering pairs are the same distance d. If we rewrite equation 2.7 in terms of vectors, and remembering that $|\underline{k}| = \frac{2\pi}{\lambda}$:

$$\begin{aligned} \underline{d} \cdot \frac{(\underline{k} - \underline{k}')}{|\underline{k}|} &= n\lambda \\ \underline{d} \cdot \frac{(\underline{k} - \underline{k}')}{\frac{2\pi}{\lambda}} &= n\lambda \\ \underline{d} \cdot (\underline{k} - \underline{k}') &= 2n\pi \end{aligned} \tag{2.8}$$

From Figure 2.4 we can see that d can be thought of as a lattice vector, so equation 2.8 can be generalised for any scattering condition by replacing d with the general lattice vector $\underline{R}$.

$$\begin{aligned} \underline{R} \cdot (\underline{k} - \underline{k}') &= 2n\pi \\ e^{i\underline{R}\cdot(\underline{k}-\underline{k}')} &= 1 \end{aligned} \tag{2.9}$$

The final step in exponentiating the equation is to show the similarity between equation 2.9 and equation 2.3. By comparing these two equations it becomes trivial to see that the Laue construction requires that $\underline{k} - \underline{k}'$ must equal $\underline{K}$, which is a lattice vector of the reciprocal lattice, and is also known as the scattering vector. Looking further into the relationship between the scattering vector and the incident ($\underline{k}$) and reflected ($\underline{k}'$) wave vectors we can see clearly that:

$$
\begin{aligned}
\underline{K} &= \underline{k} - \underline{k}' \\
|\underline{k}| &= |\underline{k}'| \\
|\underline{k}| &= |\underline{k} - \underline{K}| \\
|\underline{k}|^2 &= |\underline{k} - \underline{K}|^2 \\
|\underline{k}|^2 &= (\underline{k} - \underline{K}) \cdot (\underline{k} - \underline{K}) \\
|\underline{k}|^2 &= \underline{k} \cdot \underline{k} - 2\underline{k} \cdot \underline{K} + \underline{K} \cdot \underline{K} \\
2\underline{k} \cdot \underline{K} &= |\underline{K}|^2 \\
\underline{k} \cdot \frac{\underline{K}}{|\underline{K}|} &= \frac{1}{2}|\underline{K}|
\end{aligned} \tag{2.10}
$$

Since the component of the incident wave vector $\underline{k}$ along the scattering vector $\underline{K}$ is exactly half the magnitude of the vector, this means that the triangle formed by the three vectors $\underline{k}$, $\underline{k}'$ and $\underline{K}$ is an isosceles triangle and therefore the scattering angle $\theta = \theta'$ and $|\underline{K}| = 2|\underline{k}| \sin\theta$. This fact means that the Laue and Bragg constructions are equivalent, where Bragg derives from the direct lattice, while Laue derives from the reciprocal lattice.

This also means that the components of the scattering vector $\underline{K}$ is related to the distance between reflecting planes d. This relationship is shown in equation 2.11, which continues on from equation 2.8 remembering that both $\underline{d}$ and $\underline{K}$ point in the same direction.

$$
\begin{aligned}
\underline{d} \cdot \underline{K} &= 2\pi \\
d|\underline{K}| &= 2\pi \\
d &= \frac{2\pi}{|\underline{K}|} \\
d &= \frac{2\pi}{\sqrt{\underline{K} \cdot \underline{K}}}
\end{aligned} \tag{2.11}
$$

This means that the distance separating the Bragg planes d can be expressed in terms of the reciprocal lattice vectors, which relate to the scattering vector as expressed before as $\underline{K} = y_1\underline{b}_1 + y_2\underline{b}_2 + y_3\underline{b}_3$. Hence, the y_i coefficients describe the shortest vector perpendicular to the Bragg planes that are all separated by the distance d and are a characteristic of these reflecting planes. The coefficients

y_1, y_2 and y_3 are conventionally given the labels h, k and l respectively, and are known as the Miller indices of the crystal planes [71, 72]. The Miller indices of the Bragg planes are used to label the reflections observed in a diffraction experiment. For example, a reflection which is later found to correspond to a scattering vector $\underline{K} = \underline{b}_1 + 2\underline{b}_2 + \underline{b}_3$ would be said to be a (121) reflection. The separation d associated with each Miller index, and hence reflection, is also referred to as the reflection's d-spacing.

2.3 The Ewald Sphere and Practical Diffraction Techniques

While the Laue construction is perhaps a little more abstract and less straightforward to grasp intuitively than the Bragg construction with its relation to classical optics, it does lend itself to describing how practical diffraction techniques work more easily. Considering a reciprocal lattice, the scattering vector $\underline{K}$ corresponds to a reciprocal lattice vector from the origin of the system to another point on the reciprocal lattice. As $\underline{K} = \underline{k}_i - \underline{k}_f$, where $\underline{k}_i$ and $\underline{k}_f$ are equivalent to $\underline{k}$ and $\underline{k}'$ in the previous section, it is possible to draw a sphere of radius $|\underline{k}_i|$ so that both the origin and the end of vector $\underline{K}$ are on its surface. This is shown in two dimensions in Figure 2.5.

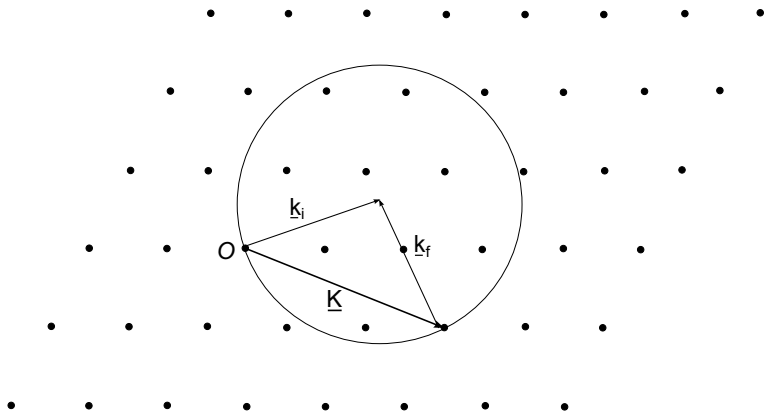

Figure 2.5 *The Ewald Sphere: Here the incident and reflected wave vectors $\underline{k}_i$ and $\underline{k}_f$ are radii for a circle upon which both the origin (O) and end point of scattering vector $\underline{K}$ lies on the surface, represented here in two dimensions*

This gives us another way to state the diffraction condition by stating that diffraction only occurs when both the origin and another reciprocal lattice point

lie on the surface of this sphere. This sphere is known as the Ewald sphere [68, 73]. Typically only one reciprocal lattice point will satisfy this condition for a given $\underline{K}$, as can be seen in Figure 2.5. There are two possible ways to increase the number of reciprocal lattice points that can be observed, and these relate to the two main practical diffraction methods.

First we could change the length of the incident wave vectors, thereby increasing the radius of the Ewald sphere until other reciprocal lattice points satisfy the Laue condition. This means that the incident beam will require either a variable wavelength, or a polychromatic source (several wavelengths incident at once). This is illustrated in Figure 2.6. This is referred to as Laue diffraction [68], and is sometimes called energy dispersive scattering when referring to x-ray diffraction.

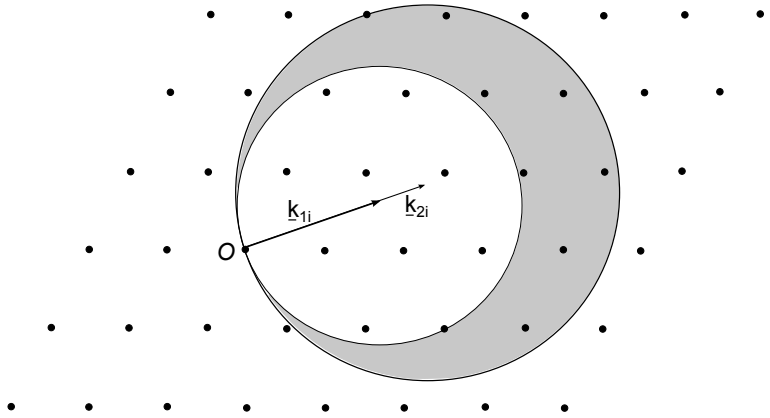

Figure 2.6 *Energy dispersive diffraction: By illuminating the sample with a variety of wavelengths between $\underline{k}_{1i}$ and $\underline{k}_{2i}$, it is possible to satisfy the diffraction conditions for all reciprocal lattice points in the shaded grey area, including those on the surfaces of the spheres.*

Alternatively if a monochromatic (fixed $\underline{k}_i$) source is used, instead the lattice itself can be rotated to bring new reciprocal lattice points into the diffraction condition. This is illustrated in Figure 2.7. To illuminate the largest portion of reciprocal space, a long $\underline{k}_i$ is required, which means a very short wavelength is needed [68]. To bring other reflections into the diffraction condition the sample needs to be rotated about its axis adding to the mechanical complexity of the experiment. This method is known as angular dispersive diffraction.

One alternative to requiring to rotate the sample, is to provide a sample where all possible crystal orientations are present, removing the need to rotate the sample [68]. This is done practically by making a powdered sample, which achieves the orientation homogeneity. While this does remove the need for rotating the

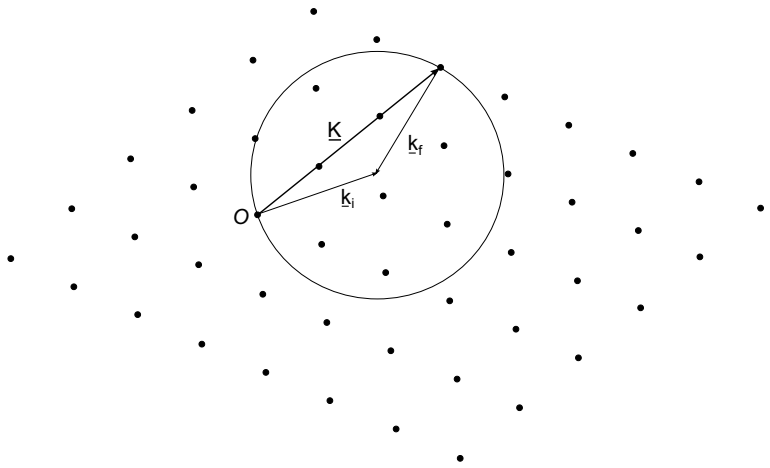

Figure 2.7 *Angle dispersive diffraction: By rotating the lattice new scattering vectors can satisfy the Laue condition using the same* $\underline{k}_i$.

sample, it does remove the relative angular information of the recorded reflections as all scattering vectors that satisfy the diffraction condition are present at the same time. Samples prepared for this method are know as powdered samples, as opposed to single-crystal samples which had been considered for all of the other options above.

For neutron diffraction, while the angular dispersive technique is still viable, there is also the possibility of using a time-of-flight diffraction technique at a pulsed neutron source [74]. The time-of-flight technique is similar to the Laue diffraction method, in that a polychromatic neutron source is used, however the detectors remain fixed at all times. The neutrons are all produced at the same initial time, and the time between this emission and the subsequent detection of the neutron by the detectors is recorded. This information can then be used to reconstruct the corresponding d-spacing of the reflections by calculating the momentum of the detected neutrons. As the mass and the distance travelled by the neutrons are fixed, the De Broglie wavelength of each neutron can be calculated from the momentum. The wavelength of each neutron can then be entered into the Bragg equation to give the d-spacings of the detected reflection.

2.4 Scattered Amplitude

So far the diffracting elements have been assumed to be identical and on the lattice points themselves. However, this is not true for most structures, which

often have several different atoms forming the basis. Every atom within the unit cell will contribute to the total amplitude of the scattered radiation [75]. In the case of x-ray radiation the x-ray is scattered by the electron cloud of the atom, and thus the total scattered amplitude ($F_{\underline{K}}$) of the incident radiation will depend on the electron distribution within the unit cell when diffraction is observed [68]. This can be summed up in the equation 2.12.

$$F_{\underline{K}} = N \int n(\underline{r}) e^{i\underline{K}\cdot\underline{r}} dV = N S_{\underline{K}} \tag{2.12}$$

Where $n(\underline{r})$ is the electron concentration at point $\underline{r}$, and $\underline{r}$ is a point within the unit cell, $\underline{K}$ is the general lattice vector of the reciprocal lattice, N is the number of unit cells illuminated by the x-ray beam and $S_{\underline{K}}$ is known as the structure factor. The electron concentration $n(\underline{r})$ can be further expanded as the sum of contributing electron concentrations of all the atoms in the unit cell, shown in equation 2.13

$$n(\underline{r}) = \sum_{j=1}^{s} n_j(\underline{r} - \underline{r}_j) \tag{2.13}$$

Where s is the number of atoms in the unit cell, n_j is the electron concentration of atom j, which is located at point $\underline{r}_j$, relative to point $\underline{r}$ in the unit cell. Combining equations 2.12 and 2.13, the total scattering factor can be represented as the integral over the unit cell of the contributions of the electron concentrations from all the atoms within the unit cell to the total scattering factor, shown in equation 2.14

$$\begin{aligned} S_{\underline{K}} &= \sum_{j=1}^{s} \int n_j(\underline{r} - \underline{r}_j) e^{i\underline{K}\cdot\underline{r}} dV \\ &= \sum_{j=1}^{s} e^{i\underline{K}\cdot\underline{r}_j} \int n_j(\underline{r} - \underline{r}_j) e^{i\underline{K}\cdot(\underline{r}-\underline{r}_j)} dV \end{aligned} \tag{2.14}$$

The integral now picks out the contribution to the scattering factor over all space of atom j centred at position $\underline{r}_j$. This integral can now be defined as the atomic form factor, f_j, which is an individual property for different atoms, altering the overall amplitude of the scattered x-ray beam, so that the structure factor can

now be written as [68]:

$$f_j = \int n_j(\underline{r} - \underline{r}_j) e^{i\underline{K}\cdot(\underline{r}-\underline{r}_j)} dV$$
$$S_{\underline{K}} = \sum_{j=1}^{s} f_j e^{i\underline{K}\cdot\underline{r}_j} \tag{2.15}$$

In neutron scattering the neutrons are scattered by the atomic nucleus rather than the electron shell of the atom as with x-rays. As a result f_j for neutrons is dependant on interaction with only the atomic nucleus. This interaction does not increase relative to the size of the electron cloud. Instead the f_j's, while still being different from atom to atom, are uncorrelated, and can even have negative scattering factors.

From equation 2.15 it is fairly obvious that $S_{\underline{K}}$ is a complex number. The intensity measured on a detector will be proportional to the square of the amplitude of the incident radiation, and therefore proportional to the square of the structure factor, $I \propto S^*_{\underline{K}} S_{\underline{K}}$, where $S^*_{\underline{K}}$ is the complex conjugate of $S_{\underline{K}}$. This means that for any observed reflection only the real part of $S_{\underline{K}}$ can be measured [68, 75]. This loss of information is known as the phase problem.

2.5 Structure Solutions

Since the phase of the structure factor is unknown, the process of solving a structure involves deducing the phases of the recorded data. There are a number of different methods that can be used to determine the phase of the recorded data and subsequently solve the structure of the material being investigated, and they all rely on determining an initial approximate structure solution [76]. This initial model is used to calculate the expected intensities of relative reflections, which can then be compared to the observed intensities.

Perhaps the simplest method is known as real space methods [77]. This was historically a trial-and-error approach which considered every hypothetical structure allowed by known chemical properties of the sample in question [76]. These models could then be used to compare calculated intensities against the observed intensities of all plausible structures. This method requires significant

investment of time and effort to produce results, and is not generally implemented exclusively. However, recent advances in computing power has lead to the time taken to test each possibility being significantly reduced, and means that trial-and-error methods have again become viable. By implementing Monte-Carlo methods on powerful computers, many randomly determined structures can be quickly tested against observed data, generating several candidate structures.

An alternative to the real space methods are reciprocal space methods, called direct methods, which attempt to determine the phases of the data directly from the measured amplitudes of the structure factor [78]. While the phases and amplitudes of the structure factor are nominally independent it is possible to determine mathematical relationships between the two. For example, the amplitude of the Bragg reflections would be invariant under an origin shift, while the observed phases would change. From this information on the structure where linear combinations of phases that are independent of the choice of origin, which are defined by the space group of the structure, can be obtained. These are known as structure invariants [78]. Additionally a combination of both real space and direct methods can be implemented [79].

The above real space and direct methods approach are viable options for single-crystal samples, where there is no ambiguity in the intensities applied to specific reflections. Powdered samples can see a significant overlap of reflections depending on both the unit cell and space group of the sample in question, along with experimental factors, such as the choice of wavelength of the probing radiation, detector resolution, particle size and sample stresses [80]. As these methods are very different from one another, the next section will describe how these methods are put into practice, and the software that implements these methods will be described.

2.6 Structure Analysis Procedures and Software

To solve a crystal structure in practice requires certain specialist software which will be described in this section. There is a general procedure for structure solution that is true for any diffraction experiment. Firstly the unit cell and space group of the sample needs to be found. This is easier with a single-crystal sample, as each reflection is recorded separately and are not subject to reflection d-spacings overlapping. Once the unit cell has been found, a space group can

then be assigned to the structure that is consistent with the observed reflection conditions. After this a model of the structure can be constructed, either through direct methods or by refining candidate structures to better fit the observed data, and the structure is solved.

2.6.1 Single-Crystal Data Sets

For single-crystal experiments the intensities of each individual diffraction peak needs to be recorded along with the orientation of the sample and detector. The angular information, from the orientation of the sample and detector, can be used to construct the reciprocal lattice, while the intensities of the reflections contain the structural information of the unit cell contents. As discussed in Section 2.1.2, the reciprocal lattice is related to the unit cell, and by finding it the direct lattice can also be determined. Plotting the reciprocal lattice can also be useful, as each recorded reflection should line up on a lattice, any reflections that do not line up with all the other points can then be dismissed as erroneous, and removed before any further analysis takes place. Once the lattice parameters of unit cell of the structure has been determined it can then be used to assign a Miller (hkl) index to all the recorded reflections in a process known as "indexing". The hkl value of all the reflections should be integers, although non-integer indices can provide an idea of how well a unit cell describes a crystal by how close to integer values the indices are. All these calculations can be done through diffraction data analysis sotware, such as the Bruker SMART software [81]. The SMART software displays the intensities recorded on the 2-D detector in a colour display that contrasts the bright spots of the Bragg reflections against the duller background colours, as shown in Figure 2.8. Any sample peaks that appear in the detector need to be "picked" out and the angular information and assosiated d-spacing stored. In this package the reciprocal space visualisation is carried out by a secondary software package in the suite named RLATT [82], where erroneously picked reflections can be excluded easily, as described above. The SMART software can then compute candidate unit cells that can describe all the reflections provided by indexing the cell and refining the lattice parameters by a least squares fit to the data.

Once the unit cell is determined the data can be integrated. This means that all intensity that is associated with a reflection is collected together, as the reflections all have a finite size, and this integrated intensity is the F^2_{obs} for each indexed reflection. One such integration program is called Saint [83]. The index and

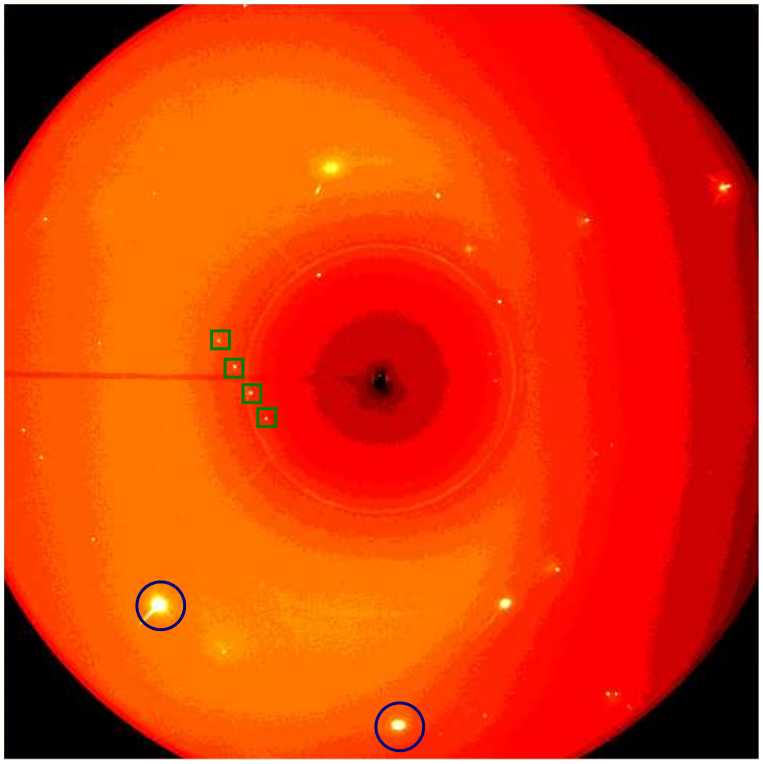

Figure 2.8 *An example of the Bruker SMART detector image display, the dull orange colour shows the background intensity, the lighter coloured spots are Bragg diffraction spots, the most intense spots are larger and closest to white in colour. Black indicates that no intensity has been recorded. In the example display shown here, the smaller peaks like the ones bounded by the green boxes are from the sample, the more intense peaks like the ones bounded by blue circles are caused by diffraction from the much larger diamond anvils.*

intensity of each reflection can then be used to determine the space group using the equivalence conditions and systematic absences as described in Section 2.1.1. While this can be done manually, software such as the XPrep program [84] can be used instead to determine the space group. In addition to checking for systematic absences and equivalences of the indexed reflections XPrep also searches for any higher or lower symmetry space groups that are consistent with the data. XPrep can then output a data file that contains the hkl values of each reflection along with either the intensity (squared structure factor F^2_{obs}) and error in intensity or structure factor ($|F_{obs}|$) and error in structure factor. This data file contains all the information necessary for direct methods approaches as described in Section 2.5. One type of software package that offers the choice of direct methods analysis programs, such as Shelx-97 [85] and SIR-92 [86], for this type of analysis is the WinGX software package [87].

2.6.2 Powder Data Sets

It is also possible to determine a structure solution from powder pattern data. Once the data has been collected, from either an x-ray or neutron instrument the data once again needs to be integrated, like in the single-crystal case. However, the integration procedure is different for powder samples. As the relative angular information of each reflection is lost in powder samples, it becomes impossible to judge the equivalence of reflections with the same d-spacing, making it harder to determine the space group. This is most easily pictured for a monochromatic source and an area detector, where instead of observing a discreet Bragg spot, as in the single-crystal case, a series of concentric rings are observed, as all possible orientations of the sample are observed simultaneously. An example of these powder rings is shown in Figure 2.9. The intensity at each 2θ angle can then be totalled before plotting intensity as a function of 2θ or d-spacing if the radiation wavelength is taken into account, forming a powder "profile". For polychromatic neutron sources, instead of a function of 2θ, the intensity can instead be plotted as a function of time-of-flight producing a powder profile. This can also be plotted as a function of d-spacing.

This integration is normally performed by the instrument software itself, which in the case of Diamond and the ESRF is FIT2D [88], and the PEARL instrument software uses the Mantid software framework [89]. The powder profile, while containing less information than a full single-crystal data set, can still be used to determine unit cell parameters and potential space groups. The d-spacing location of the peaks in the powder pattern can be used to determine the unit cell parameters by iterative searching via algorithms implemented through programs such as ITO, TREOR90 and DIVCOL-04 [90]. After the candidate unit cells have been found, they can be checked against the powder pattern via the LeBail method of profile fitting [53], which allows for further refinement of the unit cell parameters without knowing the structure of the sample by just fitting the peak heights and widths to the expected positions of the intensity peaks from the suggested unit cell and allowing the unit cell parameters to vary to produce a better fit of these peaks to the data.

Analysis of the powder pattern at this stage can be done to determine the space group in a similar fashion to the single-crystal method, once intensities of individual reflections are extracted from the LeBail fit to the data, either through visual inspection or statistical analysis [90]. Once the space group and unit cell

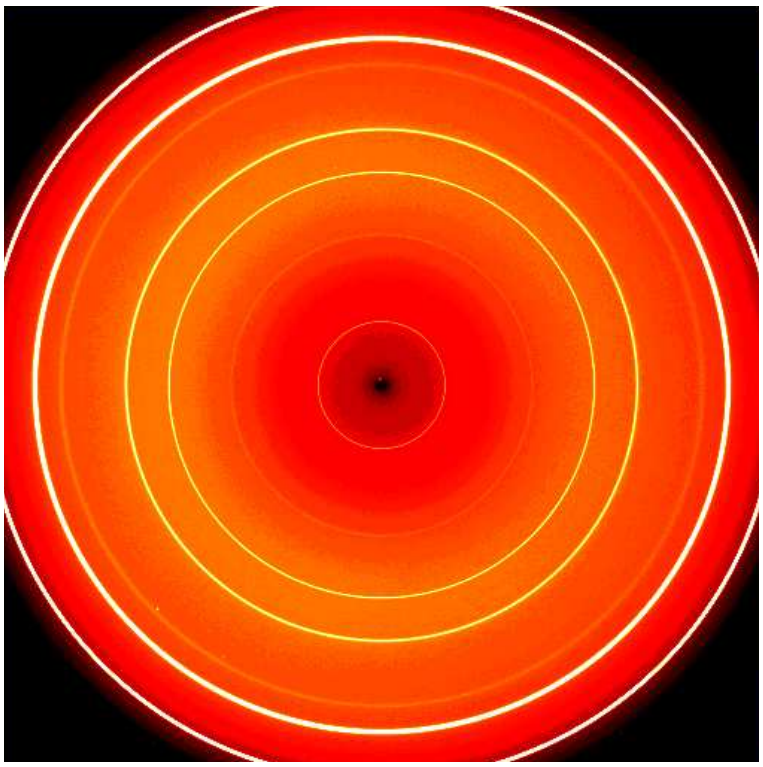

Figure 2.9 *An example of the concentric rings observable from a monochromatic source incident upon a sample, and recorded using an area detector. The intensity observable as a function of distance from the centre of the detector to the edge of the detector should be identical in all directions.*

have been determined, the trial structures can be constructed and tested against the data through Rietveld refinement.

In Rietveld refinement, a candidate structure is proposed in real space, and this is used to produce calculated intensities for that structure, this is compared against the observed data and the minimisation of the differences between the two patterns, observed and calculated, is attempted by least-squares fitting [90]. The GSAS software [91, 92] allows profile matching to powder data via both Rietveld refinement and LeBail methods. Tools are also given to give further profile fitting functions, such as peak shape and thermal parameters of atoms. GSAS also provides several other features such as the ability to impose constraints on certain parameters, introducing rigid bodies to keep some atoms in the trial structures tethered together, soft constraints of bond lengths and angles and damping the changes on parameters imposed by the refinement algorithm to name just a few [91, 92]. An alternative program suite that offers both Rietveld refinement and LeBail profile matching functionality is the FullProf suite [93].

The FullProf suite is capable of implementing all the procedures outlined in this section, from determining potential unit cell parameters and space groups to Rietveld refinement on potential structures.

2.6.3 Alternative Methods

One final alternative to generating candidate structures through analysis of collected data is to produce candidate structures through computation, like density functional theory (DFT) calculations as implemented in *ab initio* random structure searching (AIRSS) [54], or a Monte-Carlo trial-and-error approach which tries several trial structures for a defined unit cell as implemented in the FOX software [94, 95].

AIRSS depends on density functional theory to generate candidate structures. The initial "random" structures are generated with respect to certain sensible constraints, taking into account the atomic sizes of unit cell contents for example [54]. The forces acting on the atoms in this random structure can then be calculated by DFT along with the total energy of the structure. These structures are then allowed to relax and thereby reduce the total energy and minimizing the internal forces of the structure. This process is repeated for several different random structures until the structure with the lowest total energy has been found several times from different initial structures [54].

The FOX software relies on comparison of randomly generated structures to x-ray or neutron powder pattern data to determine the suitability of a structure. The structures are generated randomly, however, some parameters are able to be fixed. The FOX program also allows for either individual atoms to be entered into the trial unit cells, or for groups of atoms to be fixed relative to one another within rigid bodies, such as a tetrahedron, and these rigid bodies are then allowed to vary within the unit cell. The randomly generated structures can then be used to calculate a cost function, which depends on one or more powder data sets and/or prior knowledge about the system, such as bond lengths [94]. After several trials are performed in this fashion, convergence on the best possible configuration is achieved through implementation of either a parallel tempering or simulated annealing algorithm. Both algorithms are similar and reduce the temperature the process is performed at, thus favouring better structures [94]. Parallel tempering differs from simulated annealing by performing a small number of optimisations simultaneously at different temperatures, and

allowing the structural configurations within these different optimisations to swap between each other, to avoid becoming trapped within local minima [94]. Once the predetermined number of iterations, or trials, of the selected algorithm have been completed, the structural configuration should produce a viable candidate structure for further refinement.

2.6.4 Comparison of the Available Methods

While each of the procedures described above can lead to solving a crystal structure, there are several other considerations that need to be made. For example, direct methods require a good single-crystal sample. However if it is impossible to grow such a single-crystal, then this method cannot be used. Also if a single-crystal dataset has any strong reflections that saturate the detector, and therefore have incorrectly determined the intensity for these strongest reflections, then this dataset cannot be used to determine a crystal structure.

For the Powder procedure, if a powder sample has several different unknown phases contained within it, determining reflection intensities via the LeBail method, and hence determining the unit cell and space group becomes extremely difficult. Powder samples do require the less preparation than single-crystal samples, which may also be a consideration if single-crystal preparation is very time consuming for the substance being analysed.

The method of determining potential crystal structures through AIRSS or Monte-Carlo methods requires some structural information to limit the parameter space being explored, otherwise calculations can easily become computationally expensive and impractical. However, this method has the benefit of requiring the least information to construct trial structures but still requires actual data for these structures to be further refined against.

Each method has advantages and disadvantages, and a combined approach of these methods has been implemented in the analysis presented in chapters 5, 6 and 7.

2.7 Concluding Remarks

The fundamental diffraction theory required to interpret the data that will be shown in this thesis has been explained, illustrating the link between the data recorded by the various instruments used to collect the data and how this can be used to produce structure solutions. Both the Bragg construction and the more abstract Laue construction have been presented and shown to be equivalent. While the Bragg construction is formed in real space is easier to picture, the Laue method, which is formed in reciprocal space, can be more useful in referring more directly to the observed data.

There are several different programs available to solve crystal structures and the main programs used for analysis of the work in this thesis have been presented here. Of these programs, the most extensively used is GSAS as most of the data collected are from powder diffraction data.

Chapter 3

X-ray and Neutron Facilities Overview

This chapter will look at the variety of possible x-ray and neutron sources available for probing condensed matter materials at high-pressure with a brief explanation into how they operate. X-ray and neutron diffraction will also be compared against one another and the relative merits of both techniques discussed. In the descriptions of synchrotron x-ray sources, reactor and spallation neutron sources, the Diamond Light Source, the ILL and ISIS will be referred to as specific examples of each of these facilities respectively.

3.1 X-ray and Neutron diffraction

The theory presented in Chapter 2 can be applied to both x-ray and neutron diffraction techniques, despite the examples all being presented in the context of x-ray diffraction. These two techniques have their own advantages and disadvantages which will be highlighted here with the instrumentation described in more detail later in the chapter.

X-rays are primarily scattered from the electron cloud of an atom, which means that the larger the atomic number Z of the atom, the stronger a scatterer of x-rays that atom is. This causes problems for studying samples which are composed of light elements, which are harder to distinguish between if they are separated by only one or two atomic numbers. Additionally, samples which contain a mixture

of high Z atoms, such as lanthanides or actinides, and low Z elements, such as hydrogen, tend to make detection of these lighter elements more difficult. In addition x-ray sources tend to be much brighter than neutron sources, and this increased flux means that x-ray experiments can be conducted in a fraction of the time of a comparable neutron experiment. This higher flux also means that samples can be smaller, which again leads to higher pressure samples being able to be probed.

Neutrons diffract from the nucleus of atoms which they are incident upon, and as a result each neutron scattering factor is unique to each atom and bears no relationship to the size of the atom it is interacting with. This provides good experimental contrast between samples that contain atoms with similarly sized electron clouds. Also, the neutrons can interact quite strongly with the nuclei that they are incident upon, as some isotopes have an overall non-zero nuclear spin. This is most obvious with the difference in interaction of the neutron beam with hydrogen and deuterium. The hydrogen nucleus is a single proton, which can have a nuclear spin of $\pm\frac{1}{2}$, and this means that the interaction between the nucleus and the incident neutron beam will depend on the spin of the incident neutrons. In deuterium atoms two particles exist in the nucleus, a neutron and a proton, and thus the total nuclear spin is an integer number, reducing the influence of the spin on the incident neutrons. This is known as anomalous scattering, as it alters the trajectory of the neutron beam from what would be expected from a totally elastic interaction.

From this elementary comparison of neutron and x-ray scattering techniques it is quite easy to see that the two techniques are complementary. Considering the types of samples that will be examined in this work it also becomes clear that using both x-rays and neutrons will be necessary. Ammonia hydrates contain oxygen and nitrogen, which give a higher structure factor contrast in neutron experiments. However, probing high pressure samples (beyond the present limit of neutron experiments which is approximately 25 GPa [96]) and probing samples which contain isotopes that increase the anomalous scattering of the sample are best performed by x-ray experiments.

3.2 X-ray Diffraction

3.2.1 Lab Sources

Laboratory based x-ray sources generate x-ray beams by firing an energetic beam of electrons into a metal"target". The cathode of the laboratory source is attached to a filament that emits electrons that are then accelerated under vaccuum to energies typically 30 keV or greater into the anode. When the electrons strike the anode a continuous spectrum of x-rays are produced [97]. This x-ray spectrum however is not used for diffraction, as another process occurs within the metal target which produces a more intense source of x-rays. Above certain energies, the electron beam incident on the target can strip out electrons from the inner shell of the target atoms, the subsequent de-excitation of outer shell electrons to fill this gap releases an x-ray photon of a set wavelength [97]. Since the wavelength of the x-ray photon emitted is entirely dependent on the material the target is made out of, this is known as the characteristic spectrum [97]. Two typical lab source targets are copper and molybdenum, which have the largest photon fluxes at 1.5418 and 0.7107 Å respectively [97]. Unwanted x-ray wavelengths can be removed from the spectrum either through a filter that absorbs the unwanted radiation, or by passing the radiation through a monochromator which allows through only one x-ray wavelength [98]. Monochromators will be looked at in more detail in the next section.

The major drawback for lab-based sources for this work is that the flux of x-ray photons that are incident on the sample is much lower than the flux of a synchrotron source, increasing the data collection time for the samples significantly. Also the diameter of the x-ray beam produced is large when compared to the sample size. This means that in addition to illuminating the sample, the gasket material and possibly even the backing plate material, and large portion of the diamond anvils are also illuminated creating many parasitic reflections. These extra reflections are large diamond Bragg peaks and powder rings from the backing plate and gasket material.

3.2.2 Synchrotron Sources

Synchrotrons all operate on the same physical principle: a charged particle being accelerated by a magnetic field will emit electromagnetic radiation [99]. All synchrotron facilities contain the same three basic parts which are shown in Figure 3.1. Firstly electron bunches are produced by an electron gun, which are then accelerated with a linear accelerator (linac) to energies which are then further accelerated by a booster synchrotron ring before finally being injected into the larger storage ring where the beam is held at operational energies typically between 2-6 GeV.

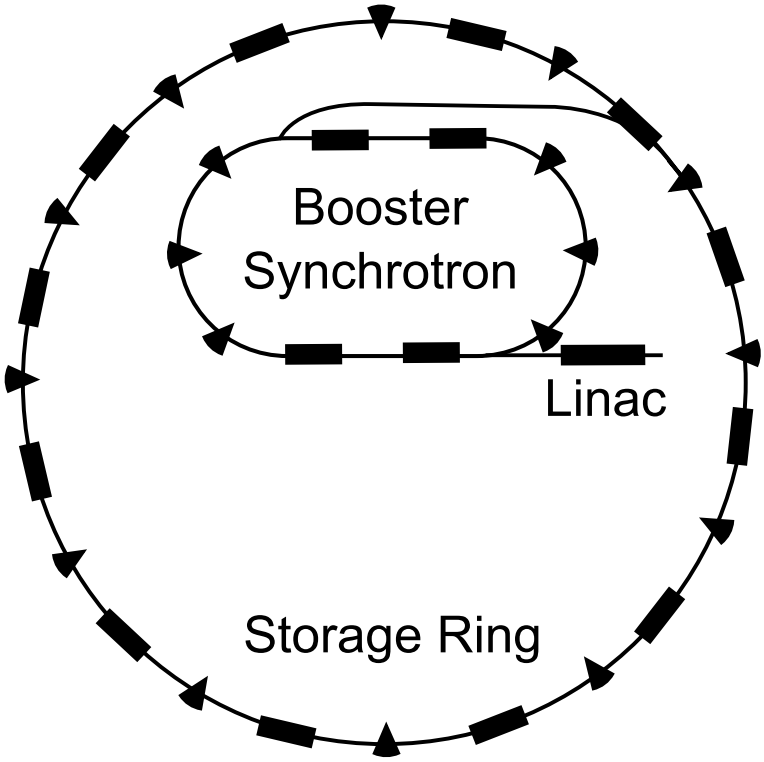

Figure 3.1 *A diagram of a synchrotron. The black wedges represent bending magnets, the black rectangles represent straight sections. The solid lines represent the beam path. Real synchrotrons will have many more bending magnets and straight sections than depicted here.*

At synchrotrons, using the Diamond synchrotron as an illustrative example, the electron beams are all held in vacuum cavities to minimise energy losses caused by collisions with air particles. The electron gun consists of a tungsten cathode in a vacuum which is then heated in order to excite electrons off of its surface, which are then accelerated towards the anode up to energies of 90 keV and gathered into "bunches" [100, 101]. Once these bunches leave the electron gun they are passed

into the linac. The linac consists of a number of Radio Frequency (RF) cavities where oscillating electric fields impart energy to the electron bunches as they pass through further increasing the total energy of the electrons [101, 102]. In the Diamond synchrotron the final energy of the electrons at the end of the linac is 100 MeV. The bunches of electrons are then accelerated within the booster synchrotron up to the operational energies of the storage ring. At Diamond the booster synchrotron consists of 36 bending magnets, in two semi circular arrangements joined by two straight sections which contain more RF cavities to accelerate the electron bunches up to 3 GeV where they are then injected into the storage ring [103]. The bending magnets are high magnetic field dipole magnet devices [102] which are used to alter the trajectory of the electrons that pass through them. In Diamond's booster synchrotron the bending magnets magnetic fields are increased as the electron beam gains energy in order to keep the beam circulating at the same radius of curvature in the semi-circular sections [103]. The storage ring at Diamond consists of another 48 bending magnets, positioned to give a the ring a circumference of 561.6 m in total [104]. These bending magnets are arranged in pairs with 24 straight sections between each pair. In these straight sections there are more RF cavities to compensate for the energy loss from traversing the bending magnets, quadrupole and higher pole magnets to reduce dispersion of the electron beam after exiting the bending magnets, and other devices in the straight sections known as insertion devices. It is also important to note that all synchrotron radiation is horizontally plane-polarised, and as such the polarisation effect has to be corrected for in data collected at a synchrotron source, or can be used to explore the magnetic order of samples [99].

The high energy of the electron beam ensures that the electrons are all travelling close to the speed of light and this biases the direction of the synchrotron radiation in a narrow forward cone [105] and as the electron beam passes through the bending magnets synchrotron radiation is produced. However this is not the only way that x-rays are produced in a synchrotron facility. Synchrotron radiation produced by the bending magnets depends on the energy of the electron beam and the strength of the magnetic fields produced by the bending magnets [99]. The x-ray wavelengths and energies of the beams produced in this manner form a continuous spectrum of soft x-rays (energies of $\sim$0.2 to $\sim$10 keV). These beams are entirely dependent on the design of the storage ring itself (its operating energy and the strength of the magnetic fields in the bending magnets) however, insertion devices offer a way of producing x-ray beams with tunable properties.

As described earlier, insertion devices are found in the straight sections of the storage ring. There are two types of insertion device, but the way they work are similar. Both rely on a series of alternating magnetic fields to alter the path of the electrons in a sinusoidal fashion as the electron beam passes through [106, 107] and this sinusoidal motion produces the x-ray radiation. They are also both designed so that once the electron beam has passed through the insertion device it remains on the same trajectory as when it entered. The wiggler insertion device is effectively a wavelength shifter [106] producing a source of hard x-rays (x-ray photons with energies of 10-100 keV). The wavelength spectrum produced is still continuous, like the bending magnet source, but the x-ray wavelengths are tunable by increasing the magnetic field and widening the gap between the wiggler magnets that the electron beam passes through. A larger number of alternating magnetic fields present in the wiggler increases the flux of the x-ray beam produced by the device [106]. The other type of insertion device is an undulator. An undulator is similar to a wiggler, in that it perturbs the trajectory of the electron beam in the straight sections of the storage ring, however the production of x-ray radiation from these devices is quite different [107]. There are many more small magnetic field magnets present in an undulator than in a wiggler and as a result the deflections from the electron beam trajectory is much smaller. The maximum angle of deflection of the electron beam by the undulator magnets is similar in size to the angle at which the x-ray photons are emitted and this leads to constructive interference, and thus an increase in intensity, at specific x-ray wavelengths which are tunable by the strength of the magnetic fields present in the undulator [99, 107].

While polychromatic (or "white") x-ray beams can be used in x-ray experiments, see chapter 2 section 2.2, it is much more common to use monochromatic x-ray beams in a synchrotron for angle dispersive crystallography. For unwanted x-ray wavelengths to be eliminated before illuminating the sample, a monochromator is used. The monochromator is typically made from a very high quality crystal with few crystallographic defects and has been cut in such a way that a crystallographic plane is parallel to the surface of the crystal. The monochromator is oriented with respect to the incoming x-ray beam so that only one x-ray wavelength satisfies the Bragg condition and is then transmitted through to the experimental hutch. This angle of the monochromator is generally variable, allowing one to select a variety of wavelengths from the beam generated by the synchrotron source [98]. The change of diffraction condition would cause the beam direction to change when a different wavelength was chosen. To prevent this, often a double crystal

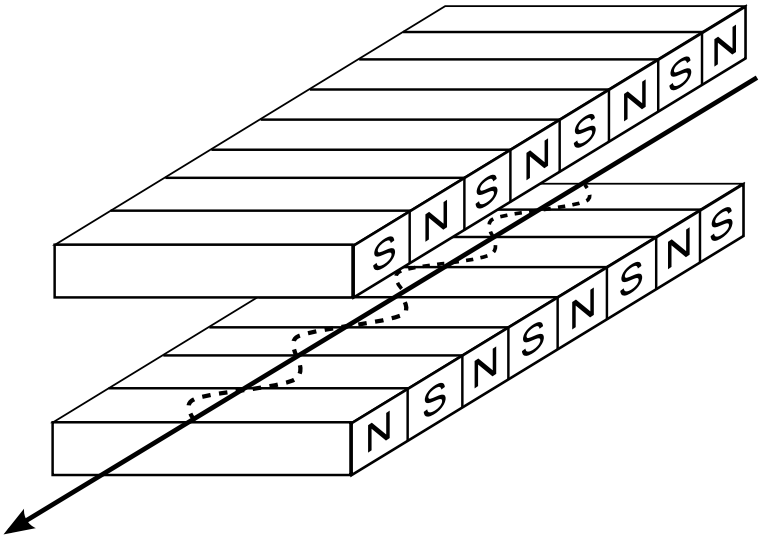

Figure 3.2 *A diagram of an insertion device. An array of opposing magnets cause the electron beam (solid arrow) to deviate from its trajectory in a sinusoidal fashion (dashed line) creating synchrotron radiation. If the photons emitted by this deviation constructively interferes with other photons emitted by the same electron by other magnetic pairs the device is an undulator, otherwise it is a wiggler.*

monochromator is used, this set up uses a second crystal to correct the change in direction.

The Diamond synchrotron has beamlines that use synchrotron radiation from bending magnets, wigglers and undulators [108], however the beamline where the majority of the x-ray results were gathered was I15 which uses a multi-pole wiggler insertion device and has a silicon dual crystal monochromator cut in the (111) direction allowing for an x-ray energy rage of 20-80 keV [109].

3.3 Neutron Diffraction

3.3.1 Spallation Sources

A spallation neutron source, as the name suggests, relies on bombarding a target nucleus with high energy particles in order to release neutrons. All spallation sources work under the same principles. Here the ISIS neutron source at Rutherford Appleton Laboratory in Oxfordshire, England will be used as an illustrative example. A particle beam is required initially, a proton beam is

preferable to an electron beam as the proton has a similar mass to the neutron, which is used to bombard a heavy metal "target" spalling off neutrons, hence the name spallation source [74, 110]. The proton beam is generated first by a linac before entering a synchrotron device, much like the first two stages of a x-ray synchrotron source discussed earlier. Again variable strength bending magnets along with beam focusing magnets and RF cavities are used to produce a beam of bunched protons at constant radius, and a further magnet, called the extractor or "kicker" magnet, is used to remove these proton bunches once they reach their maximum energy of 800 MeV, and these extracted bunches are fired at the heavy metal target [74, 110].

At ISIS this proton beam is achieved by first taking several bunches of H^- ions, hydrogen atoms with two electrons, which are injected into a synchrotron via a linear accelerator. The ions are stripped of their electrons at the end of the linac to produce a proton beam within the synchrotron, which then accelerates the protons to higher energies and gathers them into two bunches. Once at sufficient energy, these bunches are then directed to the target, each bunch producing a burst of neutrons with a characteristic time profile. This process is repeated with a frequency of 50 Hz with a mean proton current of 200 μA [111].

Spallation occurs when the target is bombarded with these protons which cause neutrons to be removed from the atomic cores of the target material, which is tungsten at ISIS [111]. A large amount of heat is produced by this process and the target requires cooling to prevent a build up of heat, ISIS uses a water cooling system to alleviate this problem [110, 111]. At this stage the neutrons produced are still too energetic and have to be cooled down by a moderator. A moderator contains a high neutron cross section material (such as water) in which the neutrons that enter are scattered inelastically until they reach energies which are useful for the experiments in question [112]. ISIS has four separate moderators to provide neutrons of various energies to the different end stations, there are two water moderators, a liquid methane moderator and a liquid hydrogen moderator [111].

At the ISIS facility, two instruments were used in the investigation of the ammonia hydrates, PEARL and SXD. The PEARL instrument is optimised for neutron-powder diffraction with the Paris-Edinburgh (P-E) press. The instrument itself uses neutrons from the liquid methane moderator, held at 110 K, which which are incident on the instrument centre where both the P-E press is seated and other necessary experimental equipment can fit, such as a tank for containing

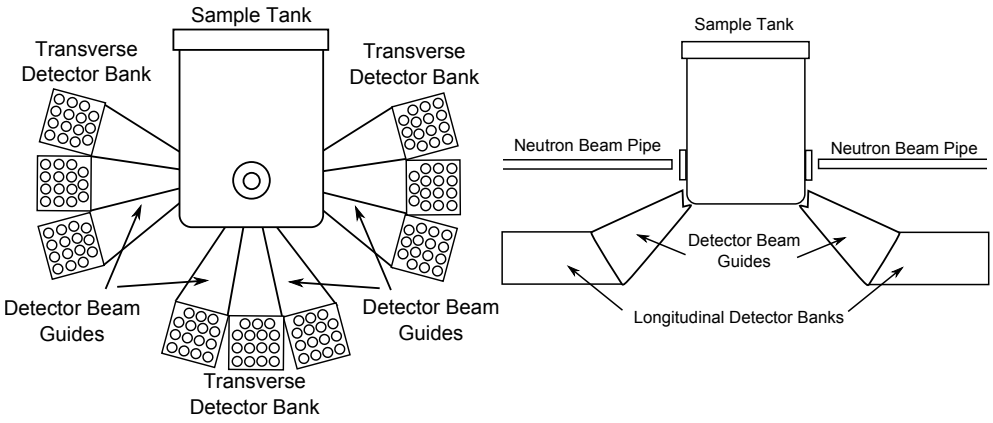

(a) *Transverse detector arrangement*

(b) *Longitudinal detector arrangement*

Figure 3.3 *A diagrammatic representation of the sample area and detectors of the PEARL instrument. The sample tank holds the P-E press and can be filled with liquid nitrogen for cooling experiments. The circular aperture seen in the left hand diagram correspond to the rectangular protrusions on the right hand diagram and are small windows that allow easier passage of neutrons through the sample tank.*

liquid nitrogen for cooling experiments, heating rings for warming samples and the associated control equipment. The main detector banks sit perpendicular to the beam direction around the centre of the instrument (see Figure 3.3). With the neutron beam entering from the back of the anvils in the P-E press, these detector banks can collect all the neutrons scattered within 8.8° of the transverse direction of the neutron beam. This primary operational mode of the PEARL instrument is hence called the "transverse" mode [113]. The other operational mode of the PEARL instrument is the longitudinal mode, in this mode the neutron beam enters through the side of the gasket to a detector which sits in the lower half of the instrument and allows longer d-spacing ranges to be observed.

The SXD instrument has a set of 11 detectors, 6 arranged around the equatorial region of the incident beam, 4 detectors at a 45° angle under these detectors and finally one detector on the base of the instrument parallel to the floor, this is schematically shown in Figure 3.4. These detectors are arranged in this roughly hemispherical fashion to allow detection of neutron diffraction peaks over the greatest amount of reciprocal space. The SXD instrument uses a water moderator which gives neutron wavelengths from 0.2-10 Å allowing access to reciprocal space from 0.4 to ∼30Å [114], although the flux at very large d-spacing is low as a result of the low number of longer wavelength neutrons (greater that 2 Å) compared to

shorter wavelengths.

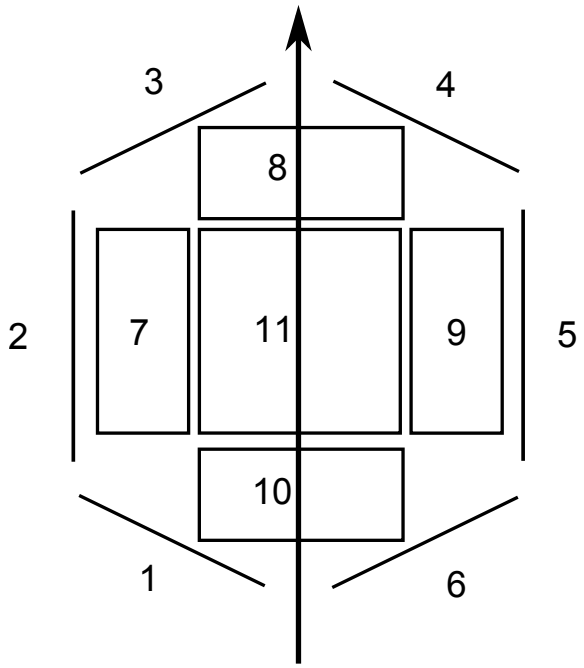

Figure 3.4 *A top down diagram of the SXD instrument showing the lay out of all 11 detectors. The arrow represents the neutron beam direction as it passes through the instrument. All the detectors are have the same area, but with different orientations.*

3.3.2 Reactor Sources

Reactor sources depend on nuclear fission to create a steady stream of neutrons for use in diffraction and other techniques. In a fission reaction, fissile material (such as uranium-235) breaks apart emitting neutrons and daughter particles. Some neutrons from this reaction contribute to continuing the fission process, while some are able to be used for the purposes of diffraction [115]. In uranium-235 fed reactors approximately 2.7 neutrons are produced from the initial disintegration of the uranium nucleus, only one of these neutrons has to go on to continue the chain reaction in the reactor, leaving 1.7 neutrons for experiments [116]. The ILL uses uranium-235 as a fuel source, and thus this type of reactor will be what is described in this section. The reactor core in the ILL contains an uranium-235 fuel element with a silver-indium-cadmium alloy control rod located within a cylindrical cavity at the centre of the fuel element. Within the core, coolant heavy water (D_2O) is circulated to remove most of the heat produced by the fission reaction and also acts as a primary moderator for the system, reducing

the energy of the neutrons produced and reflecting some of the neutrons back into the fuel element. A secondary water pool surrounds the core to provide biological shielding [117, 118]. In addition to the D_2O moderator, there is also a hot graphite moderator held at 2400 K to provide hot neutrons (short wavelengths), and two liquid deuterium moderators held at 25 K to provide cold neutrons (long wavelengths) [118]. The terms hot, cold and thermal neutrons refer to where the peak energies of the neutron flux occurs, thermal neutrons correspond to energies of approximately 36.4 meV (kT at room temperature) and has a peak neutron flux corresponding to a De Broglie wavelength of $\sim$1.5 Å. Hot neutrons has a peak flux of neutrons at approximately 0.5 Å and cold neutrons have a peak at approximately 10 Å [115].

The instruments in the ILL are situated in three locations, in the reactor hall, and in two separate guide halls. The neutrons emitted from the reactor are guided to the instruments by neutron guides fitted tangentially from the reactor to limit the background contribution from high flux gamma rays [117]. These neutron guides penetrate the reactor shielding to the point of highest neutron flux, which is then guided to the instruments. As with the ISIS facility, the ILL has a variety of instruments suited to different experimental techniques. For example the D9 instrument located within the reactor hall is used for single-crystal neutron studies. The polychromatic neutron beam from the hot neutron moderator (graphite at 2400 K) is incident upon a copper (200) monochromator which selects the operational wavelength for the experiment. The neutron wavelengths accessible by this instrument are within the range of 0.3-0.9 Å which allows for fine tuning of experiments depending on the samples being used, trading off between accessible reciprocal space and the resolution of the Bragg peaks recorded by the detector [119, 120]. The detector itself is a small 64 x 64 mm detector area with pixels of 2 x 2 mm in size. The detector is rotated to the position of the Bragg reflection intended to be recorded. This requires that some information is already known about the sample, the minimum being the unit cell of the crystal in question [119]. Once the orientation of the crystal is known, data can be collected by rotating the detector to the reflection positions, or rotating the sample to bring more reflections into the range of the detector. This instrument is capable of having a high-pressure panoramic diamond anvil cell mounted. While this reduces the observable diffraction geometries available because of the cell body itself, it does allow the use of D9 for identifying hydrogen (deuterium) locations for the analysis of hydrogen bonds and structural disorder.

There also exist several powder diffraction instruments at the ILL, for example D20. The D20 instrument is also located in the reactor hall, and receives neutrons from the D_2O thermal moderator. Several monochromators are available for use, two fixed orientation copper (200), a fixed orientation pyrolytic graphite (002) and a variable orientation germanium (113) monochromator [118], which all supply a single wavelength neutron beam. The highest flux on the instrument is achieved by using the copper monochromator providing a wavelength of 1.3 Å. D20 has a position sensitive detector which consists of 48 detection plates, which in turn contain 32 detection cells. Each of the cells has an independent output, and the entire detector covers 156.8° to a height of 15 cm which provides a very thin slice of reciprocal space to be mapped [118]. This instrument allows very small samples to be investigated, which is ideal for high pressure applications. However the design of the high pressure cell may cause some of the detector area to be shaded by the cell and thus rendered unusable.

3.4 Conclusions

With the exception of laboratory based x-ray sources, all the instruments highlighted in this chapter represent high flux sources that can produce data in minutes (x-ray synchrotron sources) to hours (reactor and spallation neutron sources). The operation of these sources and how they produce the beams used for production have been reviewed. Examples of typical instruments that could or have been used in the experiments conducted in this work have been given as illustrative examples of the various different experimental set ups at the central facilities that house them. While the exact implementation of the different instruments differ, none of the instruments presented are particularly ill-suited to high-pressure diffraction experiments. However, with the long experimental times and the limited access to reciprocal space, only the laboratory sources will not be used for this work.

Chapter 4

Generating High Pressure and Sample Preparation

There are several methods of producing high-pressure samples for study. This chapter will look at the main devices used to create the high-pressure samples for experiments on the x-ray and neutron instruments described in Chapter 3. In addition to this the methods used to prepare these devices will be explained as well as the method of creating the bulk ammonia hydrate samples. These methods will be used for the majority of the samples described in chapters 5, 6 and 7.

4.1 Diamond Anvil Cells

The Diamond Anvil Cell (DAC) has been the primary investigative tool in high pressure science since its development in 1959 [121]. With this device it is possible to reach pressures in excess of 300 GPa [122], and with the aid of laser heating and cryogenic cooling apparatus a range of temperatures from mili-Kelvin to several thousands of Kelvin can be measured [123, 124] but the device itself is surprisingly simplistic. The simplest DACs feature two opposed single-crystal diamond anvils which rest on a backing disc and taper to a much smaller surface (the culet) which range from typically 600 μm for low pressure applications to as little as 50 μm to attain the highest pressures. In between the anvils a thin sheet of metal acts as a gasket, preventing the diamond anvils from touching. A small

hole in the gasket material, much smaller than the diamond anvils culets, forms the sample chamber. This set up is illustrated in Figure 4.1 and relies only on the principle $P = \frac{F}{A}$ to achieve mult-giga-pascal pressures. Typically the force is applied to a DAC by tightening screws on the cell body to force the culets closer together, but this leads to a certain lack of control over the pressures achieved by tightening these screws by hand.

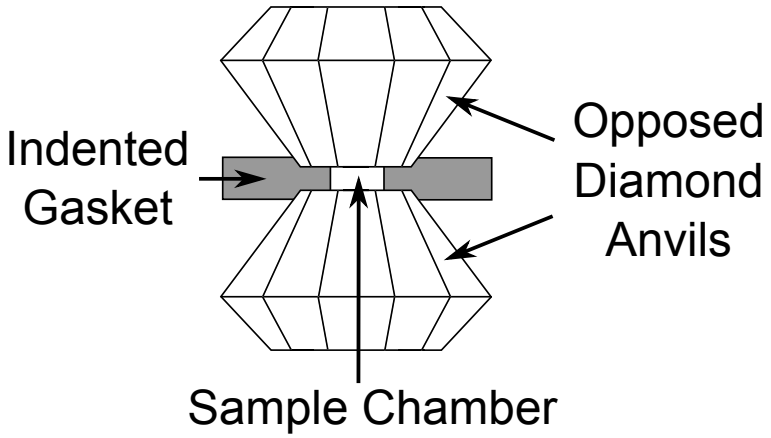

Figure 4.1 *A cross-section schematic of a simple diamond anvil cell set up*

There are several individual DAC designs, each with their own unique advantages and disadvantages. Merrill-Basset cells are perhaps the most widely used cell because of their simplicity [125]. Figure 4.2 shows the design of the M-B cell, its body consists of two mostly triangular halves with three screws that are used to push the two halves of the cell together, which in turn applies force to the backing discs that then apply the force to the pair of diamonds being used. Three guide pins ensure the cell retains alignment upon repeated assembly/disassembly, and alignment of the diamonds can be adjusted on each half of the cell by the use of three grub screws that are kept in contact with the backing discs that hold the diamond in place. The M-B cell has many advantages, its compact design means it is highly portable and can be mounted into a variety of different experimental set ups, for example laser set-ups and x-ray beamlines, even when sample space is minimal. The downside to M-B cells is the fact that during the process of increasing pressure, force will be applied unevenly, this is unavoidable as only one screw can be tightened at a time, for lower pressures this isn't as important, but at the force limits of the diamonds being used, this can become an issue. Also because of the three grub screw alignment system for the backing discs, aligning the diamonds is perhaps trickier to achieve than using four screws for the same purpose.

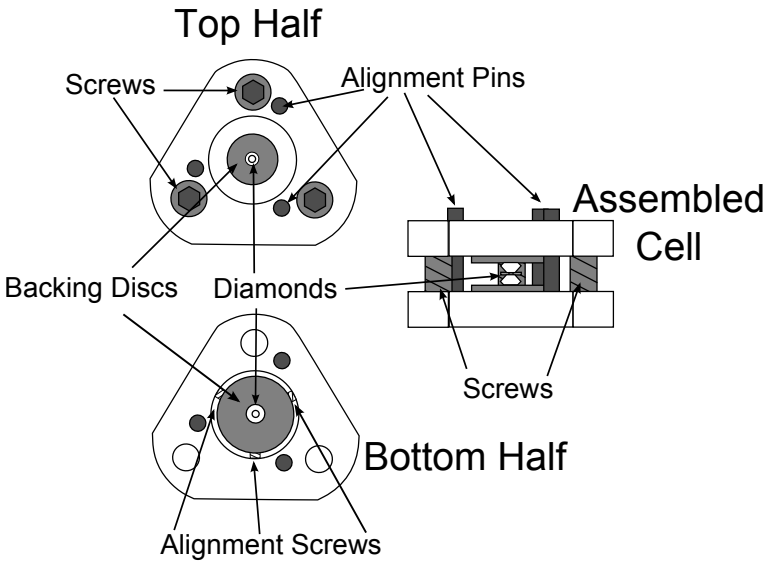

Figure 4.2 *A labelled diagram of a Merril-Basset diamond anvil cell showing both halves of the cell in a top down view as well as the fully assembled cell in a side on view. The top half is shown from the "outside" of the cell as it would appear when closed. The bottom half is shown from the "inside" where the sample and gasket would be placed before assembling the two halves of the cell.*

The design of the M-B cell allows for backing discs to be interchanged quite easily once the cell is disassembled. There are two main types of backing discs which are used for mounting diamonds in the M-B cells, these are beryllium backing discs and Boehler-Almax tungsten carbide backing discs. These two types of backing discs are shown side by side in Figure 4.3. The beryllium discs are very simple in design, and the diamonds are glued over the central aperture, and as a result they can be quite hard to align properly, but they can be used with a number of differently sized diamonds providing that they cover the aperture. The Boehler-Almax design has the diamond mounted in a conical recess over an aperture which tapers away from the central hole, and requires specially cut diamonds to sit within the recess. The design allows for greater angular access to the sample chamber without the x-ray beam passing through the backing disc while still providing adequate support for the diamonds. This is very advantageous for single-crystal experiments where a large angular access is desirable. However, this design requires a specific size of diamond with a specially cut diamond required to fit into the recessed area. This does make the alignment of the diamonds with respect to the backing disc much simpler, as it can only fit into the recess provided for the diamond.

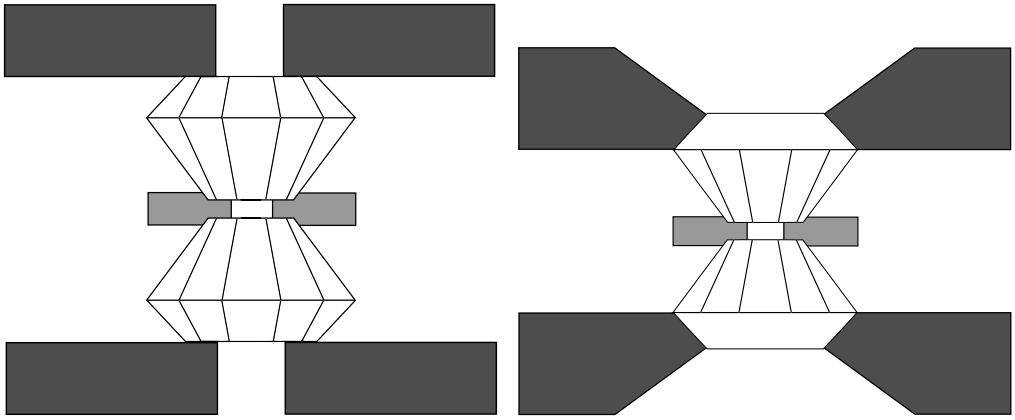

(a) *A Beryllium backing disc*

(b) *A Boehler-Almax tungsten carbide backing disc*

Figure 4.3 *Two different types of backing discs that can be used in the Merrill-Bassett DAC.*

Another type of cell is the Diacell x-ray (DXR) cell. This type of cell is shown with a simple schematic in Figure 4.4. DXR cells uses an outer backing plate to apply force to a central piston, and this force is supplied by two screws of opposite threading. This set up allows force to be supplied to the diamonds in a uniform manner, reducing the chance of failure through uneven force distribution and as a result extends the range of pressures accessible by a given pair of diamonds. One clear disadvantage of the DXR type cells are their size, they are much larger than a M-B cell, and also because of their design they have very limited angular access for x-ray beams. This makes them unsuitable for single-crystal experiments compared to M-B cells. Also the large main cell body introduces complications in the loading process as a result of the small diameter but deeply recessed cavity for housing the piston.

Considering the advantages and disadvantages of the cells presented here, the work conducted has primarily used the Merrill-Basset cell for the bulk of x-ray experiments, with DXR cells used for very high pressure experiments.

4.2 Paris-Edinburgh Presses

While the DAC is perfect for use in high flux x-ray experiments, in neutron experiments, as discussed in chapter 3 section 3.1, the low flux requires a large volume to observe a significant signal compared to the background. To do this a greater force needs to be applied to the sample in question, and this larger force

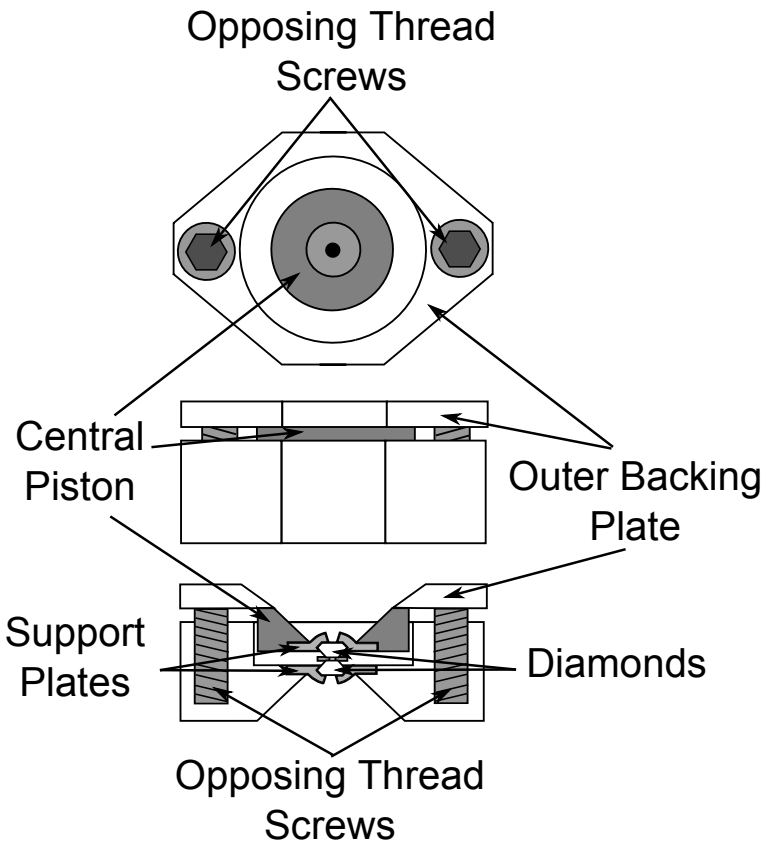

Figure 4.4 *A labelled diagram of a DXR type diamond anvil cell. The top two figures show how a DXR cell looks fully assembled from a top down and a side on view. The bottom-most figure shows a cross sectional view of the DXR cell.*

needs to be applied uniformly in the confined space of a neutron beamline. These issues are overcome by the Paris-Edinburgh press (P-E press).

The P-E press uses a number of hardened anvil materials (usually either sintered tungsten carbide or sintered diamond) and a hydraulic ram to apply the force required to pressurize samples. At the opposite end of the ram is the breach, which holds the opposite anvil in place during the experiment and can be unscrewed and removed to allow access to load samples. In the end of this breach there is a space for a collimator material, typically boron nitride, which absorbs neutrons diverging from the beam direction, to reduce background levels. The anvils themselves have a very specific geometry to endure the various stresses applied under pressure. The tips of the anvils have toroidal grooves around the "cups" that form the sample volume and the anvils taper from the toroidal groove to the edges of the anvil assembly at a very shallow angle of 7° [126]. The purposes of this geometry is specifically to minimize the stresses that are experienced during

the experiment being conducted which allows pressures of ∼10 GPa to be reached. The anvils are then housed within binding rings of hardened steel which continue to taper out to the piston housing which contains the anvil assembly, see Figure 4.5.

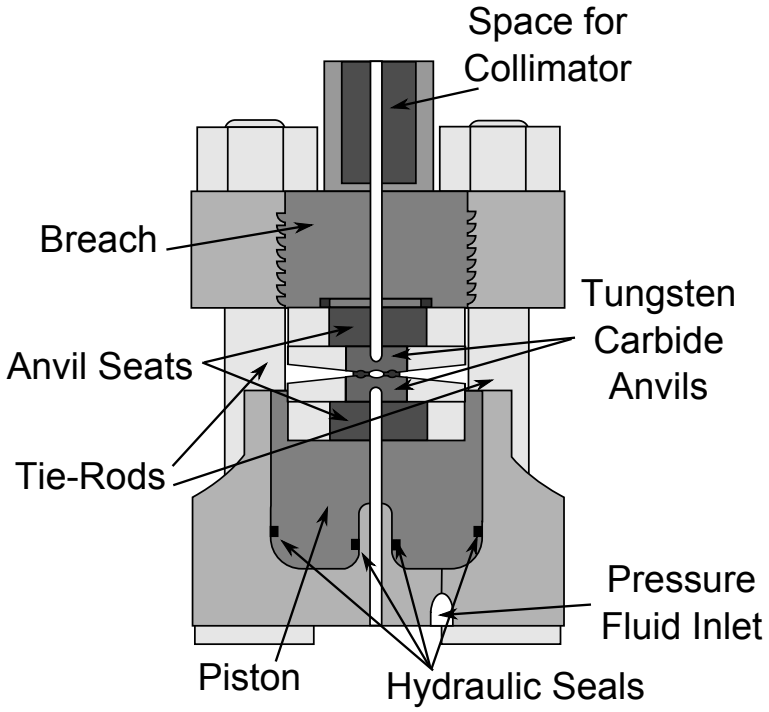

Figure 4.5 *A labelled cross-section diagram of a Paris-Edinburgh press after [127]. The whole device is held together by four large hardened steel tie-rods. The anvils can be fixed to the breach and the piston for loading purposes. The pressure fluid inlet allows for different hydraulic fluids to be used to pressurise samples (see text).*

Each anvil is supported by an anvil seat, which also have hardened steel binding rings, that serves to distribute the force supplied by the piston (and breach) in a more even fashion. An O-ring is used to provide a hydraulic seal between the piston and the cylinder. The hydraulic fluid used to provide the force on the piston depends on the temperature the cell will be used at. Standard oil based hydraulic fluid is usable for ambient temperature applications, a 5:1 mixture of iso-n-pentane and n-methyl butane, is usable down to temperatures of 110 K if the supply capillary is insulated and heated against the liquid nitrogen bath that the cell sits in. For temperatures lower than this helium is required to be used as the hydraulic fluid but this requires different seals in the P-E press to prevent helium leakage at very high pressures.

Gaskets for the P-E press come in two varieties, encapsulating or non-encapsulating

gaskets, both typically made of TiZr null-scattering alloy. TiZr, is a titanium zirconium alloy. The titanium has a negative coherent scattering factor and zirconium has a larger positive one. By alloying the two metals in a molar ratio of 2.08:1 Ti:Zr an effective zero coherent scattering can be achieved, meaning that this material is effectively neutron transparent, or null-scattering [128]. Both of the different gasket types require an outer ring to occupy the toroidal part of the anvil surfaces to provide an inward force to support the inner gasket and prevent it from extruding significantly and thus providing better pressure efficiency. The inner part of the gasket forms the sample chamber and are classified as either encapsulating or non-encapsulating. Non-encapsulating gaskets are a simple small washer that sits within the larger outer washer and forms the sample chamber with the cups within the centre of the anvils. Encapsulating gaskets on the other hand are formed of two halves which come together to form a smaller sample volume, but this sample volume has no contact with the anvil surfaces. Both types have their own unique benefits, and their use primarily depends on the types of samples that are desired to be loaded. Non-encapsulating gaskets provide a larger sample volume, which reduces collection times, but the contact with the anvils can lead to either diffusion problems, such as with gases like hydrogen or helium, or reactivity problems, which would lead to an anvil failure. Encapsulating gaskets, prevent contact between the anvils and the sample, making them particularly useful for loading gases and reactive materials.

Single toroidal anvils like the ones described earlier allow the study of samples up to a maximum of $\sim$10 GPa with sintered diamond anvils [126]. To study materials at higher pressures than this slightly different geometries of the anvils are required, as samples require more toroidal supports to withstand the forces involved, but in practice this is usually limited to only one additional toroidal ring in double toroid anvils. The principles involved are much the same as with the single toroidal anvils. Gaskets have an additional set of supports and the inner toroid support and the gasket itself are thinner than the outer supports to reduce the deformational forces experienced by the inner parts upon initial compression. This ultimately extends the pressure range up to $\sim$30 GPa using sintered diamond anvils. The single and double toroidal anvil cross-sections are shown side by side in Figure 4.6.

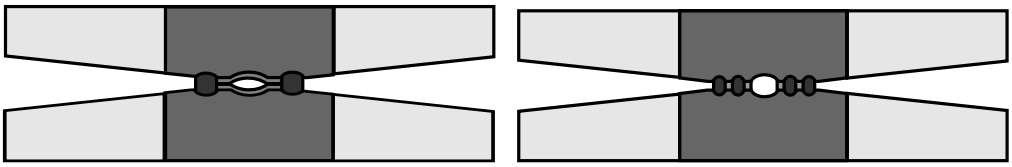

(a) *A single toroid tungsten carbide anvil with hardened steel binding disk and encapsulating gasket*

(b) *A double toroid tungsten carbide anvil with hardened steel binding disk and non-encapsulating gasket*

Figure 4.6 *A cross section of single and double toroidal tungsten carbide anvils (dark grey) and the hardened steel binding rings (light grey) used to support them. Sintered diamond anvils have an extra tungsten carbide binding ring between the anvil and the hardened steel ring for added support. The dark grey sections between the anvils show the toroidal supports for the gasket, the light grey sections show the flat washer gasket and/or encapsulating gasket.*

4.3 Experimental Procedures

4.3.1 Sample Preparation

As discussed in chapter 1 section 1.8, mixed ammonia and water solutions with an ammonia content higher than ∼33% ammonia by molar weight are unstable at ambient conditions. As a result in order to prepare higher concentration of ammonia-to-water the sample must be held at a lower temperature. The method that was used to prepare all samples of AMH, AHH and even ADH was the same method used by Loveday *et al.* over the course of all their studies of the ammonia hydrates [42, 43, 51]. To prepare a sample, one pre-weighed and dried stainless steel vessel with a valve attached was connected to a gas cylinder that contained ammonia via steel tubing. Once the two containers were connected together, the empty vessel was immersed in liquid nitrogen and allowed to come to thermal equilibrium. Once this was achieved the valves were opened and ammonia was condensed into the smaller vessel. The valves were then shut and the vessel warmed back up to room temperature, and care was taken to ensure no moisture was left on the vessel. This set up is shown in Figure 4.7. Weighing the vessel again gave the mass of ammonia contained within, which could then be used to calculate the molar weight of the ammonia. After this a volume of water corresponding to the molar ratio of the ammonia hydrate desired was decanted into a second pre-weighed and dried vessel with another valve attached.

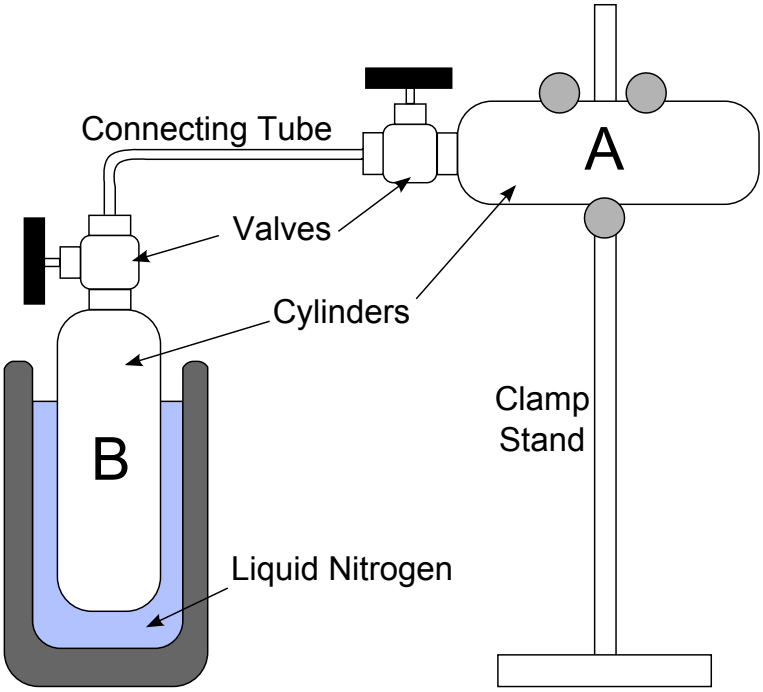

Figure 4.7 *A diagram representing the experimental set up used to form the bulk ammonia hydrate samples as described in the text. When both valves are open, gaseous ammonia condenses from cylinder A into cylinder B, which is held at liquid nitrogen temperatures.*

This second vessel was then connected to the first in the same way as shown in Figure 4.7, and immersed in liquid nitrogen. Once the second vessel was in thermal equilibrium with the liquid nitrogen both valves were opened and the ammonia condensed from the first vessel into the second. The apparatus was left until the first vessel returned to room temperature to ensure that the ammonia had been successfully transferred into the second vessel. The valves were then sealed and the second vessel allowed to return to room temperature where the mixture was shaken to ensure proper mixing and also weighed again to determine the exact composition to the desired composition. All hydrogenous ammonia hydrate samples were made with ammonia gas (99.99% purity) obtained from Sigma-Aldrich and distilled water (99.9 % purity). Samples for study via neutron diffraction were created using deuterated water (99.98 % deuterated) and deuterated ammonia (99 % deuterated), again from Sigma-Aldrich. Deuterated samples were used for neutron experiments as hydrogenous samples have a large incoherent scattering background as explained in chapter 3 section 3.1.

The method described above was used to prepare all the ammonia hydrate samples studied in this thesis, including those of ammonia dihydrate (ADH

1:2 ammonia-to-water ratio) unless otherwise stated. The reason for this was to ensure that the compositions were known as exactly as possible. ADH composition is stable at room temperature, however fluctuations in temperature may alter the exact composition of ammonia solution over time, and the composition can also be known much more accurately via the method outlined above.

4.3.2 Pressure Determination

There exist several methods to calculate the pressure of samples inside of both DACs and P-E presses. One of the most wide spread methods for samples prepared in DACs is the ruby fluorescence method [129]. This method relies on a small piece of ruby being placed in the same sample chamber as the sample of interest in a DAC or other device that allows optical access. Illuminating the ruby with laser light excites the electrons within the ruby, causing a characteristic fluorescent emission of light with a wavelength of ∼694.3 nm in ambient conditions, this is known as the R_1-line of ruby. When the load on the diamonds is increased, and hence the pressure of the sample and ruby is also increased, the wavelength of R_1-line can be clearly observed to increase. This pressure dependance on the fluorescence of the ruby R_1-line is well documented [129] and also depends on the temperature of the sample. The ruby fluorescence method is a widely used for pressure determination but depends on samples being accessible by laser light. For DACs this is not a problem for most samples, as diamonds are transparent to visible light, however for devices such as P-E presses, where samples are not normally optically accessible, this technique cannot be used.

For samples that cannot be viewed optically an alternative pressure calibration method needs to be used. One such method requires including another material that has a well characterised equation of state (EOS). An EOS relates pressure, volume and temperature to one another, or can relate only two of these three variables and shows how they vary with respect to each other [130]. For the purpose of being used as a pressure calibrant the most useful EOS's are those that relate volume to pressure. One of the most commonly used EOS is the third-order Birch-Murnaghan Equation of state, which takes account of the compressibility (bulk modulus) of the material in question and the rate of change of this compressibility as pressures are increased on the material [131]. This EOS

is reproduced in equation 4.1.

$$P = \frac{3K_0}{2}\left[\left(\frac{V_0}{V}\right)^{7/3} - \left(\frac{V_0}{V}\right)^{5/3}\right]\left\{1 + \frac{3}{4}\left(K_0' - 4\right)\left[\left(\frac{V_0}{V}\right)^{2/3} - 1\right]\right\} \quad (4.1)$$

Here P is the pressure of the sample, V is the volume of the sample, K_0 is the bulk modulus at 0 pressure, K_0' is the derivative of the bulk modulus with respect to pressure at zero pressure and V_0 is the volume at zero pressure. Providing the values of K_0, K_0' and V_0 are known, the pressure of a sample can be determined from the lattice parameters of the material in question. Additionally, if given a set of precisely measured pressures and temperatures the three EOS fitting parameters, K_0, K_0' and V_0 can be determined through fitting the EOS to the observed data.

Providing the calibrant remains stable over the pressure range being investigated, the sample pressure can be determined. This is done by using the collected diffraction pattern to fit the lattice parameters of the calibrant and comparing the unit cell volume against the EOS. However, relying on the diffraction pattern means that the choice of pressure calibrant has to be made very carefully. The ideal calibrant must have very little overlap with the diffraction pattern of the sample, so that a structure determination can still be made with little error, and ideally this would mean that the pressure calibrant would have few diffraction peaks of its own, and thus have a high symmetry structure. One such suitable calibrant is lead [132] which has a cubic structure and remains stable over a large range of pressure and temperature. However, the exact suitability of a pressure calibrant depends entirely on the diffraction pattern of the sample being studied, as overlap with diffraction peaks from the sample has to be avoided. Another consideration is whether the material used as a pressure calibrant can react with the sample. Obviously a reactive calibrant is unsuitable for use. Lead does have a cubic to hexagonal phase transition at approximately 14 GPa, making it useful for low pressure P-E press experiments [132].

It is also possible to estimate the pressure of the sample from the load supplied to the sintered diamond anvils. This requires the supplied load to be measurable, and as such cannot be done for the smaller DACs used for x-ray experiments which apply load from the tightening of screws. Paris-Edinburgh presses have load sensors which accurately display the load supplied by the hydraulic fluid

in terms of tonnes of force supplied to the piston generating the force on the diamonds, this load can then be equated to the sample pressure [126]. While this method of pressure determination has the advantage of not adding any additional material to the sample chamber, or requiring the camber to be viewed optically, this method is the least accurate in pressure determination compared to the other methods outlined above as many factors can alter the relationship between the load supplied to the piston and the pressure generated by the anvils. These include the sample volume enclosed in the gasket, the compressibility of the sample, and whether the sample has been compressed before. However, this method can serve as an initial pressure indicator for a material whose reactive properties and diffraction pattern are unknown.

4.3.3 Gasket Preparation

Before a sample can be loaded into a DAC a gasket needs to be prepared to prevent contact between the two opposing diamonds and to contain the sample and prevent it escaping from between the diamonds. A gasket is simply a strip of metal that sits between the two diamonds, the type of metal used is generally dependant on whether it will react with the gasket material, and the mechanical properties of the material itself. Some typical metals used as gasket material are steel, tungsten and rhenium. The gasket material is first pre-indented between the diamonds of the DAC. The purpose of this is to mechanically harden the gasket material and create a very thin gasket between the diamond anvil culets. This prevents extrusion of the gasket material from between the diamond anvils during the experiment, leading to a more stable sample chamber [133]. The ideal thickness of a gasket is only slightly thicker than what would be achieved by the end of the experiment [133].

Once the pre-indentation of the gasket has been done the sample hole can then be made. In samples prepared in DACs for neutron experiments it is still possible to create gasket holes with conventional drill bits, however for high-pressure DACs used in x-ray experiments the typical hole sizes required ($\sim$200 – 50 μm) needs a different technique. A small hole can be created in the gasket through spark erosion, a process also known as electrical discharge machining. In this process two electrodes are brought into close proximity within a dielectric fluid causing a spark between the closest points of the electrodes vaporising some of the material [134]. Here the gasket forms one of the electrodes, and the other is made of

tungsten wire with a diameter of the desired sample hole size. The gasket is then placed in acetone in an ultrasonic bath to clean it of any remaining residue from the spark eroding process. The gasket is then replaced on one of the diamond surfaces and the cell is ready for loading.

4.3.4 Sample Loading

The process of loading samples into both P-E presses and DACs are very similar. For DACs, of the Merrill-Bassett type as described in section 4.1, each half of the DAC was placed on a metal surface which was in thermal contact with a liquid nitrogen bath with a pre-indented gasket attached to one of the diamonds. This nitrogen bath both served to cool the sample down to nearly 77 K and provide a dry nitrogen-rich atmosphere which prevented water from condensing into the sample chamber. In preparation for loading, the bulk sample contained in the sealed vessel was placed in a container with either isopropyl alcohol (IPA) cooled by dry ice or liquid nitrogen, the liquid nitrogen cooling method cools the IPA to its freezing point where a constant temperature can be maintained. IPA has a melting point of 184 K and dry ice sublimes at 194.7 K, which are temperatures at which any form of ammonia hydrate can exist as a liquid. The liquid IPA provides good thermal contact to the container vessel of the bulk sample.

When all of the vessel has reached thermal equilibrium with the cooling mixture, the liquid sample can be dripped onto the gasket hole where it immediately freezes in place, the two halves of the DAC can then be rejoined and closed to seal the sample within it. The process for loading the P-E press is similar, except that only the anvils are cooled within the liquid nitrogen bath. A clamp apparatus is used to hold the two opposing anvils in place while the anvils are transferred into the P-E press, held at a low temperature to keep the sample from separating and ammonia being lost during the loading process. A small load is then applied to the press to ensure a seal is kept tight on the sample before the experiment begins.

4.4 Concluding Remarks

The experimental procedures outlined in this chapter are used for the preparation of all the samples described in chapters 5, 6 and 7 unless otherwise specified.

There are a number of pressure determination methods, which have also been described and the advantages and disadvantages of each approach has been examined. The various types of pressure cell that have been used in this work have also been described in detail, and shown to be ideally suited to the experiments being conducted in this thesis.

Chapter 5

AMH V: Pressure-induced Dehydration and the Structure of AHH-II

In this chapter the structure of the phase identified as ammonia monohydrate V (AMH-V) will be discussed. As described in chapter 1 section 1.8, the structure of AMH-V has remained unsolved since it was first discovered by Loveday *et al.* [42]. As AMH-V shares a boundary with the liquid phase, growing a single crystal of this phase appeared to be the best method of attempting to solve the crystal structure. However, data collected on both an x-ray single-crystal and neutron powder samples were required and will be presented in turn. The results of the analysis of the data collected will be discussed and finally the structure solution will be presented and compared to other known structures.

5.1 Experimental

The first sample studied was a single-crystal hydrogenous loading of ammonia monohydrate (AMH). This sample was in a Merrill-Bassett DAC and was prepared and loaded using the method explained in chapter 4 section 4.3.1. A stainless steel gasket was used, the gasket indent was 80 μm thick with 125 μm diameter gasket hole. The diamond culet size was 400 μm. The sample was taken to a pressure of 3.6(4) GPa measured by the ruby fluorescence method,

and a single crystal grown from the melt. The crystal did not completely fill the sample volume, which could mean that the crystal was grown very close to the solid/liquid phase boundary of the system. The crystal was transparent to visible light and also allowed light to pass through when the DAC was placed between two crossed polarisers. Optically isotropic materials, such as liquids and unstrained cubic crystals, will not allow light to pass through crossed polarisers as they do not change the polarisation of the light, and as such the liquid portion of the sample did not allow light to pass through crossed polarisers; only the single-crystal did.

In addition to this first sample, a second sample was prepared with ammonia solution (33% volume ammonia) in a DAC with 300 μm culets and a stainless steel gasket indented to 43 μm and the gasket hole had a diameter of 125μm. This sample was taken to the pressure of 3.8(4) GPa. As a result of this sample being of $\sim$ 1:2 ammonia-to-water ratio, there will be a portion of the sample that is purely ice VII, as described by Fortes *et al.* [59], and to attempt to limit the diffraction from ice in the sample the excess ice was grown as a single crystal in addition to the AMH single-crystals grown, which could then be excluded from the region probed by the synchrotron x-ray beam. In this sample along with the large ice VII crystal, two smaller crystals of AMH were also grown, and again only the AMH crystals allow light to pass through crossed polarisers. Pictures of both the 1:1 and 1:2 composition single-crystal samples are shown in Figure 5.1.

Single-crystal x-ray data were collected at the ID09a beam line at the ESRF in Grenoble, France. The detector used was a Mar555 detector. The beamline was calibrated with a silicon standard sample which determined the wavelength to be 0.4142(2) Å. The data were collected with an exposure time of 1s per step angle of 0.25° over a $\pm$ 30° range either side of the cell's axis. Unfortunately even this minimal exposure time still saturated the detector for some of the Bragg reflections so it was not possible to completely solve the structure from this data set alone. However, it was possible to determine the unit cell and possible space groups of the crystal. The space group determination was achieved through analysing the x-ray data firstly with the Bruker SMART software [81], to pick out the reflection positions on the detector for each orientation of the DAC. Once this was done, the array of data points could then be viewed in RLATT, a reciprocal lattice viewer which is a part of the Bruker software [81], to remove any erroneous point that had been picked out, these are points that do not line up in a regular reciprocal lattice. The corrected data set could now be analysed in SMART

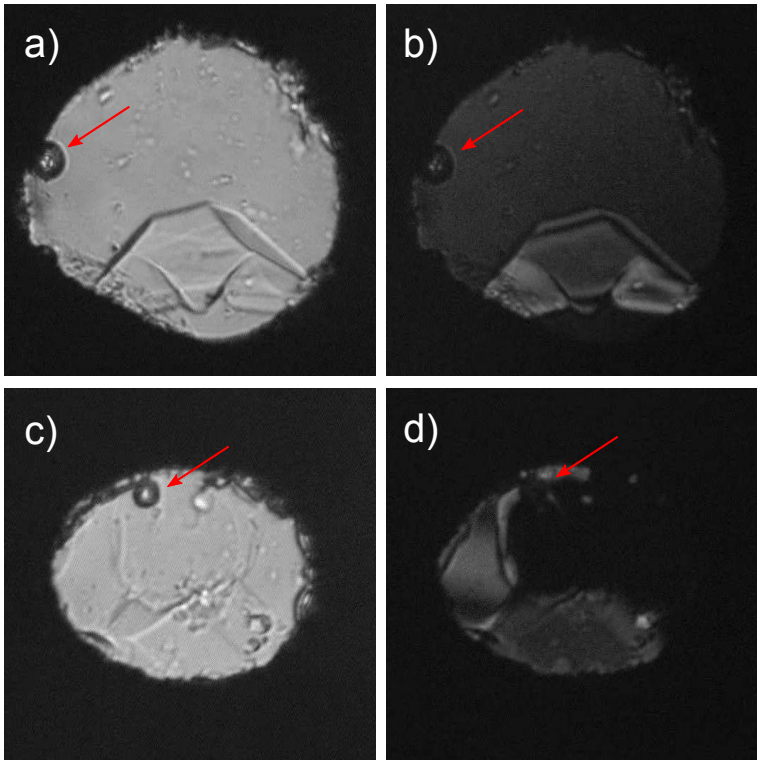

Figure 5.1 *These figures show single-crystals grown in the samples referred to in the text. a) shows the 1:1 sample, c) the 1:2 sample. b) and d) show the same samples viewed through crossed polarisers. Crystals that allow light through the crossed polarisers are the crystals of interest. The red arrows show the location of the ruby sphere pressure calibrant.*

to determine the lattice parameters. For the 1:1 ammonia-to-water sample the lattice parameters were found to be $a = 3.396(1)$ Å, $b = 9.254(1)$ Å, $c = 9.006(2)$ Å, $\alpha = 90.05(1)°$, $\beta = 94.40(1)°$ and $\gamma = 90.06(1)°$ at room temperature and a pressure of 3.6(4) GPa, and this unit cell was suggested to be a monoclinic space group. The data was then processed through the Saint integration program [83], which extracted the total intensities of each reflection into a data file. This was then entered into the XPREP program [84] which examined the unit cell symmetry, systematic absences and equivalences of reflections and was found to be consistent with the space group number 14 ($P2_1/c$), although at this stage it could not be ruled out that the full structure (with hydrogen atoms) had the symmetry of one of two subgroups $P2_1$ and Pc. Data were also collected on the 1:2 sample with the same exposure and angle range as the 1:1 sample, with a step size of 0.5°. Again the sample was over-exposed, but the lattice parameters determined for this single crystal was $a = 3.355(2)$ Å, $b = 9.209(7)$ Å, $c = 8.924(6)$ Å, $\alpha = 90.14(3)°$, $\beta = 94.34(3)°$ and $\gamma = 89.93(4)°$ at room temperature with

a pressure of 4.0(4) GPa. The lattice parameters for this AMH crystal in a 1:2 composition sample has nearly identical lattice parameters which are all slightly smaller in magnitude than the 1:1 sample, which is to be expected from the slight difference in pressure between the two samples and does indeed show that the same structure is observed in both these cases. A further single-crystal 1:1 sample was prepared in a much larger panoramic DAC intended for study by neutron single crystal methods, however there were complications with the data collected from this sample which will be described in detail in chapter 6.

Unit Cell Parameter	*1:1 Sample Values*	*1:2 Sample Values*
a	3.396(1) Å	3.355(2) Å
b	9.254(1) Å	9.209(7) Å
c	9.006(2) Å	8.924(6) Å
α	90.05(1)°	90.14(3)°
β	94.40(1)°	94.34(3)°
γ	90.06(1)°	89.93(4)°

Table 5.1 *The unit cell parameters determined from x-ray single-crystal data from samples of 1:1 and 1:2 ammonia-to-water ratio presented side-by-side for ease of comparison. the data for both samples were collected at room temperature, and a pressure of 3.6(4) GPa for the 1:1 sample, and a pressure of 4.0(4) GPa for the 1:2 sample.*

This unit cell could then be compared to the original neutron-powder data collected by Loveday *et al.* [42, 43] for the AMH Vb structure. Figure 5.2 shows LeBail fits to the neutron data based on the unit cell determined from the x-ray diffraction data. The upper plot shows good agreement with the data, but with a couple of reflections unexplained by the unit cell, most notably, the peak at 2.35 Å (shown in more detail in the inserts). The position of this peak corresponds well with that expected for the strongest (110) reflection of ice VII (the stable phase of ice at pressures above 2 GPa at room temperature) [135]. Including Ice VII as a phase in the profile of the powder pattern produced the LeBail fit on the lower plot of Figure 5.2, and it can easily be seen that the fit now explained all the peaks observed in the pattern, including a longitudinal pattern shown in the insert where two further peaks at higher d-spacing can be identified.

The presence of ice in the sample was not expected, but could mean that the sample loaded did not have the intended 1:1 ammonia-to-water ratio. However the sample had been taken down to low temperatures at ambient pressure, and showed a powder diffraction pattern perfectly described by the AMH-I structure, this pattern is shown in Figure 5.3. Since ice VII is present in the high-pressure

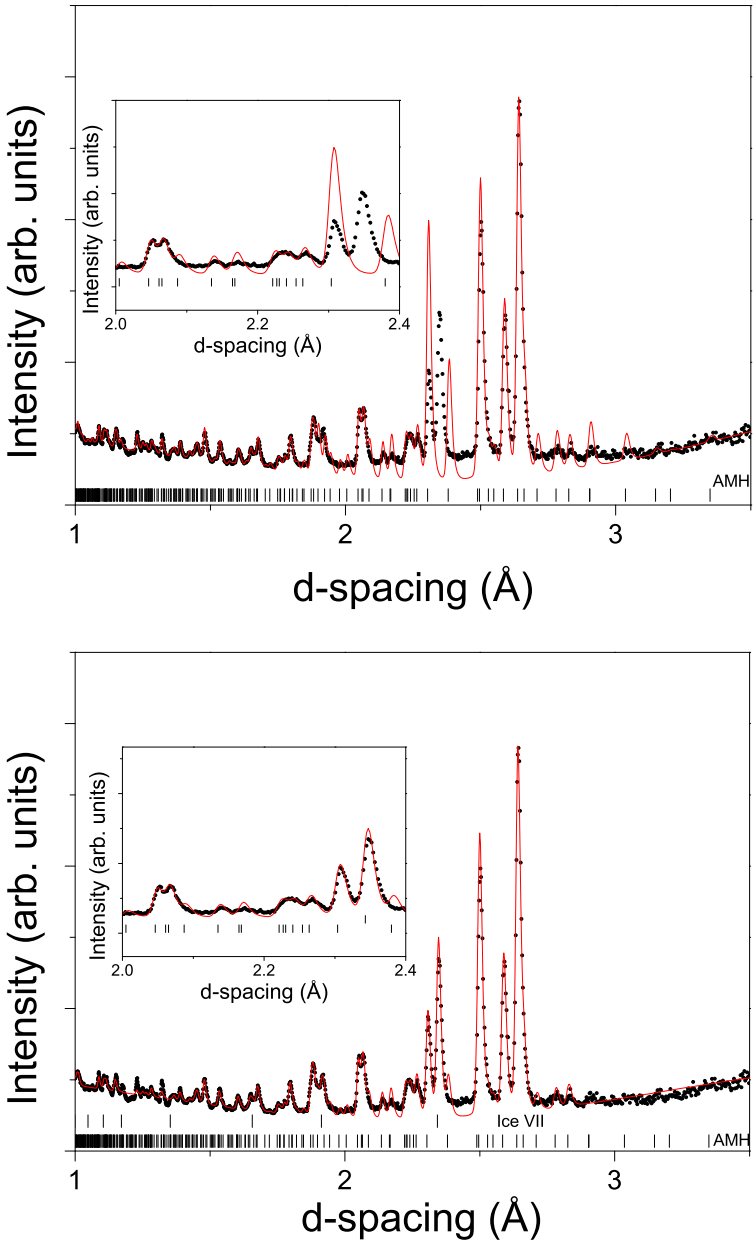

Figure 5.2 *Le Bail fits of the neutron-diffraction data, the dots show the observed data points, the red lines show the calculated fit to the data. The upper plot is fitted using only the monoclinic unit cell of the ammonia hydrate determined from x-ray single-crystal data and the lower plot is additionally fitted with the unit cell of ice VII. The vertical lines denote the expected positions of reflections which are labelled to show which phase they represent. The inserts shows a close up of the d-spacings around the ice (110) reflection.*

powder diffraction pattern, this means that phase must be richer in ammonia than was previously thought.

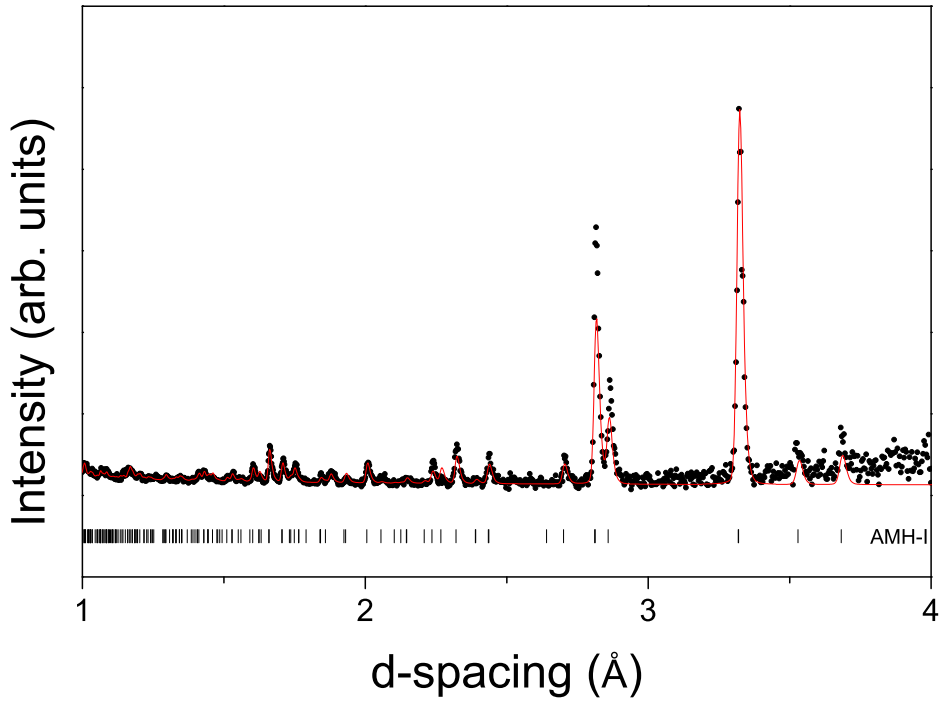

Figure 5.3 *Rietveld fit of the same neutron powder sample at ambient pressure and low temperature, corresponding exactly to the structure of AMH-I as described by ref [43]. The black points are the collected data and the red line is the calculated pattern from the crystal structure of AMH-I.*

Comparing the unit cell volume found in the x-ray study to the AMH-I equation of state (EOS) provided by Loveday *et al.* [43] it was possible to estimate the number of formula units of AMH, and therefore the total number of molecules within the unit cell. From the Murnaghan equation of state given by Loveday *et al.* [136] the volume of a unit cell of AMH-I at 3.5 GPa is approximately 195 Å^3, corresponding to four formula units of AMH, which is equivalent to approximately 48.75 Å^3 per AMH formula unit. This means for the monoclinic unit cell, which has a volume of 282.2 Å^3, there will be a total of ∼5.8 formula units of AMH within the unit cell, this means there will be a total of ∼12 molecules in the unit cell. While the LeBail fits suggest that the structure is richer in ammonia than previously thought, using the AMH-I EOS would not be a good choice to base the deduction of the contents of the unit cell. However, the average volume per molecule (taken over both water and ammonia) for ADH, AMH and AHH at ambient pressure are respectively 30.170(6), 30.604(2) and 30.583(2) Å^3 [43]. These values are very similar and show no obvious trend between volume per molecule and composition, so the use of the AMH-I EOS for this different composition should still be able to determine the unit cell contents.

The apparent dehydration of AMH is somewhat surprising given that Boone and Nicol [49] concluded that at this pressure and temperature they observed AMH and sometimes ice, depending on the composition of the sample. However, it should be noted that they only studied a single 1:1 composition sample and that the sample was powdered which may have hampered identification of the ice in their samples. From their extensive exploration of the ADH/AMH stability regions in solutions with a 1:2 ammonia water ratio, it would have been difficult to estimate the amount of ice produced when the sample decomposed into ice and an ammonia hydrate and hence the amount of water contained in that ammonia hydrate.

5.2 Rietveld Refinement of the Structure

As discussed, it was not possible to fully analyse the single-crystal x-ray data as a result of saturation of the detector by a few of the Bragg reflections. The LeBail analysis of the unit cell to neutron-powder data did show that the structure could be indexed with this unit cell and it was also deduced that 12 molecules could fit within its volume. Rietveld analysis could be performed on the structure if the approximate locations of the atoms were known. The FOX program [94, 95] was used to obtain this starting point. The FOX program uses a Monte-Carlo algorithm to randomly place a set of predetermined objects (individual atoms or user defined molecules) within a unit cell and then making finer adjustments to their locations and orientations to produce a better fit to the data set provided. In the $P2_1/c$ space group there are two possible configurations to arrange twelve molecules in the unit cell. The molecules could either be distributed over three general (4e Wyckoff positions) or two general and two special sites (2a, 2b, 2c or 2d Wyckoff positions). As the exact composition of the sample was unknown, but was known to contain both ammonia and water, a "general" molecule was used to represent either a water or ammonia molecule. This general molecule consisted of central atom which contained both a nitrogen and oxygen atom both with 50% occupancy, and four hydrogen atoms located around the central atom which formed a tetrahedron. The hydrogen atom sites all had an occupancy of 62.5% .

After running several iterations of the parallel tempering algorithm in FOX it became very clear that the three four-fold site configuration was preferred. the same structure arrangement appeared repeatedly with a goodness-of-fit (G-o-F)

of 3685. In comparison, the two general and two special position models gave a G-o-F of 9760 when the algorithm had finished. The goodness-of-fit combines the quality of fit to the data (χ^2) and the degree to which any user imposed structural constraints are obeyed. In this case, no constraints were used and hence the (G-o-F) is proportional to χ^2. This arrangement of "general" molecules was then entered into GSAS [91, 92] for more detailed refinement, now on both the longitudinal and transverse data sets.

The general molecule was entered into GSAS as a rigid body where the distribution of the deuterium atoms around the central nitrogen/oxygen site remained the same. However, the distance between the central atom and the deuterium atoms was allowed to vary, but each bond was kept the same relative length. In addition to the unknown phase which was being solved, two other phases, ice VII and hexagonal tungsten carbide (the anvil material) were also included in the fit. The initial refinements showed that all the peaks were indeed explained by the preliminary structure, however some of the peak intensities were not correct, and the weighted R factor R_{wp} had a value of 7.41%. At this point the central atom in the general molecule was allowed to vary in ratio between oxygen and nitrogen, with an increase in one leading to a proportional decrease to the other, along with the occupancy in the deuterium atom sites remaining consistent with the N/O occupancy (three deuterium atoms per nitrogen and two per oxygen). After this refinement convergence was achieved when two of the central atoms preferring to be nitrogen rich and another to be oxygen rich. One of the nitrogen rich sites and the oxygen rich site had refined to nearly 100% occupancy of one atom rather than the other, the other nitrogen rich site gave approximately 75% occupancy of nitrogen. This was taken as an indication of preferred site order of the molecules in the system, and seemed to suggest that the structure may be much closer to ammonia hemihydrate (AHH, 2:1 ammonia-to-water ratio) in composition than ammonia monohydrate. At this point the central atoms of the general molecule were assigned to be either nitrogen or oxygen with 100% occupancy, the assignment of the central atoms were determined by the nitrogen/oxygen preference shown in the previous refinement. The deuterium sites were then renormalised to give occupancies that corresponded to the molecules present at those sites, 50% occupancy for the water molecule, 75% occupancy for the ammonia molecules, this reduced R_{wp} to 6.49%. The other two possible arrangements of two nitrogen and oxygen atoms distributed over the three general positions gave poorer fits than the original disordered model (R_{wp}=8.45 and 8.37%).

The occupancy of the deuterium atom sites was then allowed to vary. This was done one molecule at a time to lessen the chance of divergence in the refinements. For the ammonia sites, one deuterium site reduced to barely any occupancy while the other three sites all increased in occupancy to nearly 1. For the water sites one site reduced to zero occupancy while the others retained some deuterium occupancy. When this step was repeated again, a further deuterium site on the water molecule reduced to zero while the other two increased and very little difference was observed from the ammonia sites. This showed a preference in orientation order for this compound, and also suggests that this structure is an ammonia hemihydrate phase, not a monohydrate phase. As both ammonia and water molecules are known to not have perfectly tetrahedral angles between their constituent hydrogen atoms, at this stage the rigid bodies of the "general" molecules were replaced on the molecular sites with molecules of either ammonia or water as determined by the process described earlier. On the remaining atoms, soft constraints were initially given to limit the angles between deuterium atoms bonded to nitrogen to be 107.8° and deuterium atoms bonded to oxygen to be 106.5° and initially constrained to be within ±0.1° of these angles, similarly all intra-molecular bond lengths were constrained to be 1±0.1 Å in length. After initial refinement these constraints were gradually lifted until final convergence was achieved with no constraints on the system at all. The plot of the final result of this Rietveld refinement is shown in Figure 5.4 and shows very good agreement with the observed data. Numerically the final refinement gave a weighted profile R factor (R_{wp}) of 4.25% with a total of 61 fitting parameters. The refined parameters were the fractional co-ordinates of all the atoms (33 parameters total), 14 background co-efficients for the two histograms, 2 thermal parameters, lattice parameters of all phases in profile (7 total, 4 for AHH-II, 2 for tungsten-carbide (anvil material), 1 for Ice VII), scale factors of both longitudinal and transverse data sets and two phase fractions (for ice and tunsten carbide), two diffractometer constants for the longitudinal data and one for the transverse data.

The structure determined from the plot in Figure 5.4 is shown in Figure 5.5, and atomic positions and bond lengths are detailed in Tables 5.2 and 5.3 respectively. The final lattice parameters for the structure after refinement of the neutron data were $a = 3.3584(5)$ Å, $b = 9.215(1)$ Å, $c = 8.933(1)$ Å and $\beta = 94.331(8)°$. The pressure of the neutron sample can be calculated by comparing the unit cell volume of the excess ice in the sample volume against the EOS of deuterated ice VII [135] and was found to be 3.5(1) GPa at room temperature.

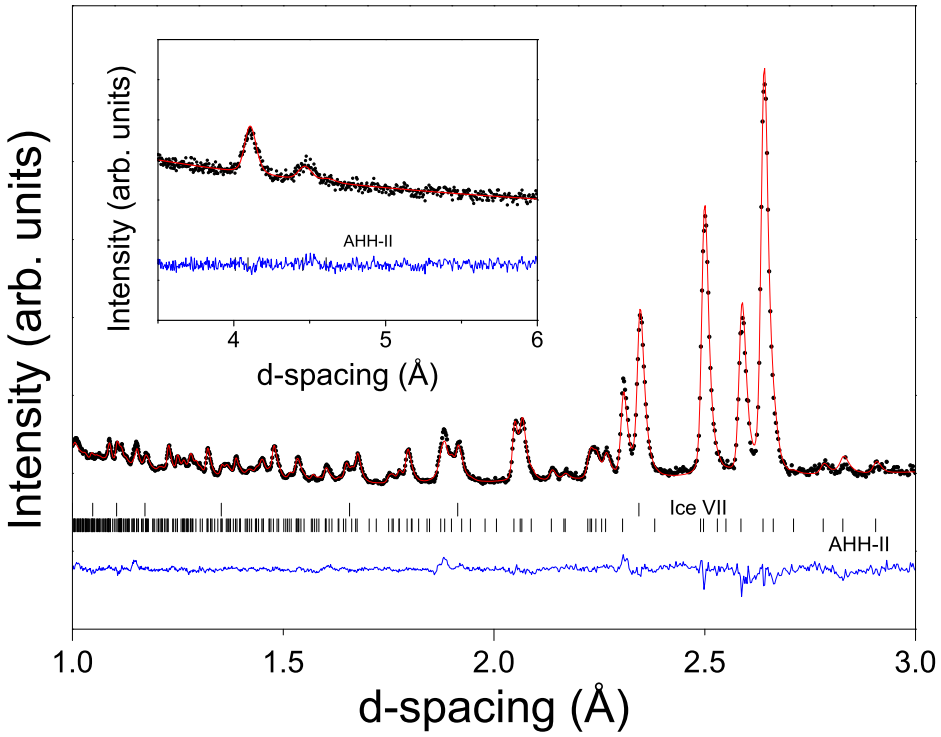

Figure 5.4 *Reitveld refinement fit of the AHH structure with ice included to neutron-powder data. The dots show the observed data points, the red line shows the calculated fits, the lower blue line the difference between observed and calculated plots, and the vertical lines show the expected positions of reflections as per Fig 5.2. The insert shows the high d-spacing data obtained in the longitudinal orientation (see text).*

Figure 5.5 shows the structure as viewed down the *a*-axis. This can be described in full by a series of chair configuration hexagonal rings each "crowned" by an ammonia molecule that has one bond that points near parallel to the *a* axis. Hexagon A is marked out by the ring of molecules N1a, O1b, N2c, O1c, N1c, O1a and crowned by the molecule N2b. If only the molecular centres of these molecules were to be considered, then this unit would tile the entire *b*-*c* plane of the structure with very minor positional differences. However, the orientation of the hydrogen bonds complicate this somewhat and require another three crowned hexagons to be defined to reproduce the structure in full. These are marked in Figure 5.5 as Hexagon A′ (formed by N2a, O1a, N1c, O1d, N2c, O1b and crowned by N1b), A″ (formed by N1c, O1c, N1a, O1a, N2a, O1d and crowned by N2b) and A‴ (formed by N2c, O1d, N2a, O1b, N1a, O1c and crowned by N1d). These are all hexagons crowned by ammonia molecules that have a bond nearly parallel to the *a* axis. Alternately a set of four hexagons that are crowned by ammonia

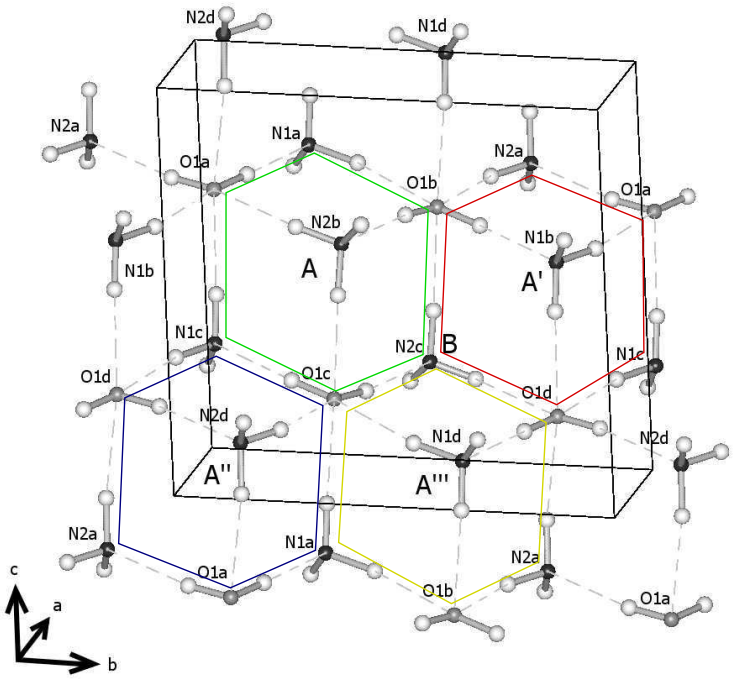

Figure 5.5 *The structure of AHH-II viewed approximately along the a axis. The black balls represent nitrogen atoms, the grey oxygen atoms, and the white hydrogen atoms. The hydrogen bonds are shown as dashed lines. The unit cell is drawn as solid black lines around the structure. The hexagons A, A′, A″ and A‴ have been highlighted in green, red, blue and yellow respectively for clarity.*

molecules with a hydrogen bond that have a bond near anti-parallel with the *a* axis can be used to describe the structure, only one of these has been highlighted in the diagram for illustrative purposes, marked B (outlined by O1b, N1b, O1d, N1d, O1c, N2b and crowned by N2c). This planar structure is reproduced at each lattice repeat along the *a* direction so that the atoms of adjacent layers lie directly on top of one another when viewed along this axis. A consequence of this arrangement is that the only bonds between the layers are N1-H...N1 and N2-H...N2 bonds formed between crown ammonia molecules with a length equal to the a lattice parameter.

5.3 Structure Analysis

While the fit to the observed data is very good and indicates that the correct solution has been reached, some other avenues had to be investigated in order

Atom	*x*	*y*	*z*	$U_{iso} \times 10^2$ *(Å^2)*
O1	0.033(4)	0.877(3)	0.238(2)	1.1(1)
D4	0.135(6)	0.791(2)	0.185(2)	1.8(1)
D5	0.157(6)	0.961(2)	0.199(2)	1.8(1)
N1	0.715(3)	0.134(1)	0.414(1)	1.1(1)
D1	0.818(4)	0.032(2)	0.365(2)	1.8(1)
D2	0.796(3)	0.134(2)	0.525(2)	1.8(1)
D3	0.408(4)	0.142(2)	0.398(1)	1.8(1)
N2	0.665(2)	0.874(1)	0.902(1)	1.1(1)
D6	0.746(3)	0.869(2)	0.018(1)	1.8(1)
D7	0.718(5)	0.777(2)	0.859(2)	1.8(1)
D8	0.361(4)	0.893(2)	0.890(1)	1.8(1)

Table 5.2 *Coordinates of AHH structure at 3.5(1) GPa obtained from neutron-powder diffraction data, all atomic sites are on 4e (x,y,z) Wyckoff positions.*

Atoms	*H-bond length(Å)*	*Atoms*	*Covalent bond length(Å)*
N1···O1	3.1560(4)	N1-D1	1.09795(13)
N1···O1	3.0797(3)	N1-D2	1.00803(15)
N1···N1	3.3585(5)	N1-D3	1.03178(16)
O1···N1	2.7819(3)	O1-D4	0.99962(11)
O1···N2	2.8411(3)	O1-D5	0.96441(10)
N2···O1	3.1696(4)	N2-D6	1.05366(15)
N2···O1	3.0387(3)	N2-D7	0.99777(13)
N2···N2	3.3585(5)	N2-D8	1.03369(16)

Table 5.3 *The X...Y and X-D distances of all hydrogen bonds (X-D...Y) in the structure of AHH-II. The bond lengths were calculated from the relative atomic positions within the unit cell, this means that the precision of the bond lengths will be overestimated.*

Atoms	*Bond Angle(°)*
D4–O1–D5	107.19(4)
D1–N1–D2	108.71(5)
D1–N1–D3	110.21(4)
D2–N1–D3	109.18(6)
D6–N2–D7	107.49(3)
D6–N2–D8	106.83(5)
D7–N2–D8	108.45(4)

Table 5.4 *The bond angles describing the molecular arrangement of the ammonia and water molecules. Again the error has been calculated from the atomic positions derived within GSAS and likely overestimate the precision.*

to make sure that this conclusion was in fact correct. Firstly, the dehydration effect, while already known as described in chapter 1, was previously thought to dehydrate ammonia dihydrate to ammonia monohydrate. While the reason for this being reportedly incorrect has been addressed in section 5.1, this would mean that the volume of ice in the sample should be predictable. In the structure described earlier, through the $P2_1/c$ symmetry, there are 8 ammonia molecules and 4 water molecules. In order to obtain the ideal loaded ratio of ammonia-to-water another 4 molecules of water are required, this equates to two unit cells of ice VII which contain two water molecules each. This would mean that the proportional difference between the different structures would be 1:2 of AHH-II:ice VII. In the GSAS program, this property is called the phase fraction, so called because each different structure that is entered into the program is referred to as a separate phase. This number represents how much of a phase (structure) contributes to the overall fit compared to the other phases present. After final refinement the ratio between the two phase fractions of AHH-II and Ice VII was 1:1.82(3), and while this is not exactly the ideal ratio of 1:2 this discrepancy could be due to some of the ice in the sample being formed outside of the section of the sample chamber being illuminated by the neutron beam and thus not contributing to the powder pattern. This adds further support to the other evidence that the structure is correct and that the phase labeled AMH Vb by Loveday and Nelmes [42, 43] is in fact a structure of ammonia hemihydrate and should be called AHH-II.

Comparing the structure to the structure of ice VII reveals an underlying packing similarity, this is shown in Figure 5.6, and shows that both these structures contain a crowned chair hexagon arrangement albeit with a very different hydrogen bonding scheme. The upper diagram in Figure 5.6 shows hexagon A crowned by N2b along with a repeat of this crowned hexagon one unit cell away along the a direction with the N2b′-N2b H-bond providing the bonding between layers. The crowning atom N2b is N-H···O H-bonded to O1a, O1c and O-H···N H-bonded to O1b with H-bond lengths in the range 2.8-3.2 Å. However, this ring is also "crowned" in the other direction by N2b′ which has short non-bond contacts to atoms N1b, N2a and N1a in the range 2.9-3.2 Å to N2b′. The lower plot shows the analogous ring structure in ice VII formed by six oxygen atoms (labelled A to F), this ring is "crowned" on both sides by two oxygen atoms $\kappa 1$ and $\kappa 2$. Although $\kappa 1$ and $\kappa 2$ are not H-bonded to the (A to F) ring they have non-bond O$\cdots$O contacts which are the same length as the H-bonds to atoms B, D and F in the case of $\kappa 1$ and atoms A, C and E in the case of $\kappa 2$ and these contacts are shown

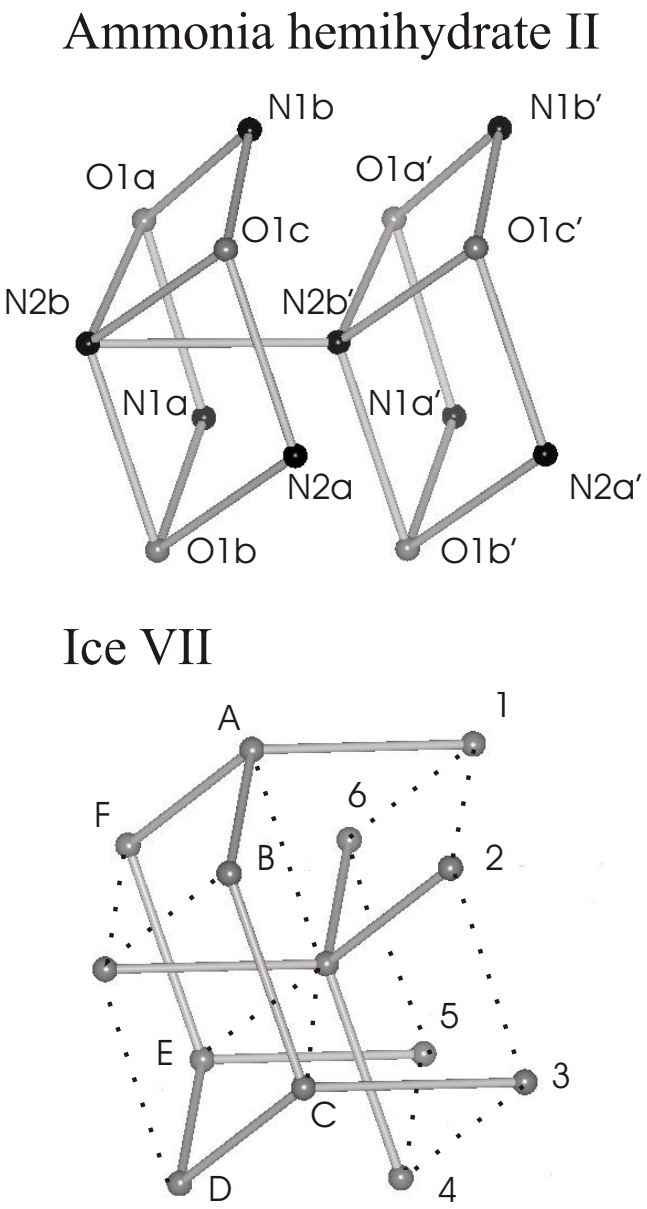

Figure 5.6 *Top: The crowned hexagon A of AHH-II as described in the text showing the stacking of adjacent hexagons along the a-axis. The solid lines show H-bonds, for clarity the hydrogen atoms have been omitted. Bottom: The analogous capped ring structure in ice VII. The solid lines represent H-bonds and the dotted lines represent non-bond O···O contacts whose length is identical to that of the H-bonds. Again for clarity the hydrogen atoms have been omitted.*

as dotted lines. In AHH, the adjacent crowned ring along the a-axis (labelled N1b′ etc.) is within the next adjacent unit cell and hence an identical copy, in ice VII it is not and instead $\kappa 2$ forms H-bonds to atoms 2, 4 and 6 of a ring formed of

entirely of these short non-bond contacts (again shown as dotted lines). Hexagon B exhibits qualitatively the same geometry as hexagon A with small differences (at the level of 0.1 Å) in the individual interatomic distances and it thus appears that although AHH-II and ice VII have very different H-bond topologies, their molecular packing is rather similar. Given that the molecular packing of ice VII remains stable up to the highest pressures studied [137] it might be expected that AHH-II (or at least its packing) is also likely to be stable over a large pressure range. The similarities in the molecular packing also suggests that the principal driving force for the formation of this structure is the need to achieve the best possible packing density at the expense of a distortion of the hydrogen bonds. This has also been observed in the high pressure phase IV of ammonia [7] and in the case of AHH-II manifests itself in the formation of N-D$\cdots$N H-bonds. These do not occur in the open ambient-pressure structures of the ammonia hydrates, yet in AHH-II they are the only source of bonding between the layers of crowned hexagons. It should also be noted that the structure of the disordered molecular alloy (DMA) phases of AMH and ADH aslo show a remarkably similar packing arrangement to ice VII.

5.4 Discussion

Both a 1:1 and 1:2 ammonia-to-water composition sample produced the same lattice parameters under analysis of single-crystal x-ray diffraction data, and by implication formed the same structure. From these single-crystal data, it appears that the dehydration boundary reported by Boone and Nicol [49] and Fortes *et al* [59]. does not just signal the upper pressure limit of the ADH composition in the solid, as they reported, but also the upper limit of the AMH composition. This has an interesting implication for the known disordered molecular alloy phases (DMAs) of ADH and AMH reported by Loveday *et al.* and Fortes *et al.* [51, 59, 61]. Now both AMH and ADH DMAs appear to be able to exist above the dehydration boundary where other structures would split into a mixture of AHH and ice, and are observed to do so. It would appear that either AHH-II or the DMA phases are metastable, however no conclusion on that matter can be drawn from the data presented here, and it should be noted that the P-T paths taken to form these phases are very different and it could be possible that the structure formed is entirely path-dependent. Crystallisation at room temperature does, however, seem to consistently form a mixture of AHH-II and ice VII so this

would appear to be the thermally stable form, at least at pressures of 3.5 GPa.

Ma *et al.* reported an ammonia hemihydrate phase that first formed at the same pressure and temperature region as the phase AHH-II presented here [2] and derived an orthorhombic unit cell for this structure (See Chapter 1 Section 1.9.3). The data presented by Ma *et al.* are from x-ray powder diffraction and only show five identifiable peaks which is much less detailed than the neutron data analysed in this chapter. The three largest peaks can also quite easily be described by the structure of AHH-II. Of the remaining two peaks one can be attributed to AHH-II, but the last remaining peak cannot, but it does, however, sit in the same relative position attributed to ice VII in the data presented here. This would mean that there could have been some excess ice loaded with the sample and that their composition was not reported correctly. This may be a result of the relatively warm temperatures that their bulk samples were kept at compared to the bulk samples used here (256 K by Ma *et al.* ∼184/195 K here), or merely by an error in their calculation of their hydrate composition. Their exact method of preparation of the bulk sample was not mentioned, but it can be deduced that the ammonia would have been in a liquid state when preparing the bulk sample as the bulk sample was loaded at 220 K. It also cannot be determined whether the sample was loaded into a DAC as a liquid, or flash frozen in place as used in this study. Figure 5.7 is a reproduction of the figure from Ma *et al.* [2] showing their x-ray powder data, the x-ray wavelength used to obtain this data was quoted to be 0.4859 Å without error. Assuming the peak labelled as (210) in Figure 5.7 is ice VII then the pressure of their sample can be obtained by the ice VII equation of state, in the same way as the neutron data presented above. The peak labelled (210) in Figure 5.7 would actually be the (110) peak of Ice VII, the lattice parameter can therefore be found by finding the d-spacing of this peak through Bragg's law and multiplying that value by $\sqrt{2}$. Doing so produces pressures for Ma *et al.*'s powder patterns that are within 1-2 GPa of that determined by ruby fluorescence in the paper, which is remarkably close considering that this calculation was performed on data extracted from Figure 5.7 rather than the original data. This calculation only fails after the onset of the second transition at 25.8 GPa in Figure 5.7. The summary of the values used in calculating the lattice parameter of ice VII, followed by the pressure associated with this parameter is presented in Table 5.5.

The presence of a dehydration process all the way to AHH has potential consequences for the behaviour of ammonia inside planetary bodies. The

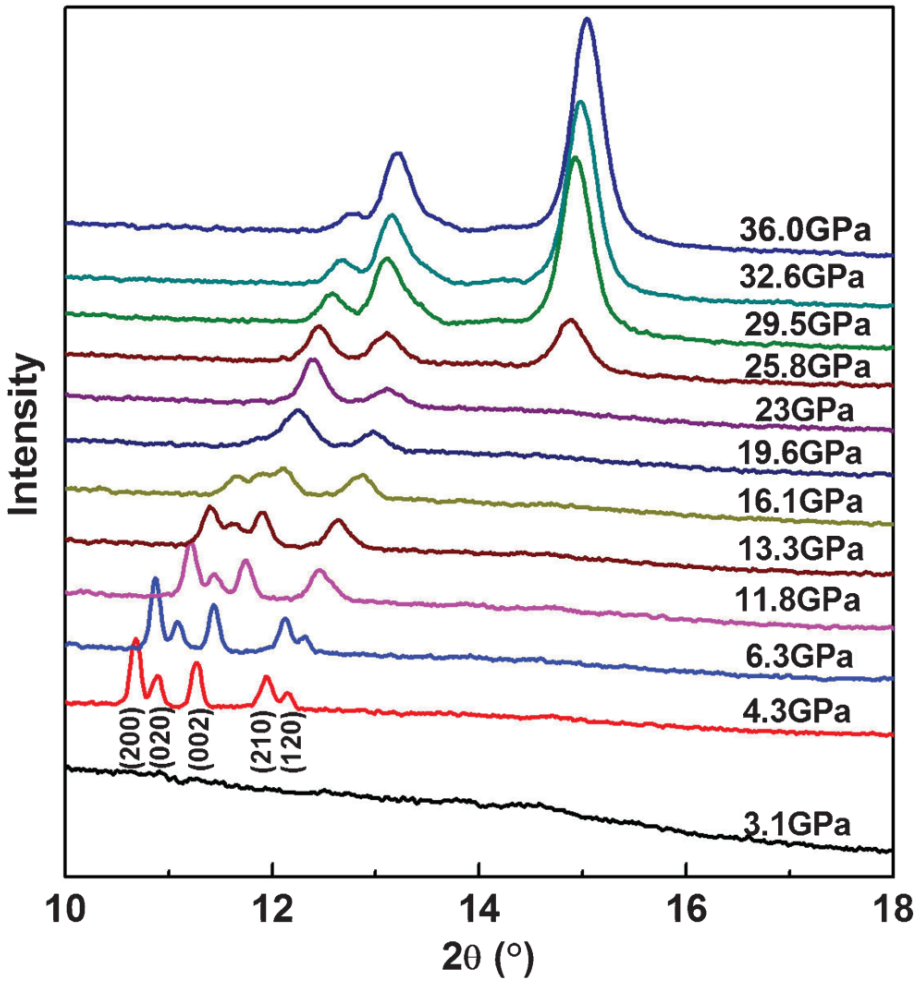

Figure 5.7 *A reproduction of Figure 3 from Ma et al. reproduced by permission of The Royal Society of Chemistry [2]. This represents powder data presented in 2θ format identical to the original figure. The pressures shown were measured by ruby fluorescence.*

ammonia content of the planetary nebula in the vicinity of Saturn is estimated in the range 10-15 % which would correspond to a composition of roughly half ADH and half ice by molar fraction [16]. Our results suggest that above 3.5(1) GPa in any body where solid phases form, this mixture will be almost 80% ice and 20% AHH by mass. A crude calculation of how the density of AHH-II compares to that of ice VII at this pressure produces the values of $\sim$1.45 g cm^{-3} and $\sim$1.83 g cm^{-3} respectively. These values were calculated from the atomic mass of the atoms contained in the unit cells of both AHH-II and ice VII, using the atomic mass of hydrogen rather than deuterium, divided by the volume of their respective unit cells as they appeared in the final refinement. This means that above this pressure there will be a chemical differentiation in any body containing ammonia and

Pressure From Ma *et al.* (GPa)	2θ of Ice VII (110) Peak (°)	Ice VII Lattice Parameter (Å)	Calculated Pressure (GPa)
4.3	11.94	3.303	3.86
6.3	12.11	3.257	5.63
11.8	12.45	3.169	9.96
13.3	12.63	3.124	12.77
16.1	12.83	3.076	16.32
19.6	12.95	3.047	18.77
23.0	13.06	3.021	21.2

Table 5.5 *The values extracted to calculate the "pressure" of the suspected ice VII peak in the work by Ma et al. The pressures quoted from their work was obtained from the ruby fluorescence method, and was published without errors. Values deduced from Figure 5.7 are also given without error as they are only being used to draw a simple comparison to the quoted pressures from Ma et al. [2]*

water so that energy can be released as the denser ice falls through the less dense ammonia hemihydrate. The existence of layering will also have consequences for heat flow and convection across any icy layer which will be important for models of heat flow inside planetary bodies. Finally, the fact that the greater part of any ice layer will be composed of water-ice free from any ammonia content provides an important constraint for the conductivity and other properties of such an ice layer. These results may also have important consequences for bodies where ammonia and water exist as fluids. Fluid ammonia and water are miscible in all proportions under the conditions currently explored (up to 4 GPa) and it is assumed that this is true for all pressures and temperatures. The fact that in solid phases ammonia and water appear to be progressively less miscible with increasing pressures raises the possibility that the fluids may also become unmixed at some pressure beyond that yet studied. This possiblity would have important consequences for models of the giant planets Uranus and Neptune.

Finally, it is important to note that AHH-II has a wide range of O-D···N, N-D···O and N-D· · ·N hydrogen bonds of differing lengths and geometry. If, as appears possible, it is stable over a wide pressure range it will provide a good system to explore the effects of changing geometry on H-bond strength over a wide range of densities without the complications of the abrupt structural changes brought about by structural phase transitions, provided a high resolution data set can be provided at each pressure step.

5.5 Concluding Remarks

In this chapter x-ray single-crystal and neutron-powder diffraction data have been used to deduce the structure of the phase AMH-V. However, this phase has been shown to actually be an ammonia hemihydrate phase and has been renamed as AHH-II. The structure has a monoclinic unit cell with a space group $P2_1/c$ and lattice parameters $a = 3.3584(5)$ Å, $b = 9.215(1)$ Å, $c = 8.933(1)$ Å and $\beta = 94.331(8)^\circ$, as found upon final refinement of the neutron-powder diffraction data collected at room temperature and a pressure of 3.5(1) GPa. This result means that the dehydration boundary reported by both Boone and Nicol [49] and Fortes *et al* [59] signifies a much larger release of ice than was previously thought. This may be significant for the modelling interiors of icy satellites such as Titan and Europa amongst others. The phase has also been shown to have a similar molecular packing to ice VII, which is also stable at similar temperatures and pressures to AHH-II.

Chapter 6

Single-Crystal Neutron Diffraction Study of Ammonia Hemihydrate

This chapter will look at the work that was conducted to attempt to solve the structure of an unexpected phase of ammonia hemihydrate that was observed first in a neutron powder experiment attempting to obtain a phase pure powder pattern of AHH-II. This new phase was grown as a single crystal in samples for both x-ray and neutron experiments, but a structure solution was not found. This chapter will also look at the phenomenon of multiple scattering, which was thought to have some effect on the data gathered in the neutron single-crystal experiments that could potentially effect the identification of reflections belonging to the sample examined on the SXD instrument. A Java-based computer program was written to look for potential multiple scattering events in the sample and analysis of the effectiveness of this program is discussed.

6.1 Complexities in the Ammonia Hemihydrate System

The AHH-II structure has so far only been observed in water-rich samples, those samples containing 50% molar volume water or more, as discussed in Chapter 5. While the structure seen in the work by Ma *et al.* [2] is consistent with the structure presented in Chapter 5, the water content of their sample was perhaps larger than the 2:1 ratio reported, as discussed in Chapter 5 Section 5.4. The

AHH-II structure should be able to be formed from a 2:1 molar ratio sample without any excess ice. This was first attempted on a powder sample prepared on the PEARL beam line at ISIS, using the same method used to form AHH-II from both 1:1 and 1:2 samples. The sample was loaded cryogenically as described in Chapter 4 Section 4.3.1 and cooled to check that the loaded sample produced the powder pattern of the structure of AHH-I. This is shown in Figure 6.1 and shows clearly that all peaks are explained exclusively by the AHH-I structure without any other phases present. The sample was then allowed to warm to room temperature and compressed in 10 tonne steps to 55 tonnes. The final powder pattern collected is shown in Figure 6.2 and shows quite clearly that along with both AHH-II and ice-VII peaks there are several other peaks that can be adequately described by ammonia-IV. While AHH-II has formed in a 2:1 sample, it is accompanied by both ice-VII and ammonia-IV. Looking back through the previous patterns collected as the sample was being pressurised, the powder pattern in Figure 6.3 was observed at a load of 32 tonnes. This is a poor powder pattern because of the low exposure time of approximately 10 minutes, and as such no meaningful refinement can be made against this data, but there are still some peaks present that seem to indicate a different structure forming from the melt.

From the force applied to the P-E press it would seem likely that the newly identified phase forms at a lower pressure than seen for the AHH-II phase, which is already known to form at 3.5 GPa (see Chapter 5). A single-crystal sample was prepared for x-ray study to permit accurate determination of the unit cell of the structure. A 2:1 ammonia-to-water hydrogenous sample was loaded into a Merrill-Bassett DAC with 300 μm culets using the same method as described in Chapter 4 section 4.3.1, with a ruby sphere pressure calibrant. The gasket material was steel, pre-indented to 87 μm with a hole size of 125 μm diameter. From this a single-crystal was grown at a pressure of 2.7(4) GPa, a much lower pressure than the crystal grown in Chapter 5. However, there were some optical differences between the sample grown here than the sample grown in Chapter 5. While the new sample still allowed light through cross polarisers, the shape of the crystal was very different from the samples in Figure 5.1 in Chapter 5. The crystal grown here had no straight edges observable, appearing to have curved edges and corners rather than the facets seen before. During preparation of the single-crystal sample other long thin straight edged crystals were also seen in the sample, but these were melted off. The single-crystal did not fill the entire sample volume, but did fill the majority of it. This sample was sent to the I15 beamline

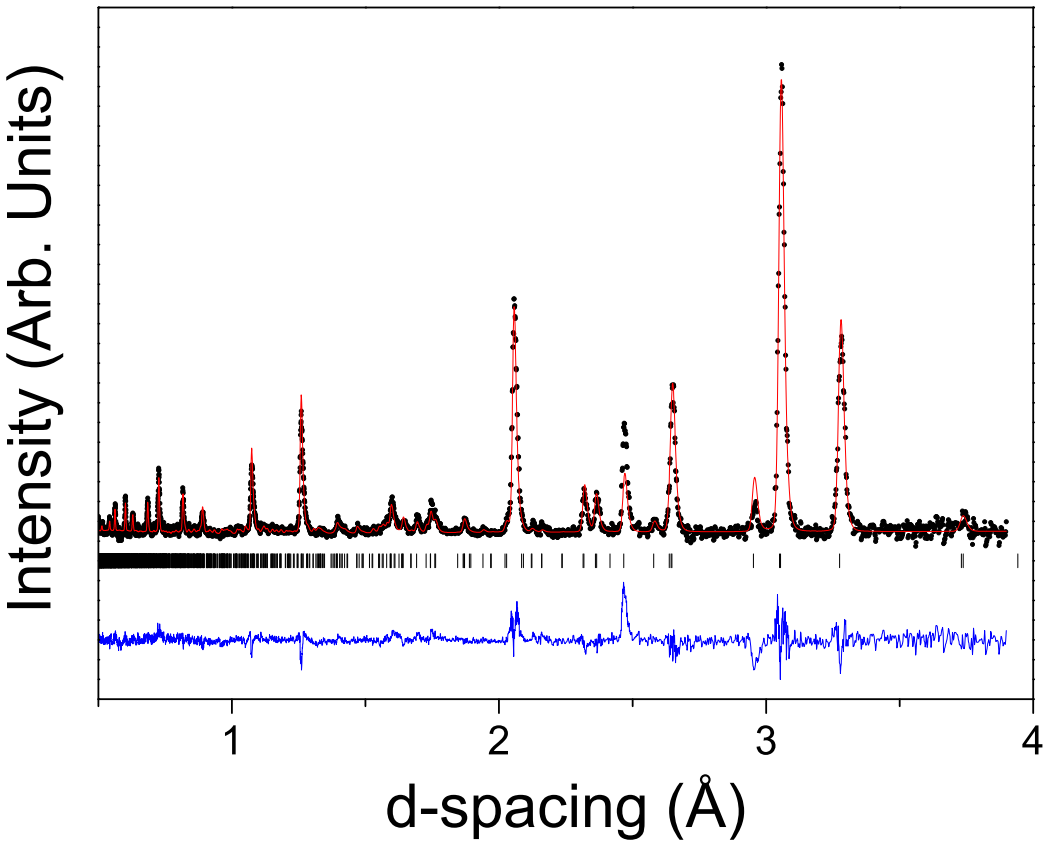

Figure 6.1 *Neutron powder pattern for the analysed sample of a 2:1 deuterated ammonia-to-water mixture at low temperature showing the AHH-I powder pattern. The black points are the collected data, the red line shows the fit of the Rietveld refinement of the AHH-I structure against the data, the blue line is the difference curve between calculated and observed intensity. The tick marks represent the reflection positions of the AHH-I phase.*

at the Diamond Light Source for data collection.

The detector used was a Mar345 detector. The beamline was calibrated with a silicon standard sample which determined the wavelength to be 0.4141(2) Å. The data were collected with an exposure time of 10 s per step angle of 0.5° over a ± 25° range either side of the cell's axis. From these data the following unit cell parameters were found; a = 6.319(3) Å, b = 5.322(2) Å, c = 6.456(2) Å, $\alpha = 90.11(2)°$, $\beta = 113.41(2)°$ and $\gamma = 90.33°$, with a suggested monoclinic space group of $P2_1/m$ from the systematic absences determined through the XPREP program [84]. This is very different than the AHH-II structure, and performing the same analysis used to determine how many molecules occupy the unit cell volume as was done in Chapter 5 it is also possible to determine the approximate contents of the unit cell. The unit cell of this phase has a volume of 199.2

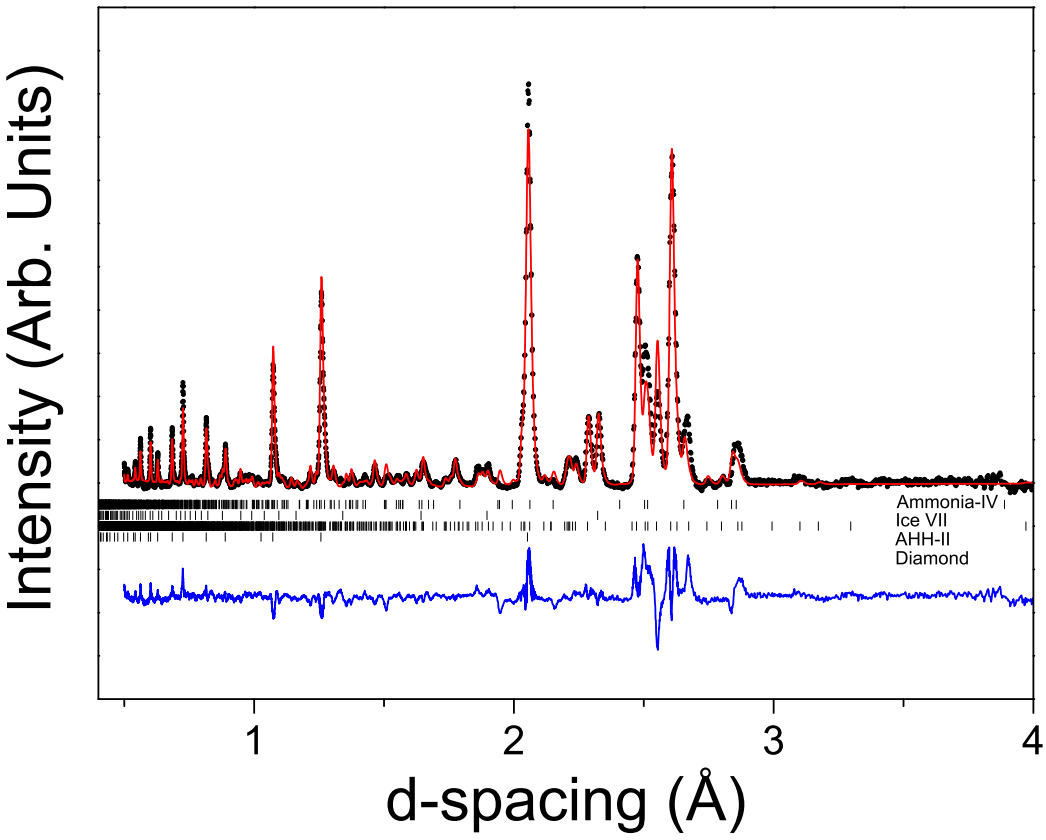

Figure 6.2 *Neutron powder pattern for the deuterated 2:1 sample at a load of 55 tonnes and the powder pattern contains peaks that can be attributed to AHH-II, ice-VII and ammonia-IV. The black points are the collected data, the red line shows the fit of the Rietveld refinement of the AHH-I structure against the data, the blue line is the difference curve between calculated and observed intensity. The tick marks show the peak positions of the four different phases included in this Rietveld refinement, the phases of these tick marks correspond to are named in order on the figure.*

Å^3, and comparing this to the equation of state of AMH-I gives ∼4.2 AMH formula units of AMH per unit cell ∼8.4 molecules of H_2O/NH_3, and thus most likely contains either eight or nine molecules. From these observations there is substantial indirect evidence to suggest that this phase is indeed unique, which unfortunately does not have a perfectly known composition as it did not occupy the entire sample volume.

In Chapter 5 it was mentioned that a deuterated 1:1 sample was prepared for a neutron single-crystal study. This sample was prepared for the purpose of determining whether the AHH-II structure did have site disorder between ammonia and water sites within the structure and to determine more accurately

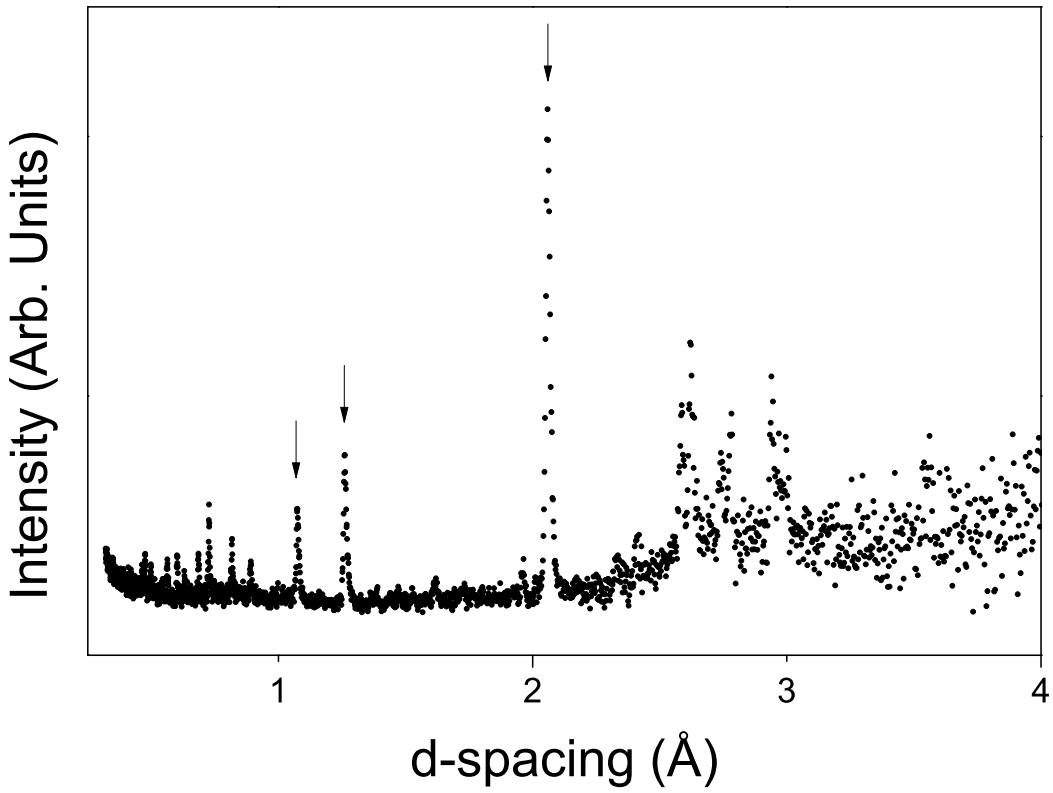

Figure 6.3 *Neutron powder pattern collected on a 2:1 ammonia-to-water ratio sample compressed at room temperature to 32 tonnes. Arrows show the strongest diamond reflections, it is quite clear with comparison to Figure 6.2 that the peaks at a high d-spacing do not belong to either ammonia-IV, ice-VII or AHH-II.*

the thermal parameters of the atoms within the structure. This sample was prepared in a panoramic DAC with 2 mm diamond culets. The gasket material was toughened CuBe of 1 mm thickness pre-indented to 0.99 mm, with a gasket hole diameter of 0.7 mm. Along with the 1:1 sample, a ruby sphere pressure calibrant was also included. The sample was taken up to a pressure of 3.09(3) GPa where it finally crystallised and a single crystal was prepared by melting the smallest crystallites and allowing larger ones to grow back until only one crystal remained. The crystal grown bore a closer resemblance to the single-crystal described above rather than the long thin crystals typical of AHH-II in Chapter 5 Section 5.1 and also failed to fill the entire sample. However, this crystal was observed to anneal over several months to have very well defined straight edges, but still failed to fill the entire sample. This sample was taken to the D9 beamline of the ILL, which has already been described in Chapter 3. In the set up of this experiment it was found that the diffraction peaks of the single-crystal could not be mapped successfully using an AHH-II unit cell. However,

this could be done with the unit cell determined above, suggesting that this new phase has been found a second time in a different composition sample. The data collected unfortunately had a non-uniform background on each individual frame scanned by the instrument. The cause of this background problem was not identified and this meant that no meaningful intensities could be extracted from the collected data preventing full structural analysis. However it can be confirmed that the sample had the same unit cell of the x-ray sample probed on I15 at Diamond.

6.2 Multiple Scattering in Neutron Single-Crystal Experiments

6.2.1 What is Multiple Scattering

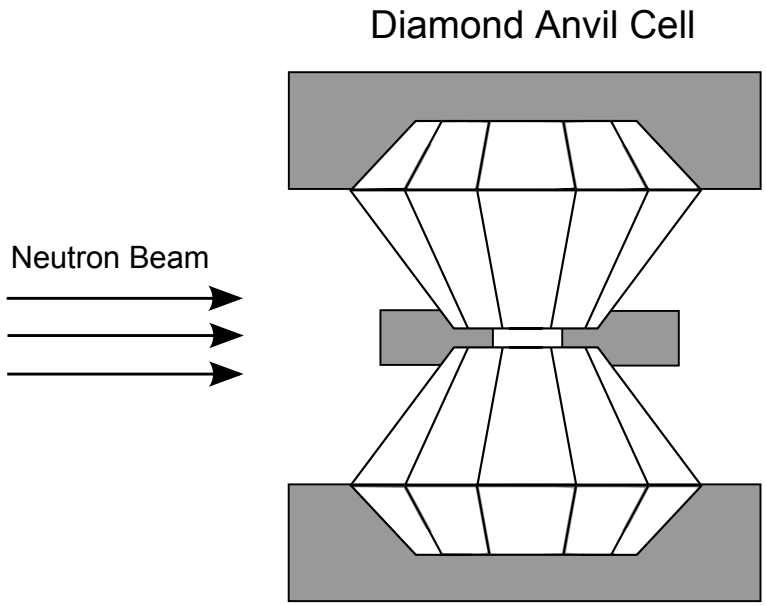

Figure 6.4 *A cross section of how the incident neutron beam enters the pressure cell in a neutron diffraction instrument, entering through the gasket rather than through the diamonds as with x-ray experiments. The neutron beam illuminates, and hence diffracts from both diamonds, the sample and the gasket.*

The neutron sample was also placed on the SXD instrument at the ISIS facility, in another attempt to solve the structure. However, this was also unsuccessful, but for different reasons than the experiment in the previous section. The SXD

instrument is a time-of-flight Laue diffractometer set up with six area detectors in the equatorial plane of the instrument [114], described in more detail in Chapter 3 Section 3.3.1. The cell has to be mounted vertically in the instrument, and the neutron beam passes through the gasket vertically to the central diamond axis (see Figure 6.4). The incident neutron beam not only illuminates the sample, but also the diamond anvils and the gasket. While the gasket material contributes powder diffraction peaks to the data recorded by the detectors, the diamonds contribute several intense Bragg reflections since the size of the diamonds being illuminated by the neutron beam are much larger than the sample. Also, as a result of their intensity, these intense Bragg reflections can go on to act as a secondary incident beam that can cause further diffraction in the sample. This phenomena is known as multiple scattering and has typically been looked at in the context of intense Bragg reflections causing further scattering within the same crystal structure [138]. This case of multiple scattering is shown in Figure 6.5 via the Ewald construction (see Chapter 2 section 2.3). The surface of the Ewald sphere contains two reciprocal lattice points on its surface in addition to the point at the origin. Here the diffraction condition is satisfied by reciprocal lattice vectors $\underline{K}_A = \underline{k}_i - \underline{k}_{fA}$ and $\underline{K}_B = \underline{k}_i - \underline{k}_{fB}$, however it is possible that if $\underline{K}_B$ is a strongly scattering reflection that the diffracted beam $\underline{k}_{fB}$ could diffract further as $\underline{K}_{AB} = \underline{k}_{fB} - \underline{k}_{fA}$, adding to the intensity of the $\underline{K}_A$ reflection. This is the same as saying that the diffracted beam $\underline{k}_{fB}$ acts as a secondary incident beam so that the intensity of the diffracted primary beam and a secondary diffraction event from a particularly strongly scattering reflection.

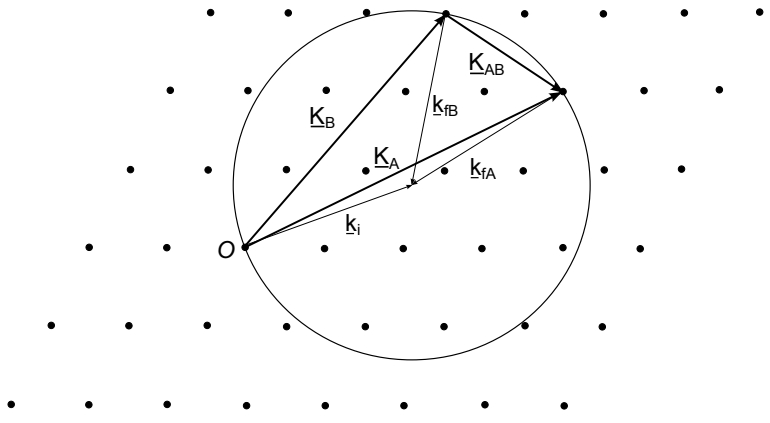

Figure 6.5 *A multiple scattering event shown as an addition of two scattering vectors where the ends of the vectors both lie on the surface of an Ewald Sphere, illustrated here as a circle*

The situation in Figure 6.5 is shown for only one $\underline{k_i}$, hence a fixed wavelength. It is also only shown on a single-crystal lattice, and so these extra diffraction events will only occur and affect the intensities of reflections that correspond to a general lattice vector of that reciprocal lattice. In a Laue or time-of-flight configuration there is a range of incident wave vectors available for diffraction (see Figure 2.6 in Chapter 2 Section 2.3) so it is possible for this situation to occur more frequently. Additionally, the set up of the SXD instrument itself means that there is another form of multiple scattering that could cause problems in data collection.

The SXD instrument has six area detectors that surround the central sample position centred on the equatorial plane of the instrument. It has five further detectors that sit under these six, but these are not used in high-pressure experiments as the cell body prevents any useful data being recorded on these detectors. This gives nearly 360° of reciprocal space access around the equatorial plane of the instrument. This large reciprocal space access means that all diffracting elements will be recorded in these detectors, the two diamonds, the sample and the gasket. In addition to this, a particularly strong reflection could act as a secondary incident beam to the other objects in the neutron beam. Reflections like this would be primarily from the diamonds as these are the largest objects in the neutron beam. This produces extra reflections in the detectors that would not appear to be caused by either of the diamonds or the sample. This situation is shown in Figure 6.6.

The detectors record both the intensity of the diffraction peaks as well as the time that they are recorded on the detector. From this information, and prior knowledge of the unit cell of the crystal you are collecting data from, the UB matrix can be calculated. The UB (or orientation) matrix is a mathematical construct that is unique to the unit cell of the structure. It translates the *hkl* values for a given reflection into the k-space (momentum space) scattering vector ($\underline{K}$) that is produced for that reflection. In other words, given the *hkl* indices (or lattice vector) of the structure, the UB matrix maps this to detector space, the point on the detector that the Bragg reflection corresponding to that index will be detected. This also means the inverse of the UB matrix maps the $\underline{K}$ vectors measured by the detector to *hkl* values of the corresponding unit cell. If several reflections exist that cannot be explained by the UB matrix, this complicates the matter of determining the UB matrix of the cell, especially if these extra reflections have intensity of the same order of magnitude as the signal from the sample itself.

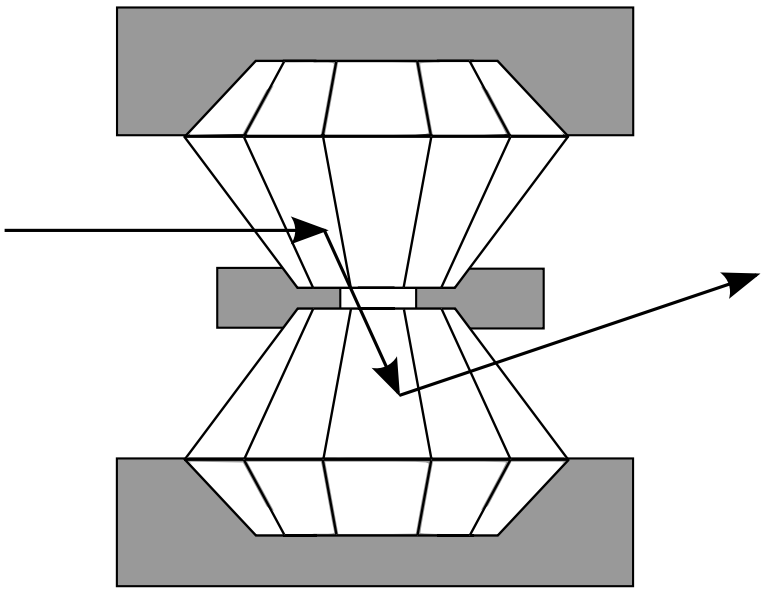

Figure 6.6 *The primary neutron beam can be diffracted from the diamond anvil and then enter the other diamond anvil where is diffracts again. The neutron beam path described is represented above using arrows. This situation can also be thought of as a multiple scattering event.*

Typically on the SXD instrument, reflections that are caused by the two opposing diamonds have to be identified first so that these reflections are excluded before attempting to find the UB matrix of the sample. It is at this point that any multiple scattering events that do not lie on the reciprocal lattice of the diamonds could be erroneously identified as belonging to the sample.

The order of diffraction from the objects is important, and as a result, from the three single crystal objects illuminated by the neutron beam there are six potential multiple scattering pairs:

- The first diamond followed by the second diamond
- The first diamond followed by the sample
- The sample followed by the first diamond
- The sample followed by the second diamond
- The second diamond followed by the sample
- The second diamond followed by the first diamond.

Of these six pairs, only two do not depend on the sample, and these were the only pairs considered because the diamonds are much larger than the sample itself, meaning that the most intense multiple scattering events are going to be from interactions between the diamonds.

6.2.2 Looking for Multiple Scattering Events in SXD Data

To calculate whether a reflection that has been detected could potentially be explained by a multiple scattering event, some mathematical manipulation has to be performed. To do this first the UB matrices of the diamonds are required to be known, and the method of calculating the co-ordinates of each reflection in SXD detector space is also required to be known.

Each reflection, once stored in the SXD data file, has the following data recorded which is of interest; The X co-ordinate of the reflection and the Z co-ordinate of the reflection, both of these are in terms of detector pixel number which will be explained later, the time-of-flight of the reflection measured in μs, the error measured in these three values, and which detector the reflection has been recorded in. Along with the data entries to be analysed, the UB matrices of both diamonds and rotation matrices of the sample are also held in the data file. This information, along with the SXD parameters describing the location of the centre of the detectors, the sample-detector distances and the neutron source-sample distance are all that is needed to reconstruct the geometry of SXD mathematically.

The detectors on SXD have their positions recorded in terms of the "longitude" and "latitude" of the central pixel of each detector, where the 0° point is defined by the incident beam, see Figure 6.7. each pixel in the SXD detector bank is 3 mm X 3 mm in size and there are 64 pixels per detector, so from the detector centre it is possible to find the lattitude and longitude of the reflection in question from the following equations:

$$\begin{aligned} R_{Lat} &= R_{Lat_{CP}} + \tan^{-1}\left(\frac{Z_{pix} \times 3}{S_{distance}}\right) \\ R_{Long} &= R_{Long_{CP}} + \tan^{-1}\left(\frac{X_{pix} \times 3}{S_{distance}}\right) \end{aligned} \tag{6.1}$$

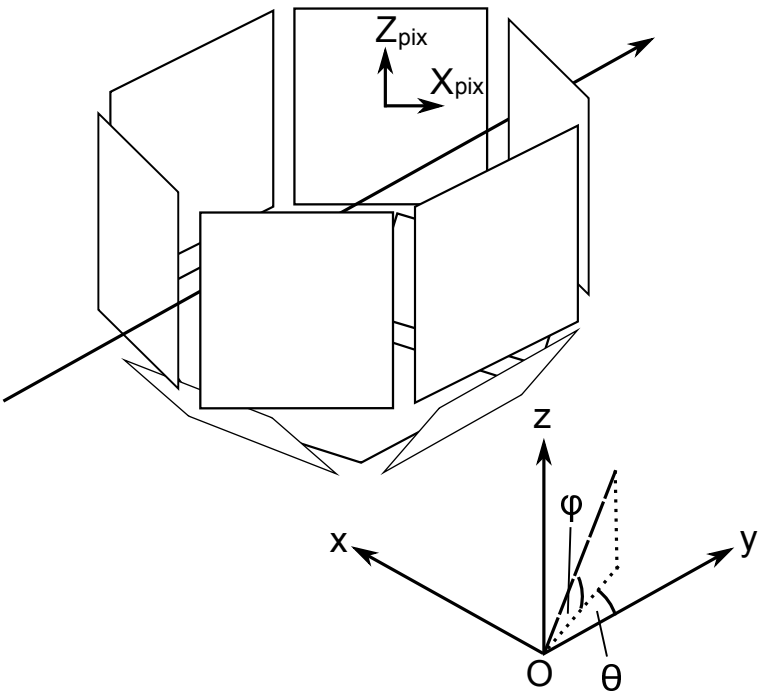

Figure 6.7 *An isometric representation of the SXD detectors is shown along with the detector axis as defined by the SXD software, including the latitude (ϕ) and longitude (θ) positive directions and the origin (O) which lies at the centre of the instrument. Note the left-handed co-ordinate system, and that each detector has its own local co-ordinate system Xpix and Zpix, which lie across the surfaces of the detectors with an origin at the centre, shown for one individual detector in the diagram. The large arrow shown passing through the instrument shows the direction of the neutron beam.*

Here R_{Lat} is the latitude of the reflection, $R_{Lat_{CP}}$ is the latitude of the central pixel of the detector, Z_{pix} is the pixel co-ordinate relative to the central pixel and $S_{distance}$ is the sample-to-detector distance. The longitude equation uses very similar labels, the orientation of the X_{pix} and Z_{pix} axes are shown in Figure 6.7. From these values it is very simple to calculate the $\underline{k}_f$ vector of the reflection in terms of the detector axes.

$$\begin{aligned} k_{f_x} &= \frac{1}{\lambda}\left(\sin(R_{Long}) \times \cos(R_{Lat})\right) \\ k_{f_y} &= \frac{1}{\lambda}\left(\cos(R_{Long}) \times \cos(R_{Lat})\right) \\ k_{f_z} &= \frac{1}{\lambda}\sin(R_{Lat}) \end{aligned} \tag{6.2}$$

where λ is the effective wavelength of the incident neutrons which depends on their time-of-flight. This $\underline{k}_f$ vector has been calculated just from the observed intensities and time-of-flight of the neutrons incident upon the detector. To see whether this reflection could be caused by a multiple scattering event, this vector needs to be able to be produced by a multiple scattering event as described earlier. An assumption is made at this point that the time-of-flight of the neutron will not be changed significantly by the small extra distance travelled in the multiple scattering event. Therefore, the neutron wavelength of the detected reflection will be the same as the wavelength used in the multiple scattering calculation. So for each reflection that is identified, and not indexed as either of the diamonds, it is possible to reconstruct the Ewald sphere for that reflection. Once this is done the UB matrices of the diamonds can be used to see if there are diamond reflections that also lie on the same Ewald Sphere as this reflection. If a diamond reflection is on the Ewald sphere, then a second search can be made to determine if a reflection caused by the other diamond would cause some intensity to be scattered onto the position of the detected "reflection".

As this would require several mathematical procedures to determine whether a reflection could be caused by a multiple scattering event, the entire process was coded as a java program so that each reflection could be checked automatically. This code is included in the supplementary electronic material of this thesis, along with the input data file consisting of the unassigned reflections from the SXD data file used and the output file generated by the program.

The operation of the Java program is quite simple. Using equations 6.1 and 6.2 the $\underline{k}_f$ vector of each reflection is calculated with respect to the instrument centre compared to the position on the detector, and its magnitude is then calculated. For a number of *hkl* values of the diamond UB matrices, which have already been determined, the magnitude of the $\underline{k}_f$ vector is calculated and compared to the length of the $\underline{k}_f$ vector that was recorded by the detector. If the vector lengths are close enough to each other then that reflection is stored for further analysis. There is a hard coded parameter within the program called "hklcycle" which determines the largest h k and l index that is looked at. The $\underline{k}_f$ magnitude length acceptability is determined by a series of hard coded parameters all of which share the suffix "lengthtol" allowing magnitude to vary from the desired value by 5%.

Each candidate multiple scatterer that is stored in this fashion becomes the input for the next stage of calculation. Each of the stored possibilities is then used

to calculate the final scattering vector $\underline{K}$ required to produce intensity on the detector in the desired location of the detector. A further cycle through h, k and l is performed and the scattering vectors produced by both the first UB and the second diamond UB matrix are calculated for that reflection. If the components of the scattering vector produced by the UB matrix match the components of the scattering vector $\underline{K}$ required to produce a reflection in the required place in the detector, this combination is labelled as a multiple scattering event and passed to the output file. The allowed variation of the vector from the ideal value previously calculated is defined by a series of hard coded parameters which all share the suffix "vectortol" allowing the vector components to vary from the desired values by 5% also.

The entire process is repeated for the reverse situation, where the incident beam is diffracted by the second diamond first, followed by the first diamond, and also for internal second diamond reflections. After this has been done for one reflection, the program moves onto the next reflection and starts again. Each *hkl* combination is also checked to see whether the combination is allowed by the diamond space group, if it is not, the possibility is ignored.

6.2.3 Analysis of Implemented Solution

The input file consisted of 114 reflections which were extracted from the SXD data file after being checked to be neither noise or an erroneously recorded powder diffraction line from diffraction of the gasket material. The output file produced highlights 30 of these 114 reflections as possibly arising from multiple scattering events, roughly 26% of the observed reflections. Figure 6.8 shows a view of the SXD data plotted in reciprocal space, showing the apparent $\underline{K}$ of each detected reflection. If the detected reflections were all caused by diffraction of the sample, and the sample was a single-crystal, all of the points would line up on a lattice. This is obviously not the case for either of the data sets presented.

Another observation from the output file is that several data points flagged as possible multiple scattering events have many potential combinations of $\underline{K}$ vectors from that would produce the desired result, however, many of these have large deviations from the $\underline{k}_f$ magnitudes that define the Ewald sphere. This suggests that the 5% error margin was too generous, and that this should be reduced for future analysis. The majority of the multiple scattering events highlighted also involve low *hkl* indexed reflections of the diamonds, which are the diamond

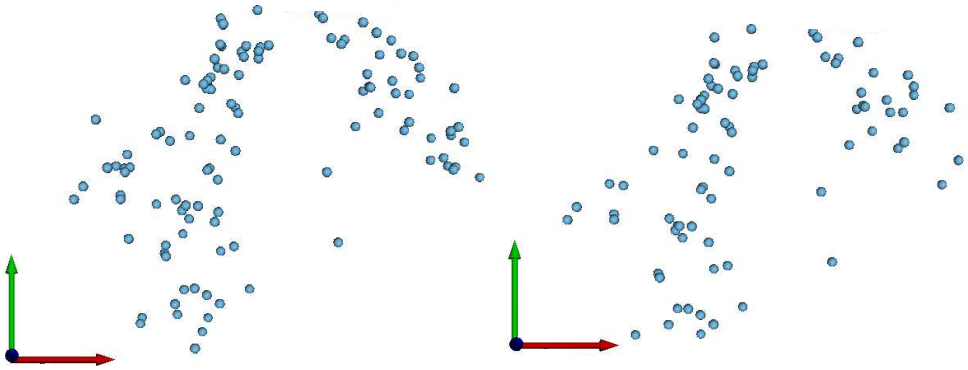

(a) *Reciprocal space plot of unknown reflections before being run through program*

(b) *Reciprocal space plot of unknown reflections after being run through program*

Figure 6.8 *Reciprocal space representations of the unknown reflections both before and after running the program. Placed side-by-side for ease of comparison. They are both in the same orientation shown by the coloured axes in the figures.*

reflections with the largest intensities. The observed reflections that are initially scattered by strong intensity, low *hkl*, diamond reflections are therefore the most likely to be genuine multiple scattering events than those that are a combination of high *hkl* indexed reflections.

The output also shows several reflections that can be highlighted either by internal diamond reflections or by an initial or final scattering event by a scattering vector with *hkl* index (000). This is actually just a reflection that occurs within the specified error to a diamond reflection, the other reflection indexed along with the (000) reflection. This would suggest that either the error chosen was either too large or perhaps that the diamond UB matrices have failed to index certain diamond reflections.

Unfortunately, the reciprocal space maps shown in Figure 6.8 show conclusively that the analysis performed on the data has not removed data points to the point of being able to identify a single set of lattice points identifiable as a single-crystal. There are several reasons that could account for this which will be looked at here.

It could be possible that diamond-sample multiple scattering effects are more important that first thought, and that reflections that obscure the underlying reciprocal lattice are a result of these effects. However, as $\sim 26\%$ of the recorded reflections were already flagged as potentially being caused by diamond-diamond multiple scattering events, as the analysis program stands, it may flag the majority of the data set as potential multiple scattering events. Also, as long

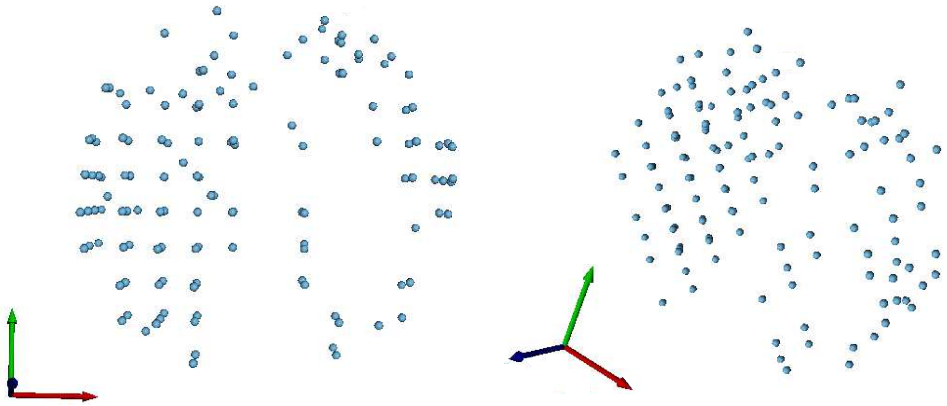

(a) *Reciprocal space plot of diamond reflections with an orientation showing lattice points lining up*

(b) *Reciprocal space plot of diamond reflections with a different orientation showing lattice points lining up*

Figure 6.9 *Reciprocal space figures showing two different orientations of the reflections identified as diamond reflections, that show that the lattices line up well. The three coloured axes indicate the relative orientations of the figures shown.*

as the lattice of the sample remains unknown, it cannot be considered without a much more complicated program.

Another possibility is that the method of calculation of $\underline{k}_f$ vectors in the written program may have a small systematic error. Only the centre point of the detectors is at the sample-to-detector distance stated and used in both SXD and the program in the supplementary material. This means that any reflection recorded away from the centre of the detectors will have a small increase in the sample-to-detector distance, which is most prominent at the edge of the detectors. Whether this forms a large error in the placing of the reflections in reciprocal space can easily be seen by plotting the reflections allocated to either of the diamonds in the SXD data file. This is shown for two orientations of reciprocal space in Figure 6.9. The reflections assigned to one of the diamond UBs line up in an obvious lattice arrangement with minor deviations from the ideal points in the lower half of the figures, but those at the top appear much more disordered, so it would seem that this systematic error is of minor importance. However, there appears to be some form of calculation error of the points that appear towards the top of the reciprocal space plots in Figure 6.9. This will need to be addressed if the deviations allowable to both $\underline{k}_f$ magnitude and calculated $\underline{k}_f$ vector within the program is to be reduced, and needs to be considered when analysing the reciprocal space plots in Figure 6.8.

Another problem is that the SXD instrument itself is not a fully calibrated instrument. Only some parameters of the instrument have been calibrated on the six detectors of interest. These parameters are the sample-to-detector distance, latitude offset, longitude offset, Z offset of the centre of the detector and the time-of-flight offset. Some parameters remain unknown, for example, the degree of tilt of the detectors from the vertical, and all the parameters for the detectors that do not lie on the equatorial plane of the instrument. In the normal operation of the SXD instrument these parameters are determined for every sample separately by fitting the diamond lattice to the accepted values. If the instrument was fully calibrated, and the small adjustments that this would involve taken into account, this could lead to a further increase in the accuracy of calculated $\underline{k}_f$ vectors and magnitudes.

Another minor concern is that the extra distance travelled by the diffracted neutrons during the multiple scattering events. This would lead to a change in the wavelength used in the calculation of the $\underline{k}_f$ vectors, however, accounting for this would mean treating each possible multiple scattering combination separately, as they would have different geometries and therefore induce a different change in the neutron wavelength. This would increase the complexity of the calculation considerably without a considerable improvement of the calculation itself.

All the possible places where the program could be improved upon that are highlighted above will provide only small improvements. The effect of implementing these small improvements is the improved calculation of $\underline{k}_f$ vector directions and magnitudes, increasing the confidence of correctly identifying multiple scattering events while allowing for lower tolerances on both vector directions and magnitudes, and in fact accounting for these is irrelevant for high tolerances, as the possible deviations that these effects could account for would be much smaller that the tolerance of both vector direction and magnitude.

6.3 Concluding Remarks

While data collected from both Diamond and the ILL suggest that there is a different phase that is observable in 2:1 ammonia-to-water samples, only the unit cell was able to be determined for this phase. The parameters are $a = 6.319(3)$ Å, $b = 5.322(2)$ Å, $c = 6.456(2)$ Å, $\alpha = 90.11(2)^\circ$, $\beta = 113.41(2)^\circ$ and $\gamma = 90.33^\circ$ with the likely space group $P2_1/m$ at a pressure of 2.7(4) GPa at room

temperature.

The sample was also investigated on the SXD instrument at the ISIS facility, with much less success, being unable to identify peaks belonging to the sample matching the unit cell parameters identified by the previous experiments. An attempt to remove reflections in the data provided by SXD that may have been caused by multiple scattering effects was made. The recorded reflections that were a result of neither of the diamond anvils were extracted from the data file and were fed into a computer program that was written to test whether any of these data points could be caused by a multiple scattering event.

The output of this program was considered and discussed, but ultimately did not prove helpful in identifying the crystal structure of the sample. While removing peaks which may constitute contributions from multiple scattering events may indeed cause problems with identifying true sample reflections, a great deal more analysis on the matter may be required than the simple attempt presented here.

Chapter 7

The Transition from AHH-II to the Disordered Molecular Alloy Phase

One of the most interesting phases of the entire ammonia-water system is the disordered molecular alloy (DMA) phase. This phase is a body centred cubic (bcc) phase where each bcc site is occupied by either an ammonia or water molecule. In addition to the bcc site disorder, the hydrogen atoms are also disordered in the [111] and [110] crystallographic directions. The probability of a bcc site being occupied by an ammonia or water molecule is determined by the stoichiometry of the ammonia hydrate. For example, the DMA phase exists in both ammonia monohydrate (AMH) and ammonia dihydrate (ADH) as the phases AMH-VI [51] and bcc-ADH [59, 61]. These two different compositions of DMA were both obtained in similar regions of phase space where samples of AMH and ADH were both cooled to liquid nitrogen temperatures and compressed to 5-6 GPa [51, 59, 61]. These phases could then be recovered to room temperature, without decomposition to ammonia hemihydrate (AHH) and ice. However, ADH would only transform to DMA if it was amorphous before compression [61].

Additionally, Ma *et al.* [2] reportedly found the DMA phase of AHH, but the P-T path followed to form it was very different to the path followed by Loveday *et al.* [51, 61]. Instead the AHH DMA phase was formed by compression at room temperature at 19.6 GPa [2], which is much higher than the transition pressures for the DMA phase in the water-rich ammonia hydrates. As all three stoichiometric ammonia hydrates can form this same structure, it seems possible that a solid solution could exist between these three different hydrates, but for

this to be possible the DMA phase of AHH needs to be stable under similar P-T conditions to both AMH and ADH DMA phases.

The work presented in this chapter was performed with the intention of forming the AHH DMA phase at P-T conditions similar to that of AMH and ADH DMA phases. Samples of AHH were studied by neutron diffraction methods to see if the AHH DMA phase could also be formed, following the same P-T path as Loveday *et al.* [51, 61]. Deuterated samples loaded with ammonia-to-water ratios of 2:1, 1:1 and 1:2 were also studied in an x-ray diffraction experiment to see if deuterated samples also transformed to the DMA phase in the same way. Finally 2:1 samples were heated at pressure to look for further high-pressure, high-temperature phase transitions.

7.1 Neutron Powder Diffraction Study

Three separate samples were prepared to look for a transition in AHH to a DMA phase by following the same pressure-temperature path that produced the DMA phase in both AMH and ADH as seen by Loveday *et al.* [51, 61]. These samples were prepared using the same preparation method as used in Chapter 4 Section 4.3.1, and all three samples behaved very similarly. Two loadings did not have the ideal 2:1 ammonia-to-water molar ratio, which was clear from the diffraction pattern collected at the sealing loads of the samples. No pressure markers were used in any of these samples to avoid any overlapping peaks in any intermediate phases obtained during compression. Despite this, all of the samples behaved in a same manner, producing very similar diffraction patterns. Figure 7.1 shows the diffraction pattern of the sample with the ideal 2:1 ammonia-to-water ratio at its initial sealing load of 5 tonnes. Figure 7.2 shows how this sample behaved under compression at a temperature of 170 K. These plots are shown separately because the initial diffraction pattern peak intensities are much larger than the subsequent peak intensities after the application of load. This can most clearly be seen with the comparison between the peak intensities of diamond to sample peak intensities in the two figures. The final phase, shown in the top diffraction pattern in Figure 7.2 was recoverable to room temperature and contains too many peaks to be DMA. Despite the extreme overlapping, 3–4 peaks can be identified above the strongest diamond peak. Furthermore the sample does not appear to be AHH-II, as the relative peak heights are incorrect compared to the diffraction pattern shown in Figure 5.4. The peaks are also too close together in d-spacing

for these peaks to be a combination of ice-VIII and DMA.

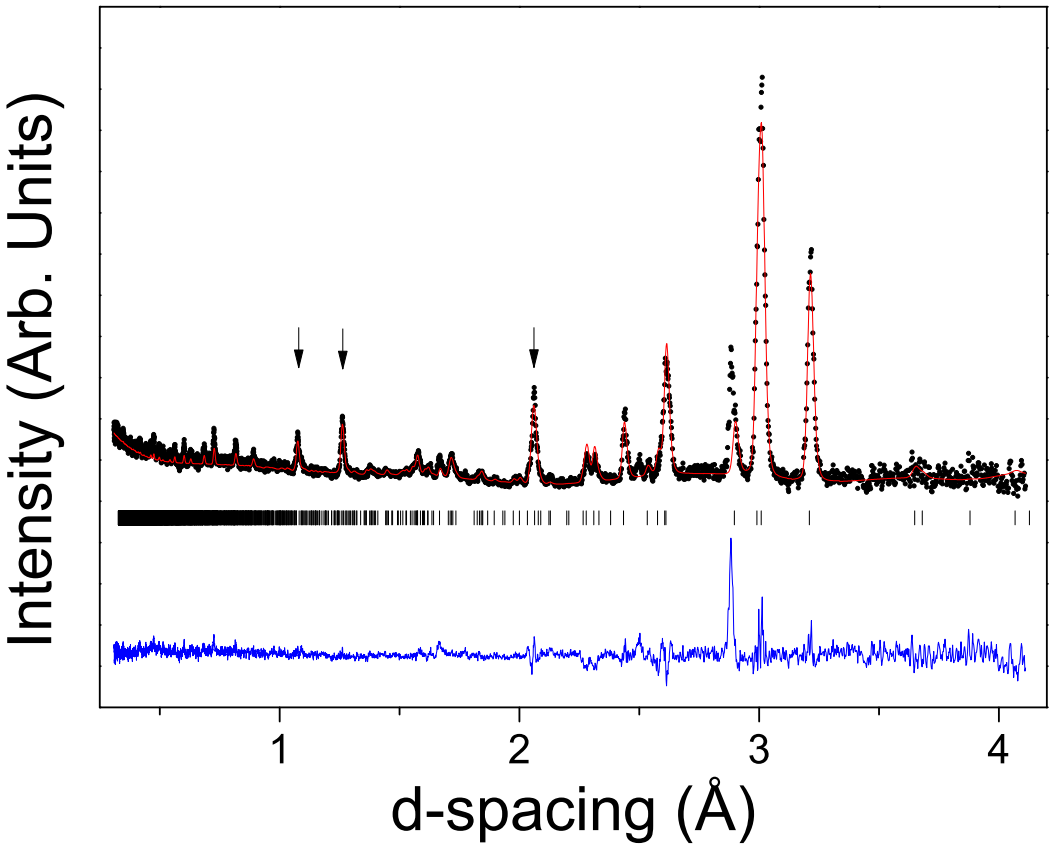

Figure 7.1 *The neutron powder diffraction pattern of the sample at the sealing load of 5 tonnes. The black circles show the collected data and the red line shows the Rietveld refinement to the AHH-I structure. The blue line is the difference curve between observed and calculated intensities. The tick marks show the expected positions of the AHH-I diffraction peaks. The arrows show the three strongest diamond diffraction peaks.*

Figure 7.3 show the end results of the other two samples that did not have a 2:1 ammonia-to-water ratio and contained some AMH-I along with the AHH-I in the diffraction patterns collected at 170 K with sealing loads of 5 tonnes. This error in the composition of these samples was possibly a result of a leaks in the valves used in the preparation of the bulk samples. It can clearly be seen in Figure 7.3 that the end state of all three samples shows significant differences in relative peak heights, which would suggest that the diffraction patterns shown are of a mixed phase. The three powder patterns shown in Figure 7.3 are not of sufficient quality to perform a full Rietveld refinement. However, by just considering the three to four peaks visible in each of the plots some simple observations can be made. Firstly, the mixed phases are unlikely to be caused by a mixture of DMA

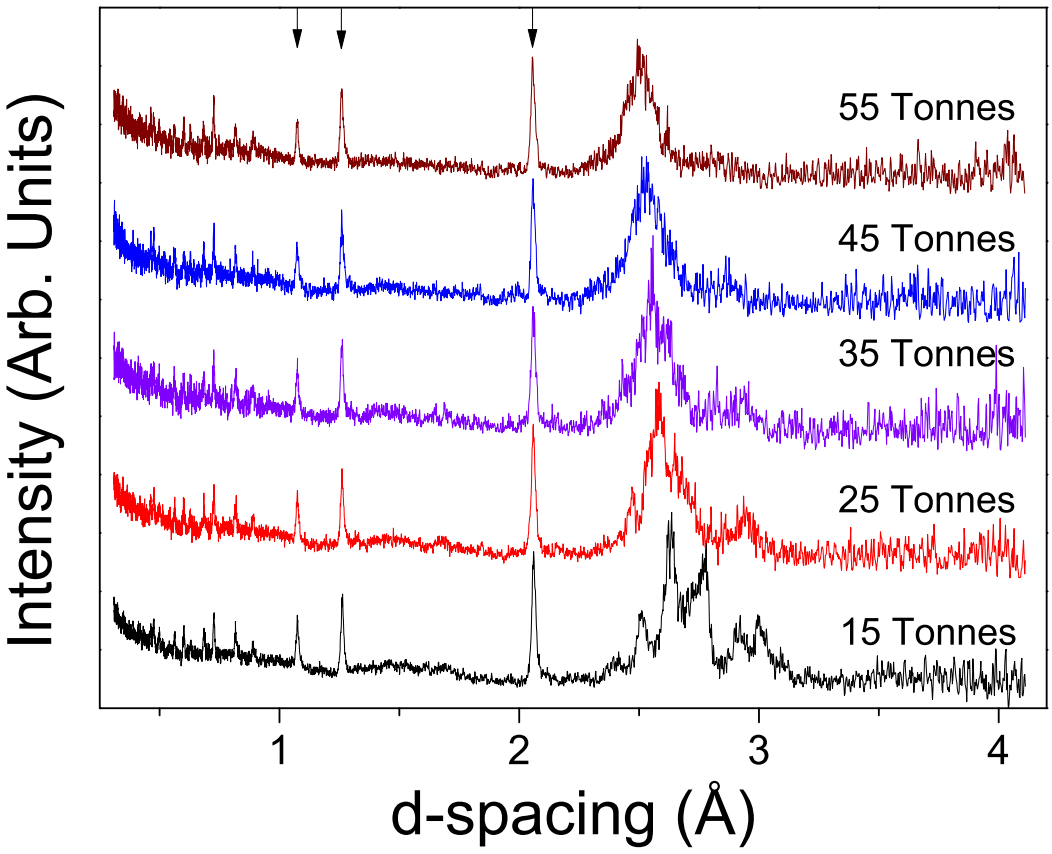

Figure 7.2 *Neutron powder diffraction patterns of the sample closest to an ideal 2:1 ammonia-to-water ratio upon compression at 170 K up to 55 tonnes of load on the P-E press in 10 tonne steps. The bottom pattern is the lowest load of 15 tonnes, which is also obviously different from the AHH-I diffraction pattern seen in Figure 7.1. The arrows show the three strongest diamond diffraction peaks.*

and ice VII or VIII, as the d-spacing of these peaks are too large compared to the pressure of the samples suggested by the loads they were collected at. For the three plots shown in Figure 7.3, from top to bottom these lowest d-spacing peaks are seen at approximately 2.33 Å(blue), 2.32 Å(red), and 2.30 Å(black), and this corresponds to a pressure of approximately 4.7 GPa, 4.1 GPa, and 5.8 GPa respectively. Comparing this to the load of the P-E press when the data were collected (85, 55 and 85 Tonnes respectively) and the sample pressure that can be estimated from this (∼7-8 GPa, ∼4-5 GPa, and ∼7-8 GPa respectively). This shows that attributing the lowest d-spacing peak to the (110) ice VII peak in the cluster of overlapping peaks in all of the patterns in Figure 7.3 underestimates the pressure expected from the load applied to the P-E Press [126].

As these three experiments failed to produce the DMA phase in AHH by following

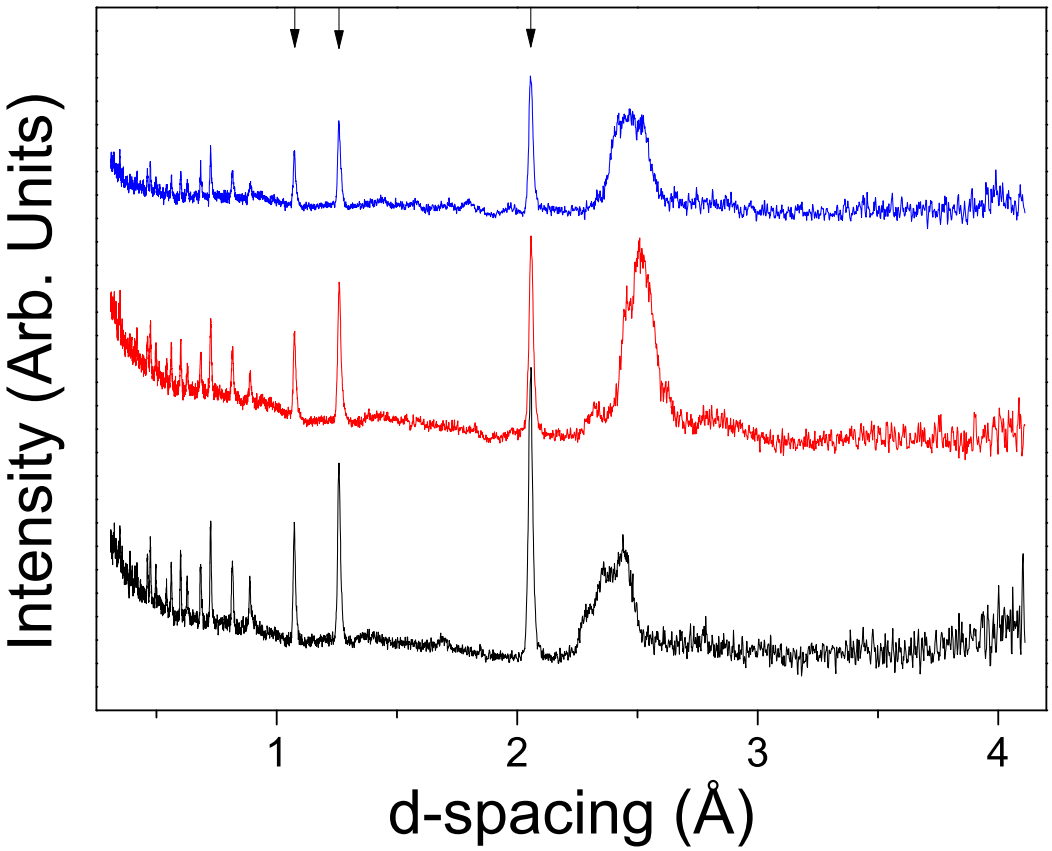

Figure 7.3 *Neutron powder diffraction patterns of the three samples recovered to room temperature as described in the text. The middle pattern is from the same sample in figure 7.2. The arrows show the three strongest diamond diffraction peaks.*

the same P-T path that forms the AMH and ADH varieties of DMA, a different approach will be needed. It has already been shown in Chapter 5 Section 5.3 that the distribution of molecules in AHH-II, while being fully ordered, gives N and O positions similar to those found in bcc DMA and pseudo-bcc ice VII. Therefore, a transition to DMA from AHH-II would require that only the hydrogen bonds re-orient. This could be done by either heating to encourage rotation or increasing pressure to encourage proton exchange between the molecules. The compression method has previously been investigated by Ma *et al.* [2] with a hydrogenous sample. The compression case was investigated again here with deuterated samples, so an easier comparison to the work presented earlier in this chapter and in Chapter 5 Section 5.2 could be made.

7.2 Room–Temperature Compression of Deuterated Samples

Deuterated samples were loaded as described in Chapter 4 section 4.3.1 into DXR cells with tungsten gaskets for the high-pressure x-ray experiment along with a ruby sphere for pressure determination as described in Chapter 4 Section 4.3.2. Tungsten was found not react with ammonia and water samples unless they were heated. DXR cells have already been described in Chapter 4 Section 4.1. The samples were deuterated to allow for easy comparison with the previous neutron experiments, and tungsten was used as gasket material since steel gaskets are known to react with ammonia and water at high pressures/temperatures [46, 47, 49]. Three samples were prepared, each loaded with a different ratio of ammonia-to-water; 1:2, 1:1 and 2:1. The x-ray study was conducted at the Diamond synchrotron on the I15 beamline with an x-ray beam energy of 29.2 keV with a 50 μm pinhole. The x-ray wavelength was determined to be 0.4254(2) Å by use of a silicon standard sample.

Figures 7.4, 7.5 and 7.6 show waterfall plots of the x-ray powder data collected for the 2:1, 1:1, and 1:2 ammonia-to-water ratios respectively, increasing from low pressures up to a maximum of 41 GPa. The 2:1 and 1:1 plots (Figures 7.4 and 7.5 respectively) show very similar behaviour between the different samples. Each show the three main peaks of AHH-II persisting up to ∼26.5 GPa, after which, a transformation to a single bcc peak, observed at a d-spacing of 2.20 Å, that corresponds to the DMA phase. The 1:1 sample shows a large ice VII peak along with the peaks caused by the AHH-II structure. However the 1:2 sample (Figure 7.6) shows very different behaviour. In that sample, first the excess ice freezes out before the entire sample solidifies (as described in [59]), but upon solidification the sample displays only a single bcc peak which is the characteristic signal of DMA in these samples. The reason for this atypical behaviour could be caused by the excess ice-VII, which froze out before total solidification of the sample, acting as a seed crystal (remembering that the structures of ice VII and DMA are very similar as discussed in Chaper 5 Section 5.3) or could be a result of the relatively rapid compression from liquid to solid phases.

The behaviour of the 1:2 sample is particularly anomalous when compared to a similar compression study that was performed on a neutron experiment, the data for which is shown in Figure 7.7. This Figure shows a pressure evolution of the

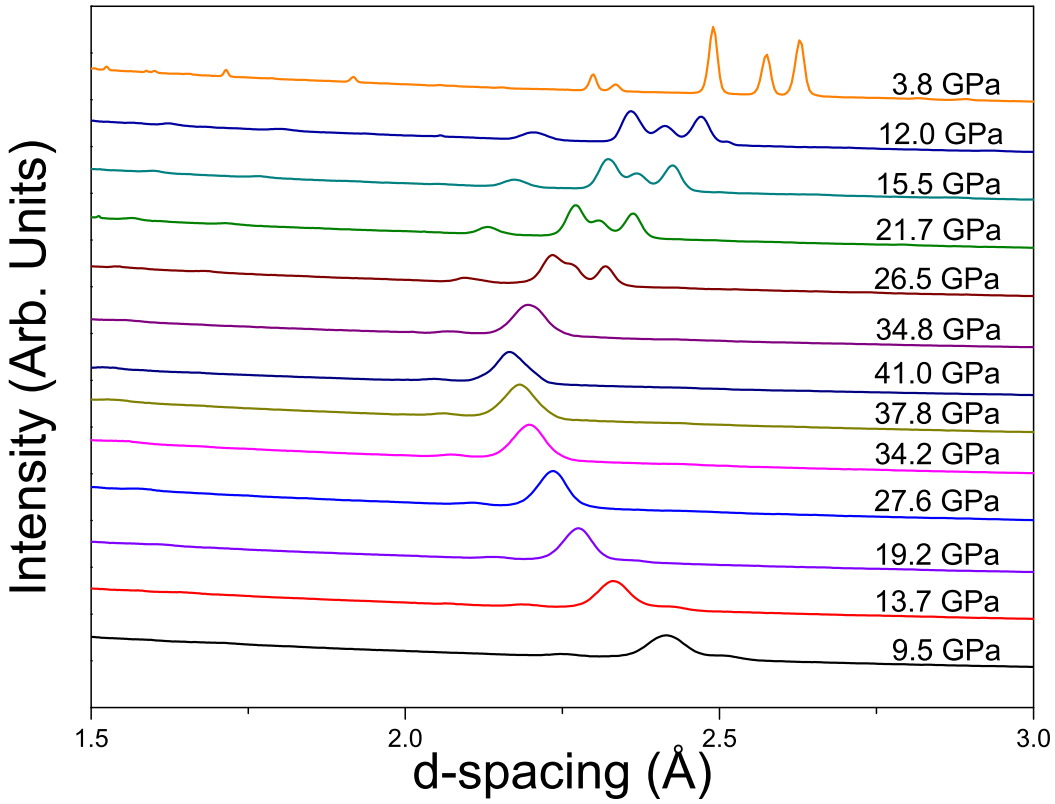

Figure 7.4 *X-ray powder diffraction patterns of the compression and decompression data from the 2:1 sample. The first plot is at the top of the figure, the last plot at the bottom. The liquid patterns recorded at 1.1 GPa at the beginning of the experiment and the 1.3 GPa at the end of the experiment have been omitted. The three most intense peaks of AHH-II can clearly be seen in the early plots before a single bcc peak forms above 26.5 GPa.*

sample much more in line with that observed in the 1:1 and 2:1 x-ray samples with AHH-II existing up to the final measurement of 26.6 GPa. Higher pressures were not pursued in the neutron sample because the load limit of the anvils had been reached [96], yet the transformation to the DMA phase does appear to have started in the highest pressure profile shown in Figure 7.7. Pressures for the neutron sample were calculated from the D_2O equation of state as described previously in Chapter 5 Section 5.2, while the x-ray samples were calculated from ruby fluorescence [129].

The 2:1 sample was the only sample that was studied under decompression. Once the sample had transformed to DMA the pressure was slowly decreased to look for the reverse transition. Surprisingly the DMA phase persisted down to at least 9.5 GPa before re-entering the liquid state (see Figure 7.4). The large pressure

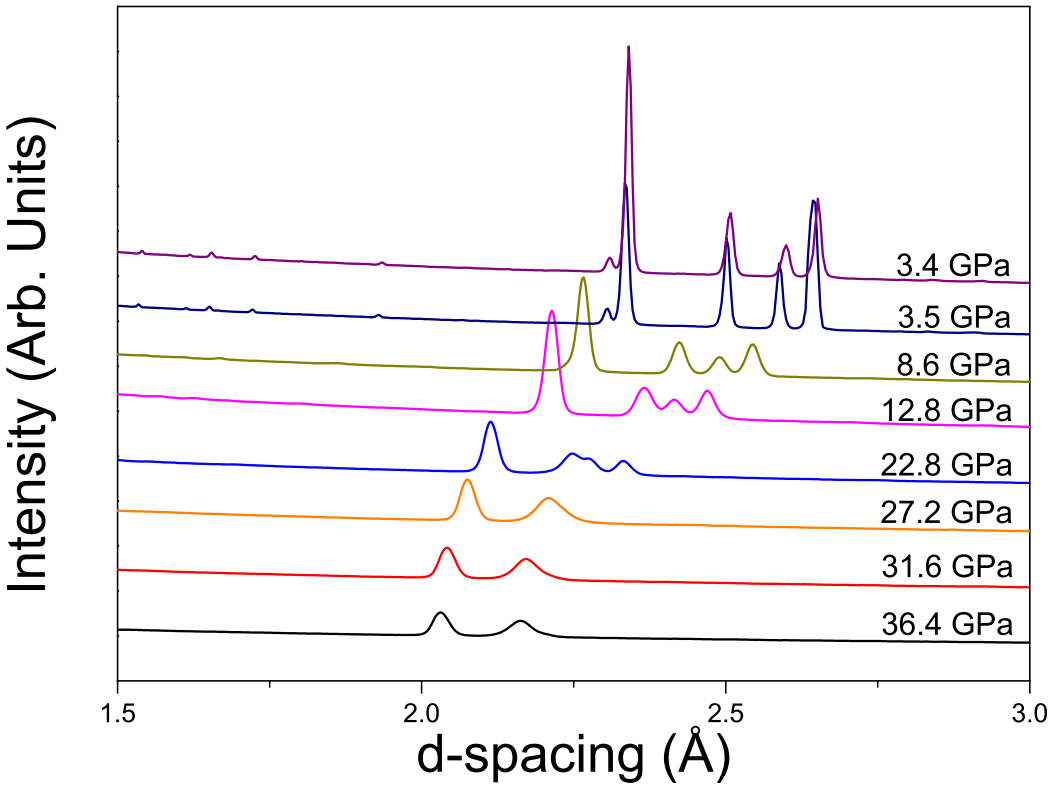

Figure 7.5 *X-ray powder diffraction patterns of the compression data from the 1:1 sample. The first plot is at the top of the figure, the last plot at the bottom. The only difference between the first plots in this figure and Figure 7.4 is the more pronounced ice-VII peak.*

stability range of ∼17 GPa means that this transition is unlikely the be a result of hysteresis alone. Closer inspection of the data recorded at 9.5 GPa (the last data set before entering the liquid) shows a pronounced shoulder on the main peak that may be the start of a transformation back to AHH-II, but this remains speculation. Further work should be performed to see if the DMA phase persists down to the liquid phase or decomposes fully to AHH-II under decompression.

Another observation that can be made from the data is that the second transformation reported by Ma *et al.* is not observed in these samples, and the transition to DMA is seen at a pressure ∼10 GPa higher than that reported by Ma *et al.* [2]. Excluding the loading method, there are two major differences between the experiments conducted here and those conducted by Ma *et al.*

The first is the difference in gasket materials. Ma *et al.* used steel as a gasket material, which has been known to react with heated mixtures of ammonia and water [48, 49]. This means one or both of the transitions observed by Ma *et al.*

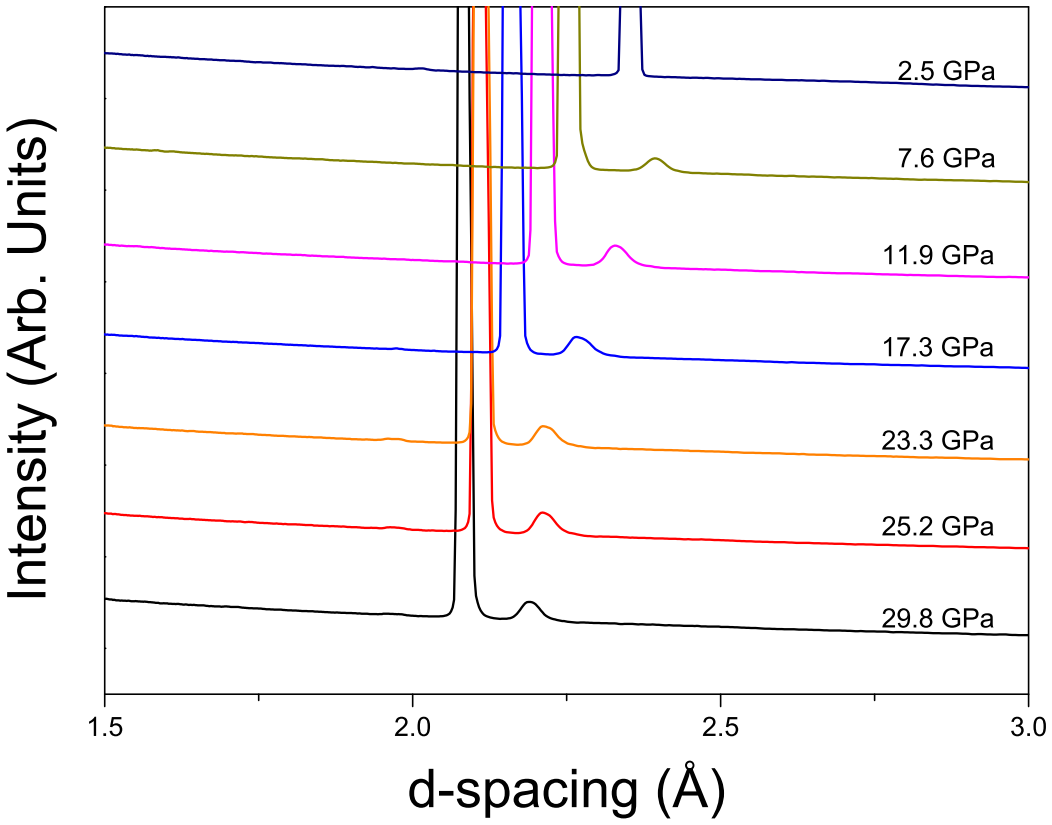

Figure 7.6 *X-ray powder diffraction patterns of the compression data from the 1:2 sample. The first plot is at the top of the figure, the last plot at the bottom. This sample behaved very differently to the two previous samples, the very large peaks is caused by ice-VII, while the much smaller peak has been attributed to AHH DMA. This reason for this different behaviour is thought to be caused by either rapid compression of the sample or the ice-VII acting as a seed crystal (see text).*

could actually be a reaction between the ammonia-water sample and the gasket material. However, since the samples by Ma *et al.* were not heated during their experiments [2], this seems unlikely.

The other major difference is that the samples here were of deuterated ammonia-water samples. Hydrogen and deuterium atoms are known to alter the proton transfer properties of materials. This was explored in several ammonia hydrate samples at low temperatures by Bertie *et al.* [38, 39, 139]. The pressures and temperatures where phase transitions occur are also known to differ between hydrogenous and deuterated samples. This is most pronounced when comparing the phase transitions of pure hydrogen to pure deuterium [140], but this effect has also been observed in ice [141]. It is possible that this is the largest factor

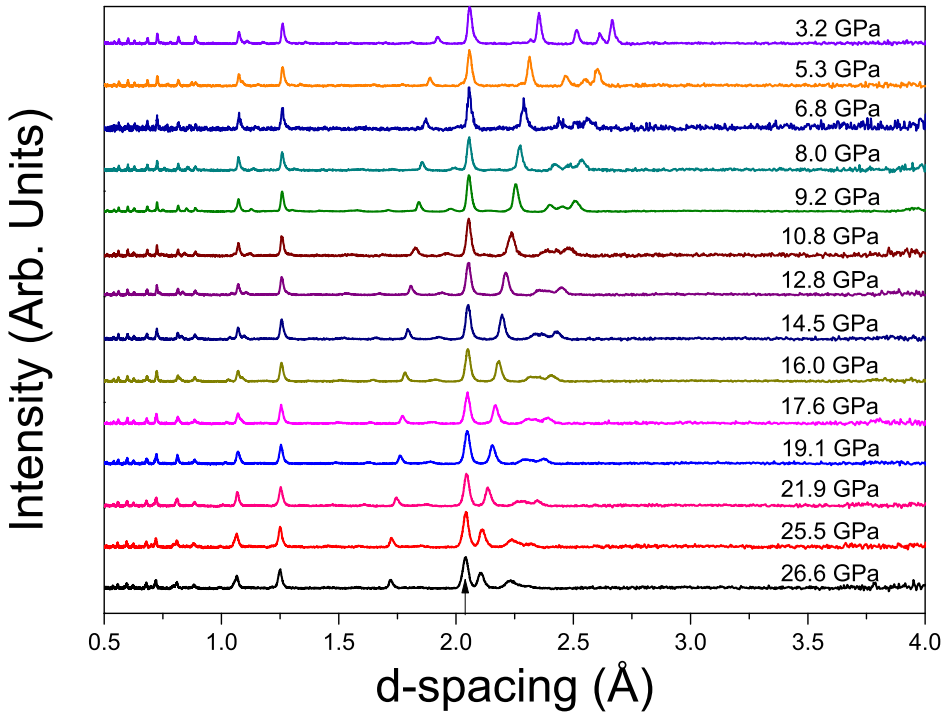

Figure 7.7 *Diffraction patterns of the compression data from a 1:2 neutron powder sample. The first x-ray powder pattern is at the top of the figure, the last plot at the bottom. This 1:2 sample shows behaviour in line with the 1:1 and 2:1 samples. The transition to a single bcc peak could possibly be occurring in the final plot at 26.6 GPa. The arrow indicates the largest peak caused by the diamond anvils. The plots have different amplitude in their diffraction peaks and have been scaled individually so that the diamond peaks are of comparable height, this is why some plots seem noisier than others.*

in the difference between the observed transitions pressures between the work reported here and the work reported by Ma *et al.* [2]. It should be noted that the ∼7 GPa discrepancy in transition pressures reported here is much larger that the difference in transition pressure observed in pure water ice. If the process of transforming to DMA under compression is led by proton transfer between the molecules of AHH-II, and hence retarded by deuteration [142], then this could be an explanation of the differences seen between the data presented here and the data presented by Ma *et al.* However, this could only be confirmed or disproved through further experimentation.

Using the collected data from the experiments presented in this chapter, an equation of state (EOS) for AHH-II can be calculated, by fitting the EOS parameters K_0, K_0' and V_0 as described in Chapter 4 Section 4.3.2. These

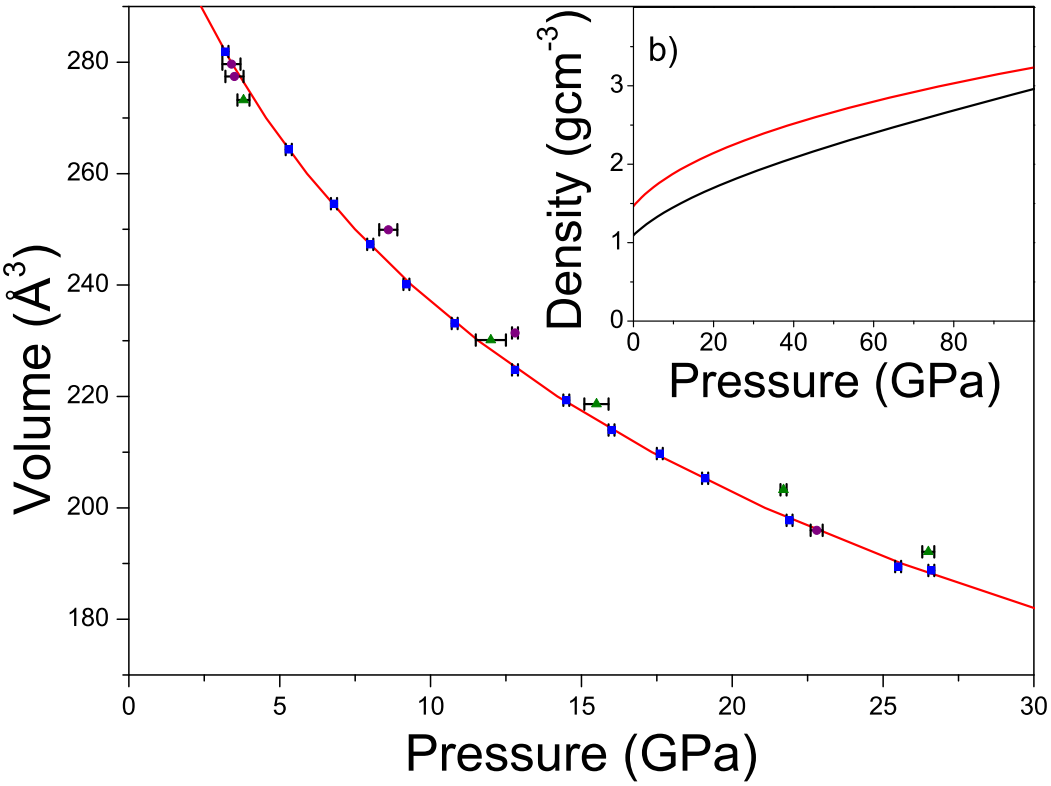

Figure 7.8 *A third-order Birch-Murnaghan fit to the unit cell volume and pressure data of the AHH-II structure seen in all compression experiment samples. The red line is the fit to the neutron 1:2 ammonia-to-water ratio sample, the blue data points. The green data points are from the 2:1 x-ray sample and the purple points are from the 1:1 x-ray sample. The inset shows how the densities of both deuterated ice VII (red line) and AHH-II (black line) over a range of pressures, and clearly shows that AHH-II remains less dense than ice VII.*

parameters were fitted to the neutron powder data of the 1:2 ammonia-to-water ratio sample alone, as this had the most points with the most consistently determined unit cell volumes, as the data had a larger number of diffraction peaks to be fitted against, in contrast to the three peaks from the x-ray data. The parameters were fitted with the EOS fitting program EOSfit [143]. This returned the following EOS parameter values for a third order Birch-Murnaghan fit; $K_0 = 18(2)$ GPa, $K_0' = 3.7(2)$ and $V_0 = 323(4)$ Å^3. This fit is plotted in Figure 7.8, along with the pressure and volume data from the 1:2 neutron sample, and the 1:1 and 2:1 x-ray samples. As the EOS has been determined, the densities of both ice VII and AHH-II can be compared over the pressure range that these two materials exist. This is shown in the inset of Figure 7.8, and clearly shows that AHH-II remains less dense than ice VII up to at least 100 GPa, where both

phases are no longer the stable phases of these materials. This is calculated for the deuterated varieties of both AHH-II and ice VII, but suggests that there could be differentiation within the cores of planets where the pressure-induced dehydration of water rich ammonia hydrates is occurring, leading to a water-rich core.

7.3 High–Temperature High–Pressure Behaviour of Hydrogenous Ammonia Hemihydrate

As stated in the previous section, the AHH-II to DMA transition could, in part, be driven by rotation and proton transfer. This would mean that supplying enough energy to the AHH-II structure, in the form of increased temperature, could promote the transition to the DMA phase. To test this theory another supporting experiment was performed. Merrill-Bassett cells with rhenium gaskets were prepared for a heating experiment to map out the high temperature region of the AHH phase diagram. Rhenium gaskets were used after it was found out on the previous experiment that, when heated, tungsten reacts with the ammonia-water mixture. A 2:1 ammonia-to-water sample was prepared and mounted within an external ring heater, which heats the entire cell assembly as well as the sample. Figures 7.9 and 7.10 show waterfall plots of data taken upon increasing temperature and the associated pressure increase. These data were taken on the same sample at two different initial pressures and show some recurring features that occur when the sample is heated. Figure 7.9 is of the first heating cycle performed on the sample. Upon solidification a mixed solid of AHH-II and DMA was achieved but after heating the AHH-II also transformed into DMA. Surprisingly at a pressure and temperature of 4.81(2) GPa and 95°C the highest intensity peak of DMA vanishes while some of the weaker diffraction peaks remain, the location of the weak peaks in question are marked with the arrow in Figure 7.9. The sample was highly textured, as the intensities of the three highest intensity AHH peaks show (comparing all the x-ray data sets shown in this chapter, the relative intensities of these peaks are very different), and while this could mean the disappearance of the main peak is caused by texture effects as this happens consistently over both runs this seems unlikely. Unfortunately, the first time the strongest DMA peak disappeared this was mis-interpreted as melting through the entire sample, and the sample pressurized to re-enter the solid phase. The result of this was to produce AHH-II again, which can be seen

at 5.90(2) GPa and 95°C, however the peak shapes are fairly irregular. upon heating this again transforms into DMA, and again before melting the strongest peak disappears. Melting was eventually observed at 5.71(2) GPa and 205°C.

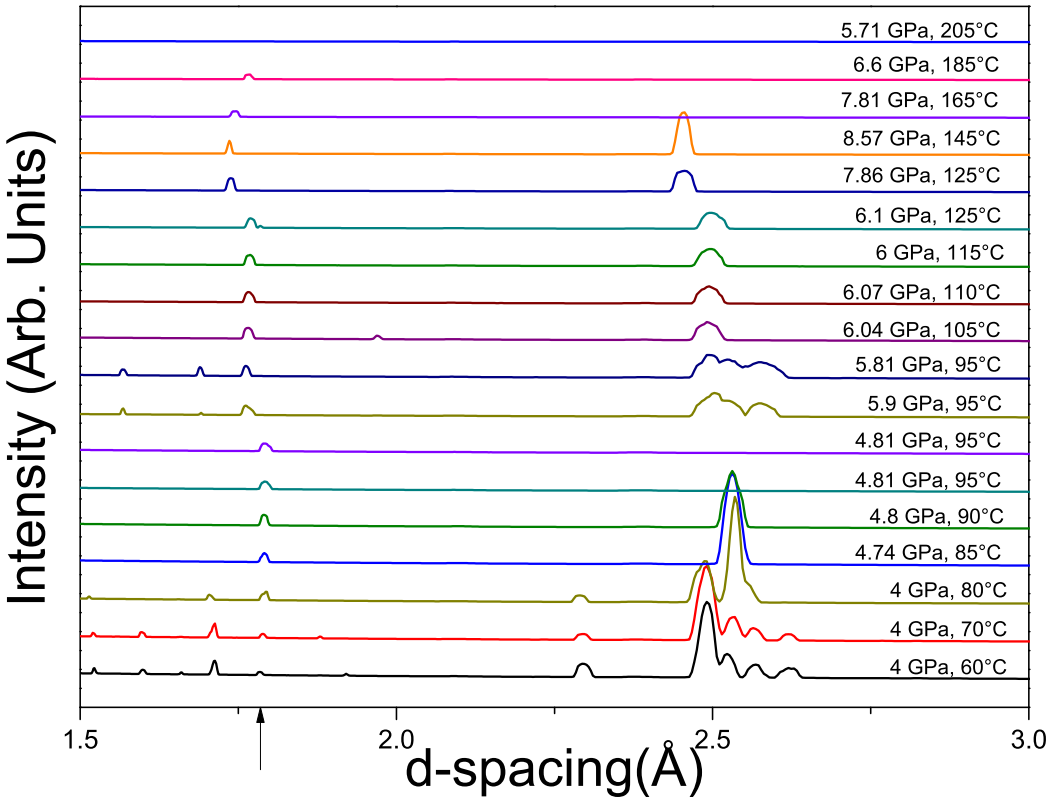

Figure 7.9 *X-ray powder diffraction patterns taken from the first heating cycle on the hydrogenous 2:1 ammonia-to-water ratio sample. The pressure, measured by the ruby fluorescence method, and the temperature, recorded by a thermocouple placed on the back of the diamond, associated with each of the plots are shown above the data on the left. The arrow shows the weak peaks present in most of the plots, even when the strongest peak of DMA has disappeared.*

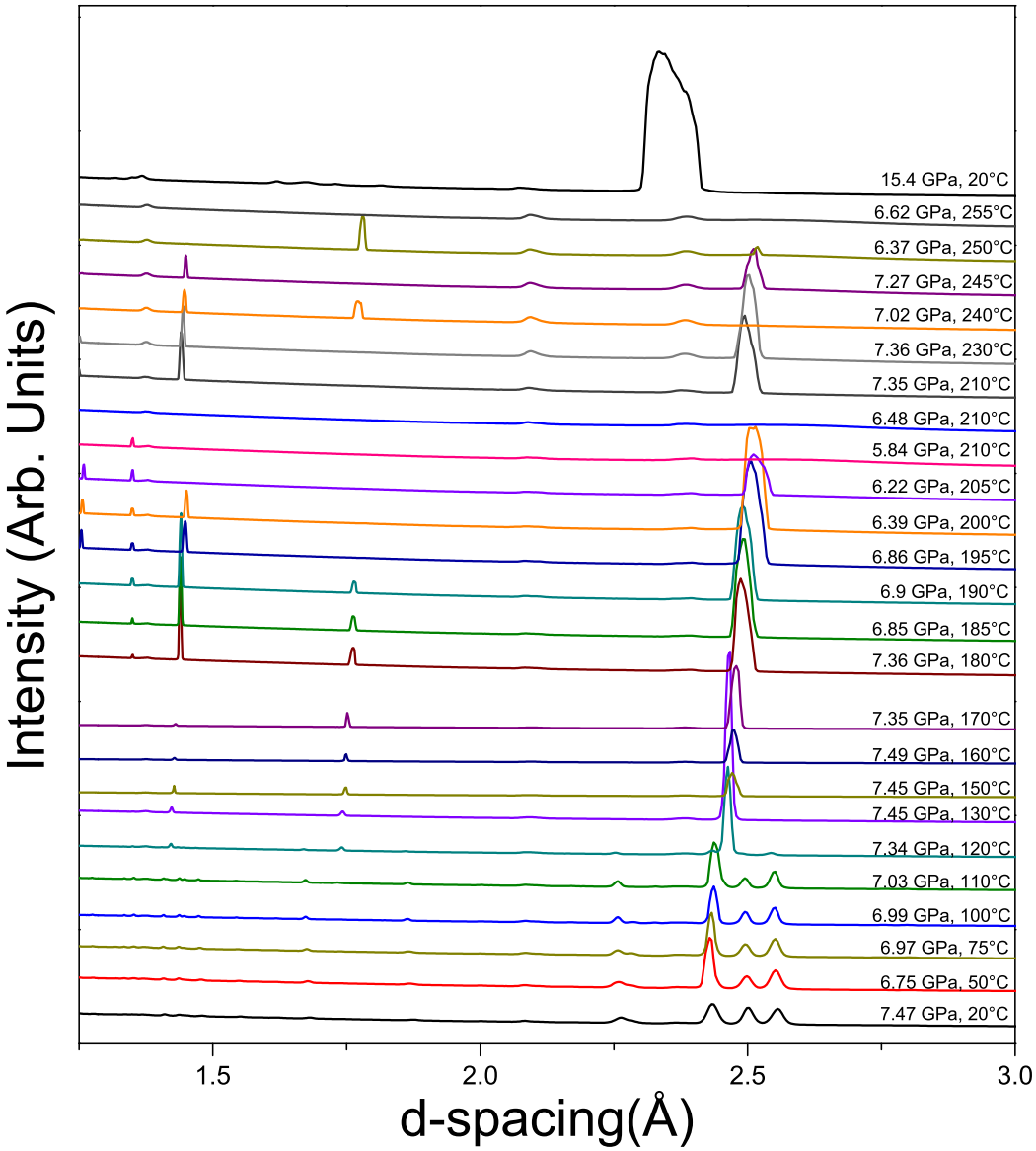

Figure 7.10 *X-ray powder diffraction patterns taken from the second heating cycle on the hydrogenous 2:1 ammonia-to-water ratio sample. The pressure, measured by the ruby fluorescence method, and the temperature, recorded by a thermocouple placed on the back of the diamond, associated with each of the plots are shown above the data on the left.*

The sample was left overnight to cool back down to room temperature and increased in pressure slightly to obtain a series of pressure points at higher pressures. As can be seen in Figure 7.10 the sample crystallised totally in the AHH-II phase. again upon heating a clear transition to DMA is seen at 7.34(2) GPa and 120°C. Again the disappearance of the most intense DMA peak was observed consistently before the onset of melting, and this seems to be a

feature of the kinetics of the melting transition rather than a texture effect. Comparing Figure 7.9 and 7.10 we can see that the overall pressure increase involved with increasing temperature is reduced from ∼0.8 GPa over 35°C from the first temperature cycle to just ∼0.3 GPa over a 50°C increase. We can also see that the pressure drop when approaching the melting transition is less pronounced so this feature may be related to the melt line tracking phenomena. Increasing pressure once the sample had melted caused the sample to re-enter the DMA phase and further heating melted it, once again showing the signature of the most intense peak disappearing before the smaller features prior to melting. finally upon cooling back down to room temperature the sample showed a significant pressure increase to 15.4(2) GPa at room temperature.

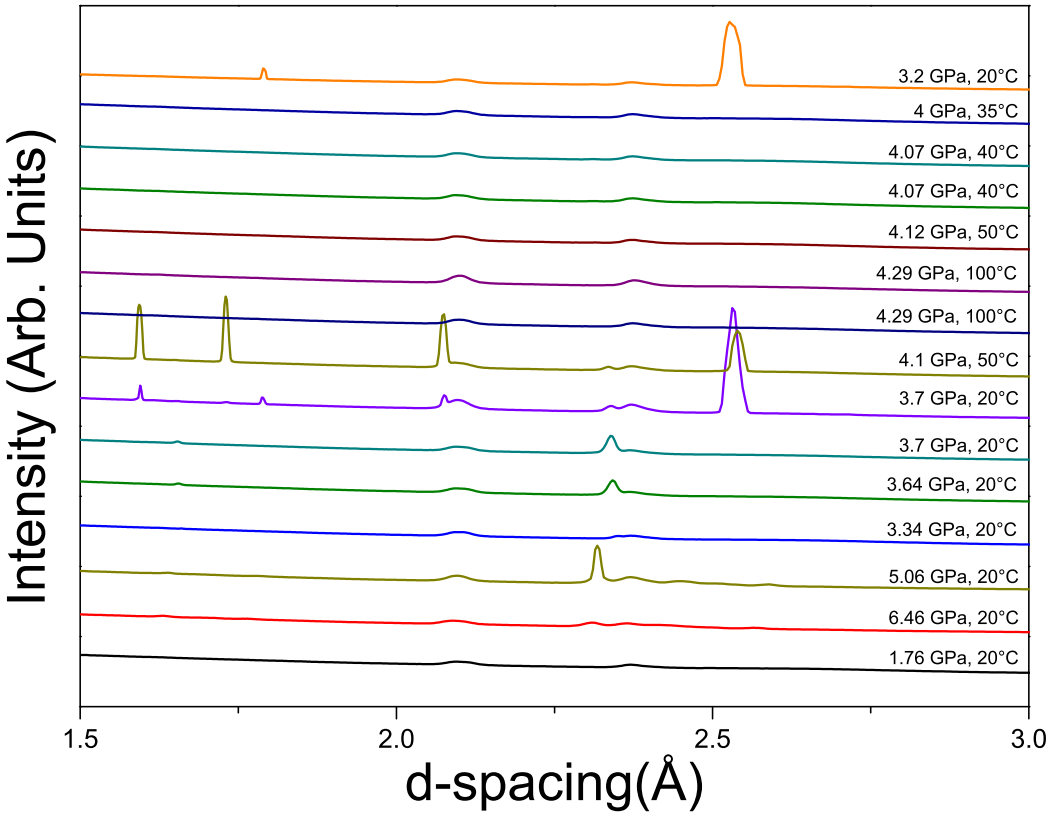

Figure 7.11 *X-ray powder diffraction patterns taken from the heating cycle on the hydrogenous 1:1 ammonia-to-water ratio sample. The pressure, measured by the ruby fluorescence method, and the temperature, recorded by a thermocouple placed on the back of the diamond, associated with the plots are shown above the data on the left.*

A separate sample was prepared with a 1:1 composition of ammonia-to-water. This sample was also compressed until it became solid as a mixture of AHH and ice VII before being heated like the samples mentioned in the previous paragraphs.

The 2-D integrations of this sample are shown in Figure 7.11. The first few plots show odd behaviour where the sample refused to solidify fully, even at high pressures. This behaviour eventually lead to the formation of only ice VII with the rest of the sample remaining liquid. This situation was remedied by lowering the pressure until the sample became totally liquid again and then re-pressurising slightly and tapping the cell, but it formed into DMA straight away instead of AHH-II. This may have been caused by the presence of ice VII which could have acted as a seed crystal for the remaining sample, because of the very similar structures of ice VII and DMA (see Chapter 5 Section 5.3). Upon heating and entering the temperature required to melt DMA it can easily be seen that both the DMA and ice VII signal disappear and the sample is fully liquid again. After the sample cooled down only peaks corresponding to DMA can be seen. This would suggest that the excess water has been incorporated into the DMA structure rather than separating out again into ice VII. This would suggest that water ice can be incorporated into the DMA structure from the melt, at high pressure, but whether this is only the case because of the 1:1 composition or whether this would be a viable P-T path to try and make non-stoichiometric DMA remains to be determined.

The 1:1 experiment mentioned above was not a typical sample of DMA; its odd behaviour has already been noted above. While this sample did behave atypically, with the refusal to first solidify, and then by forming to DMA immediately, the sample was also a very poor powdered sample. This could easily be determined from the textured powder pattern seen on the area detector, and can also be seen in Figure 7.11 by the appearance and disappearance of diffraction peaks, and changes to peak intensity without any melting taking place.

All the pressure and temperature data gathered from this experiment have been collated into the P-T phase diagram in Figure 7.12. The lines on the diagram are meant as guides to the eye only, and are not meant to represent the actual phase boundaries in the system. The lower line of the AHH-II stability region has been taken from the dehydration lines present in both ADH and AMH phase diagrams where both substances are known to separate into AHH-II and ice VII. In addition to this data, the transformation to DMA at high pressures at room temperature would suggest that there must exist a turn over in the AHH-II/DMA transition line.

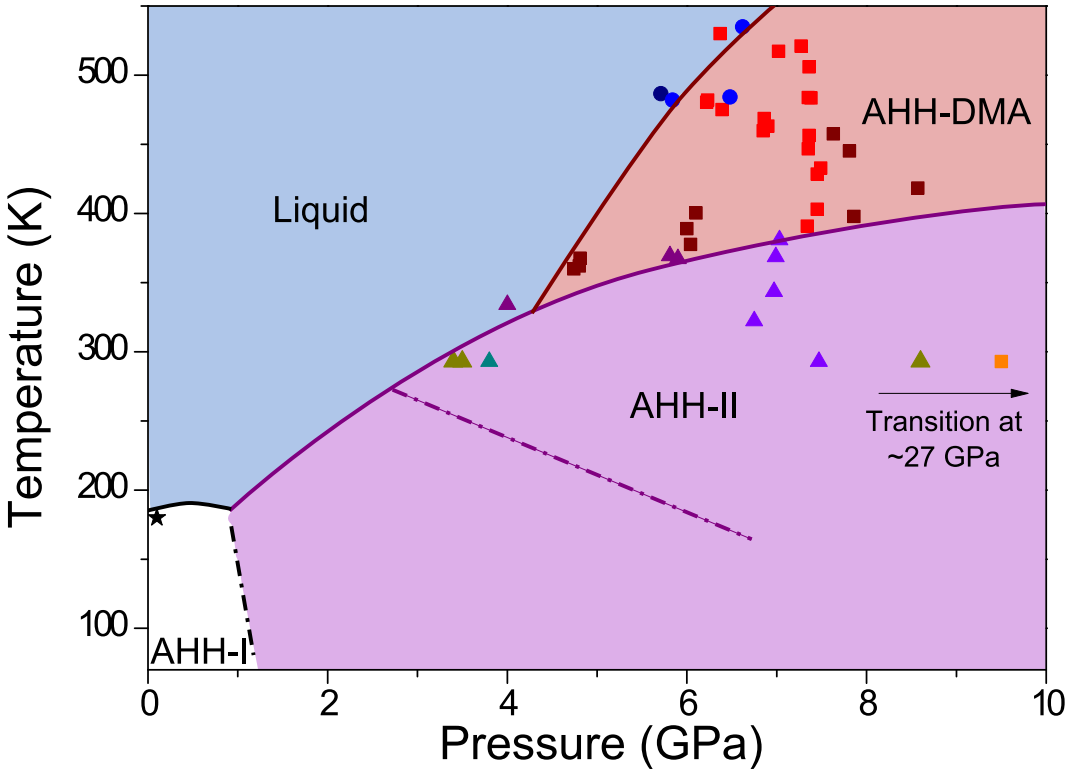

Figure 7.12 *The phase diagram of ammonia hemihydrate. The lines are guides to the eye, and are not derived from data. The Purple triangles represent points where samples were observed to be AHH-II. The red squares represent points where the sample transformed into DMA. The lighter shades are from the second heating cycle described in the text. The yellow and turquoise triangles represent AHH-II formed in the compression samples described in section 7.2. The orange square is DMA from decompression of the 2:1 sample in section 7.2. The black star is AHH-I as reported by Loveday and Nelmes [43]. The two dash-dot lines denote the area that forms unknown phases of AHH seen in the neutron powder experiments in section 7.1*

7.4 Concluding Remarks

In this chapter it has been shown that ammonia hemihydrate does indeed transform into DMA upon increase of pressure alone, but does not form DMA following the same pressure-temperature paths required for both AMH and ADH to form into DMA phases. As there is a significant difference between the transition pressure between hydrogenous and deuterated samples upon compression, the transition may be led by proton transfer between the ammonia

and water molecules. This proton exchange would be analogous to the short lived ionic pair production that occurs before the onset of the superionic phase in ammonia [6], accompanied by rotation of the remainder of the molecule. While this proton transfer process would occur at temperatures much lower than what is seen in either pure ammonia [6] or pure water ice [11], AMH is thought to have a low temperature transition to an ionic solid [58], it remains a possibility, but will need to be confirmed with further experimentation.

The transition to the DMA phase was seen to be consistent between samples of 2:1 and 1:1 and 1:2 ammonia-to-water ratio deuterated samples, however it was also observed in a single 1:2 sample that the DMA phase could be reached through rapid compression of the sample. The DMA phase formed in this fashion can then be recovered to much lower pressures than it takes to form it, down to as low as 9.50(2) GPa at least. It has also been shown that AHH DMA can be reached through heating a 2:1 hydrogenous sample and the DMA phase then subsequently melts at higher temperatures. It has also been noted that the transition to liquid is preceded by an apparent disappearance of the strongest diffraction peak of DMA and that it is possible to transform back into AHH-II from DMA at 5.90(2) GPa and 95°C.

Both of these conclusions would mean that there should be a maximum in the transition line between AHH-II and DMA at some point in the phase diagram. It has also been observed that a completely melted 1:1 sample appeared to form only DMA upon cooling to room temperature, however the sample did not behave like other observed samples, so no firm conclusion on this fact can be drawn. However, if this result is confirmed it opens the possibility of attempting to make off stoichiometry ammonia hydrates with the DMA structure.

Chapter 8

Conclusions

The aim of this thesis has been to investigate the ammonia hydrate systems, as they are important for modelling the interiors of icy satellites such as Titan, and the ice giants Uranus and Neptune. Further to this, as mixed hydrogen bonds are known to be important for biological processes and the bonding of DNA (see Chapter 1 Section 1.7), a simple material that exists over a large pressure range is required to study the evolution of these mixed hydrogen bonds before the larger and more complicated systems of DNA can be studied in detail. In this chapter the results that have been presented in chapters 5, 6 and 7 will be reiterated and discussed as a whole and the implications that these results have will also be discussed. Finally, future work that would either build upon or complement the work presented in this thesis will be discussed.

8.1 Summary of Results From Previous Chapters

X-ray and neutron diffraction studies provide a number of complementary techniques that complement the data that each provide. In chapter 5 a combination of x-ray single-crystal and neutron powder diffraction data was used to solve the crystal structure of ammonia hemihydrate phase II, which before this work was incorrectly thought to be a phase of ammonia monohydrate, AMH-V. The AHH-II structure has a monoclinic unit cell with lattice parameters $a = 3.3584(5)$ Å, $b = 9.215(1)$ Å, $c = 8.933(1)$ Å and $\beta = 94.331(8)^\circ$ with a space group of $P2_1/c$ at room temperature and a pressure of 3.5(1) GPa. This structure

has a similar molecular packing of molecules as ice-VII, but with a very different bonding system. This also means that AHH-II has a very similar molecular packing as the disordered molecular alloy phase which is seen in the other two stable ammonia hydrates, ammonia monohydrate and ammonia dihydrate.

In chapter 6 a 2:1 ammonia-to-water crystal of AHH-II was grown for both x-ray and single crystal study, but unfortunately it did not appear to form from the 2:1 liquid. Instead another phase appeared and was characterised by x-ray diffraction to have a monoclinic unit cell with lattice parameters $a = 6.319(3)$ Å, $b = 5.322(2)$ Å, $c = 6.456(2)$ Å and $\beta = 113.41(2)^\circ$ at room temperature and a pressure of 2.7(4)GPa. While this unit cell did provide a unit cell that allowed the single-crystal prepared for neutron diffraction study to be probed successfully at the ILL, an inconsistent background prevented further data analysis on this phase. Instead data was collected at the SXD instrument at ISIS, but the structure could not be identified through all of the peaks registered on the SXD detectors. To address this a program was written to identify if any of these peaks were due to multiple scattering effects, where the neutron beam could diffract off of one diamond followed by the other, creating reflections in the detectors which were not caused by either the sample or the two diamond anvils, which could be confused with sample reflections. While the program appeared to work, the collection of reflections which were left after removing the potential multiple scattering reflections still did not show an obvious lattice grid, so the structure remained unsolved.

Finally in chapter 7 in a series of high-pressure and high-temperature experiments it was determined that AHH-II will transform into the DMA phase and can be recovered to much lower pressures than it takes to form it, down to at least 9.5(2) GPa. The most likely reason for the disagreement with the AHH-II/DMA transition observed by Ma *et al.* [2] was identified to be the deuteration of the samples presented, which may be the reason for preventing the transition from occurring at lower pressures and may have prevented the second transition from happening at the pressures explored. It has also been show that the DMA phase of AHH can be formed by heating AHH-II samples, and this transition is reversible. An experiment was also conducted to determine whether a 1:1 ammonia-to-water sample could be totally melted and formed into AMH DMA from this melt, if this were possible it could mean that off-stoichiometry DMA phases could form, and a solid solution between ammonia and water may exist. However, the data collected on the 1:1 ammonia-to-water ratio sample was poor quality, as described

in Chapter 7 Section 7.3, and further experiments will be needed to confirm the conclusion suggested here.

8.2 Implications of Results on the Ammonia-Water Systems

From the work presented in this thesis it has been shown that the phases of ammonia hemihydrate have a more important role in describing the geological processes within icy planets and moons than previously expected. This is all due to AHH being the stable ammonia hydrate at high pressure as a result of the pressure induced dehydration process. Previously this was thought to only result in ammonia monohydrate from ammonia dihydrate. In addition to this the transition to a disordered molecular alloy phase upon either an increase of pressure or increase of temperature brings AHH into line with the other two stoichiometries, raising the possibility that there is a solid solution between AHH, AMH and ADH. If a solid solution does indeed occur between the three stoichiometric ammonia hydrates, then the dehydration region seen in the phase diagram of ADH (Figure 1.7) appears out of place. A solid solution implies that ammonia and water become interchangeable at high pressures and temperatures, while the dehydration boundary would suggest the opposite. These conclusions seem incompatible, and since the dehydration boundary has already been observed and non-stoichiometric ammonia hydrates have yet to be observed, an ammonia-water solid solution seems unlikely.

The conclusion that AHH-II remains less dense than ice VII over the pressure ranges that might be expected within icy satellites such as Titan or Europa means that there could be significant separation of an ammonia rich subsurface ocean with a water rich deep interior, which is of significant importance as this ice could then be free to form other hydrates such as methane hydrate, which is thought to be responsible for replenishing the methane observed in Titan's atmosphere [144]. However, as AHH-II transforms into a DMA phase at high temperatures, this stratification will be unlikely to occur in the ice giants Uranus and Neptune, as the pressures and temperatures within their interiors is far greater than that of icy satellites such as Titan [16].

Finally, the large pressure range that AHH-II exists over, $\sim$16 GPa for

hydrogenous samples and ∼22 GPa for deuterated samples, makes this material a good candidate for observing the evolution of mixed hydrogen bonds under increasing pressure conditions to build the fundamental knowledge required to study the operation of more complicated systems under these conditions, such as DNA.

8.3 Future Work

An interesting property of the ammonia hydrates, especially the hydrates with a large ammonia content (1:1 ammonia-to-water ratio and above) that has not currently been explained in the literature, is that these hydrates have a very large liquid region of the phase diagram. comparing the phase diagram of AHH (Figure 7.12) to the phase diagrams of both ammonia and ice (Figures 1.2 and 1.4 respectively) is that both ammonia and water solidify at ∼1 GPa while in AHH solidification does not occur until ∼3 GPa. While it is well known that inclusion of other substances such as salt in water can delay solidification, to have this delayed well beyond the point where both individual substances would have solidified is unusual. In the water rich ammonia-water solutions water tends to freeze out at ∼2 GPa, it seems reasonable to expect a similar behaviour of ammonia rich solutions, which so far has not been seen.

The existence of a DMA phase in all three stoichiometric ammonia hydrates opens the possibility of hydrates of arbitrary ammonia-to-water ratio being able to form into a DMA phase, and hence a solid solution between the ammonia hydrates existing. This poses another interesting question, as the end points of this ammonia and water complex, ice VII and ammonia-IV, do not form cubic phases like that seen in DMA. While ice VII does have molecular packing similar to that seen in DMA, the bonding between the molecules is very different, ammonia-IV bears very little resemblance to a cubic structure, having space group $P2_12_12_1$, so it is difficult to determine what ammonia-to-water ratio the solid solution, if it exists, should continue to. Determining whether there is a solid solution at high pressures and temperatures would be of greatest interests in modelling the interiors of the ice giants Uranus and Neptune, as these planets have the interior pressures and temperatures that can form at least AHH DMA [16], and the interaction between ammonia and water in this could have a direct impact on the dynamics of their interiors.

The interiors of icy satellites such as Titan are not only composed of ammonia and water, there is also a significant amount of other materials such as methane which could alter the behaviour of the dynamics of the interior. While much has been done towards the study of the methane hydrates, the ternary system (ammonia-water-methane) needs to be studied in more detail to accurately determine the behaviour of the interior. Additionally, just as the study of the binary systems of ammonia-water and methane-water are required to start studying the ternary system, the study of the other binary, methane-ammonia mixtures, will be required before studying the ternary system.

The ammonia-water system remains a complicated and interesting binary system with many interesting properties left to explore. This unexplained complexity highlights that a theoretical model of mixed hydrogen bonded systems would be very useful, not only to explain what is observed experimentally, but also to give predictions as to what will occur under conditions that are currently unreachable experimentally. This would help give a complete picture of the underlying physics dictating what has already been observed in this system.

These are just some of the most obvious avenues that can expand upon the work presented here. While the work presented here has furthered the understanding of the ammonia-water system, there still remains much that is unexplained, some of which have already been highlighted in this chapter. To conclude, the ammonia-water system still shows great complexity and requires greater study before it can be fully understood.

Bibliography

[1] C. W. Wilson, C. L. Bull, G. Stinton, and J. S. Loveday, J. Chem. Phys. **136**, 094506 (2012), ISSN 1089-7690, URL http://www.ncbi.nlm.nih.gov/pubmed/22401451.

[2] C. Ma, F. Li, Q. Zhou, F. Huang, J. Wang, M. Zhang, Z. Wang, and Q. Cui, Roy. Soc. Chem. Adv. **2**, 4920 (2012), ISSN 2046-2069, URL http://xlink.rsc.org/?DOI=c2ra01156e.

[3] G. A. Jeffrey, *An Introduction to Hydrogen Bonding* (Oxford University Press, 1997), chap. 2.

[4] V. Smil, *Enriching the Earth: Fritz Haber, Carl Bosch, and the Transformation of World Food Production* (MIT Press, 2001).

[5] D. D. Nelson, G. T. Fraser, and W. Klemperer, Science **238**, 1670 (1987), ISSN 0036-8075, URL http://www.ncbi.nlm.nih.gov/pubmed/17737668.

[6] S. Ninet, F. Datchi, and A. M. Saitta, Phys. Rev. Lett. **108**, 165702 (2012), ISSN 0031-9007, URL http://link.aps.org/doi/10.1103/PhysRevLett.108.165702.

[7] J. Loveday, R. Nelmes, W. Marshall, J. Besson, S. Klotz, and G. Hamel, Phys. Rev. Lett. **76**, 74 (1996), ISSN 0031-9007, URL http://link.aps.org/doi/10.1103/PhysRevLett.76.74.

[8] J. W. Reed and P. M. Harris, J. Chem. Phys. **35**, 1730 (1961), ISSN 00219606, URL http://link.aip.org/link/JCPSA6/v35/i5/p1730/s1&Agg=doi.

[9] S. Ninet, F. Datchi, S. Klotz, G. Hamel, J. Loveday, and R. Nelmes, Phys. Rev. B **79**, 100101 (2009), ISSN 1098-0121, URL http://link.aps.org/doi/10.1103/PhysRevB.79.100101.

[10] G. A. Jeffrey, *An Introduction to Hydrogen Bonding* (Oxford University Press, 1997), chap. 8.

[11] A. Goncharov, N. Goldman, L. Fried, J. Crowhurst, I.-F. Kuo, C. Mundy, and J. Zaug, Phys. Rev. Lett. **94**, 125508 (2005), ISSN 0031-9007, URL http://link.aps.org/doi/10.1103/PhysRevLett.94.125508.

[12] P. Pruzan, J. C. Chervin, E. Wolanin, B. Canny, M. Gauthier, and M. Hanfland, J. Raman Spectrosc. **34**, 591 (2003), ISSN 0377-0486, URL http://doi.wiley.com/10.1002/jrs.1039.

[13] R. J. Nelmes, J. S. Loveday, R. M. Wilson, J. M. Besson, P. Pruzan, S. Klotz, G. Hamel, and S. Hull, Phys. Rev. Lett. **71**, 1192 (1993), URL http://prl.aps.org/abstract/PRL/v71/i8/p1192_1.

[14] C. Lobban, J. L. Finney, and W. F. Kuhs, Nature **391**, 268 (1998), URL http://www.nature.com/nature/journal/v391/n6664/abs/391268a0.html.

[15] H. Lammer, J. H. Bredehöft, a. Coustenis, M. L. Khodachenko, L. Kaltenegger, O. Grasset, D. Prieur, F. Raulin, P. Ehrenfreund, M. Yamauchi, et al., Ast. Astrophys. Rev. **17**, 181 (2009), ISSN 0935-4956, URL http://link.springer.com/10.1007/s00159-009-0019-z.

[16] T. Guillot, Annu. Rev. Earth Planet. Sci. **33**, 493 (2005), ISSN 0084-6597, URL http://www.annualreviews.org/doi/abs/10.1146/annurev.earth.32.101802.120325.

[17] G. Tobie, O. Grasset, J. I. Lunine, A. Mocquet, and C. Sotin, Icarus **175**, 496 (2005), ISSN 00191035, URL http://linkinghub.elsevier.com/retrieve/pii/S0019103504004269.

[18] R. Lorenz and J. Mitton, *Lifting Titan's veil : exploring the giant moon of Saturn* (Cambridge University Press, 2008), chap. 3, ISBN 0-03-083993-9.

[19] A. Coustenis, *Titan : exploring an the earthlike world* (World Scientific, 2008), chap. 10, ISBN 0-03-083993-9.

[20] R. Lorenz and J. Mitton, *Lifting Titan's veil : exploring the giant moon of Saturn* (Cambridge University Press, 2008), chap. 4, ISBN 0-03-083993-9.

[21] G. Tobie, J. I. Lunine, and C. Sotin, Nature **440**, 61 (2006), ISSN 1476-4687, URL http://www.ncbi.nlm.nih.gov/pubmed/16511489.

[22] A. Coustenis, *Titan : exploring an the earthlike world* (World Scientific, 2008), chap. 6, ISBN 0-03-083993-9.

[23] R. Helled, J. D. Anderson, M. Podolak, and G. Schubert, Astrophys. J. **726**, 15 (2011), ISSN 0004-637X, URL http://stacks.iop.org/0004-637X/726/i=1/a=15?key=crossref.14359b88f748d478e8bdea9e6bc16527.

[24] R. Holme and J. Bloxham, J. Geophys. Res. **101**, 2177 (1996), ISSN 0148-0227, URL http://doi.wiley.com/10.1029/95JE03437.

[25] S. Stanley and J. Bloxham, Nature **428**, 151 (2004), ISSN 1476-4687, URL http://www.ncbi.nlm.nih.gov/pubmed/15014493.

[26] G. Jeffrey, J. Mol. Struct. **322**, 21 (1994), ISSN 0022-2860, URL http://cat.inist.fr/?aModele=afficheN&cpsidt=4197571.

[27] G. A. Jeffrey, *An Introduction to Hydrogen Bonding* (Oxford University Press, 1997), chap. 10.

[28] A. Sharma, J. H. Scott, G. D. Cody, M. L. Fogel, R. M. Hazen, R. J. Hemley, and W. T. Huntress, Science **295**, 1514 (2002), URL http://www.sciencemag.org/content/295/5559/1514.short.

[29] I. Clifford and E. Hunter, J. Chem. Phys. **37**, 101 (1933).

[30] F. F. Rupert, J. Am. Chem. Soc. **31**, 866 (1909), URL http://pubs.acs.org/doi/abs/10.1021/ja01938a002.

[31] F. F. Rupert, J. Am. Chem. Soc. **32**, 748 (1910), URL http://pubs.acs.org/doi/pdf/10.1021/ja01924a004.

[32] S. Postma, Recl. Trav. Chim. Pay B. **39**, 515 (1920).

[33] L. D. Elliott, J. Chem. Phys. **28**, 887 (1924).

[34] A. P. Rollet and G. Vuillard, C. R. Hebdom. Seances Acad. Sci. **243**, 383 (1956).

[35] I. Olovsson and D. H. Templeton, Acta Crystallogr. **12**, 827 (1959), ISSN 0365110X, URL http://scripts.iucr.org/cgi-bin/paper?S0365110X59002419.

[36] W. J. Siemons and D. H. Templeton, Acta Crystallogr. **7**, 194 (1954), ISSN 0365-110X, URL http://scripts.iucr.org/cgi-bin/paper?S0365110X54000539.

[37] J. E. Bertie, M. M. Morrison, J. E. Bertie, and M. M. Morrison, J. Chem. Phys. **73**, 4832 (1980).

[38] J. E. Bertie, J. Chem. Phys. **74**, 4361 (1981), ISSN 00219606, URL http://link.aip.org/link/?JCP/74/4361/1&Agg=doi.

[39] J. E. Bertie, J. Chem. Phys. **78**, 6203 (1983), ISSN 00219606, URL http://link.aip.org/link/?JCP/78/6203/1&Agg=doi.

[40] J. E. Bertie and J. P. Devlin, J. Chem. Phys. **81**, 1559 (1984), ISSN 00219606, URL http://link.aip.org/link/JCPSA6/v81/i4/p1559/s1&Agg=doi.

[41] J. E. Bertie and M. R. Shehata, J. Chem. Phys. **81**, 27 (1984).

[42] J. S. Loveday and R. J. Nelmes, Proc. XVII AIRAPT Conf., Sci. Tech. High Press. **1**, 133 (2000).

[43] J. S. Loveday and R. J. Nelmes, High Press. Res. **24**, 45 (2004), ISSN 0895-7959, URL http://www.tandfonline.com/doi/abs/10.1080/08957950410001661990.

[44] A. D. Fortes, I. G. Wood, J. P. Brodholt, M. Alfredsson, L. Vocadlo, G. S. McGrady, and K. S. Knight, J. Chem. Phys. **119**, 10806 (2003), ISSN 00219606, URL http://link.aip.org/link/JCPSA6/v119/i20/p10806/s1&Agg=doi.

[45] A. D. Fortes, Icarus **162**, 59 (2003), ISSN 00191035, URL http://linkinghub.elsevier.com/retrieve/pii/S0019103502000738.

[46] M. L. Johnson and M. Nicol, Trans. Am. Geophys. U. **66**, 944 (1985).

[47] M. L. Johnson and M. Nicol, J. Geophys. Res. **92**, 6339 (1987), ISSN 0148-0227, URL http://doi.wiley.com/10.1029/JB092iB07p06339.

[48] H. C. Cynn, S. Boone, A. Koumvakalis, M. Nicol, and D. J. Stevenson, Proc. 19th Lun. Planet. Sci. Conf. **1**, 433 (1989).

[49] S. Boone and M. F. Nicol, Proc. 21st Lun. Planet. Sci. Conf. **1**, 603 (1991).

[50] D. Hogenboom, Icarus **128**, 171 (1997), ISSN 00191035, URL http://linkinghub.elsevier.com/retrieve/doi/10.1006/icar.1997.5705.

[51] J. S. Loveday and R. J. Nelmes, Phys. Rev. Lett. **83**, 4329 (1999), ISSN 0031-9007, URL http://link.aps.org/doi/10.1103/PhysRevLett.83.4329.

[52] A. D. Fortes and E. Suard, J. Am. Chem. Soc. **135**, 13508 (2009), URL http://pubs.acs.org/doi/abs/10.1021/ja9052569.

[53] A. Le Bail, Powder Diff. **20**, 316 (2005).

[54] C. J. Pickard and R. J. Needs, J. Phys., Cond. Matt. **23**, 053201 (2011), ISSN 0953-8984, URL http://www.ncbi.nlm.nih.gov/pubmed/21406903.

[55] A. D. Fortes, J. P. Brodholt, I. G. Wood, L. Vocadlo, and H. D. B. Jenkins, J. Chem. Phys. **115**, 7006 (2001), ISSN 00219606, URL http://link.aip.org/link/JCPSA6/v115/i15/p7006/s1&Agg=doi.

[56] R. J. Nelmes, Tech. Rep., ISIS (2000).

[57] A. D. Fortes, E. Suard, M.-H. Lemée-Cailleau, C. J. Pickard, and R. J. Needs, J. Chem. Phys. **131**, 154503 (2009), ISSN 1089-7690, URL http://www.ncbi.nlm.nih.gov/pubmed/20568868.

[58] G. I. G. Griffiths, A. J. Misquitta, a. D. Fortes, C. J. Pickard, and R. J. Needs, J. Chem. Phys. **137**, 064506 (2012), ISSN 1089-7690, URL http://www.ncbi.nlm.nih.gov/pubmed/22897292.

[59] A. D. Fortes, I. G. Wood, M. Alfredsson, L. Vočadlo, K. S. Knight, W. G. Marshall, M. G. Tucker, and F. Fernandez-Alonso, High Press. Res. **27**, 201 (2007), ISSN 0895-7959, URL http://www.tandfonline.com/doi/abs/10.1080/08957950701265029.

[60] A. D. Fortes, I. G. Wood, L. Vočadlo, K. S. Knight, W. G. Marshall, M. G. Tucker, and F. Fernandez-Alonso, J. Appl. Crystallogr. **42**, 846 (2009), ISSN 0021-8898, URL http://scripts.iucr.org/cgi-bin/paper?S0021889809027897.

[61] J. S. Loveday, R. J. Nelmes, C. L. Bull, H. E. Maynard-Casely, and M. Guthrie, High Press. Res. **29**, 396 (2009), ISSN 0895-7959, URL http://www.tandfonline.com/doi/abs/10.1080/08957950903162057.

[62] G. I. G. Griffiths, A. D. Fortes, C. J. Pickard, and R. J. Needs, J. Chem. Phys. **136**, 174512 (2012), ISSN 1089-7690, URL http://www.ncbi.nlm.nih.gov/pubmed/22583254.

[63] C. Giacovazzo, *Fundamentals of Crystallography - Third Edition* (Oxford University Press, 2011), chap. 1 Section 1.3.

[64] N. W. Ashcroft and N. D. Mermin, *Solid State Physics* (Brooks/Cole, 1976), chap. 4, ISBN 0-03-083993-9.

[65] C. Giacovazzo, *Fundamentals of Crystallography - Third Edition* (Oxford University Press, 2011), chap. 1 Section 1.5.

[66] C. Giacovazzo, *Fundamentals of Crystallography - Third Edition* (Oxford University Press, 2011), chap. 1 Section 1.9.

[67] T. Hahn and A. Looijenga-Vos, *International Tables for Crystallography - Vol. A* (Springer, 2006), chap. 2.1.

[68] N. W. Ashcroft and N. D. Mermin, *Solid State Physics* (Brooks/Cole, 1976), chap. 6, ISBN 0-03-083993-9.

[69] C. Giacovazzo, *Fundamentals of Crystallography - Third Edition* (Oxford University Press, 2011), chap. 2 Section 2.3.

[70] C. Giacovazzo, *Fundamentals of Crystallography - Third Edition* (Oxford University Press, 2011), chap. 3 Section 3.11.

[71] N. W. Ashcroft and N. D. Mermin, *Solid State Physics* (Brooks/Cole, 1976), chap. 5, ISBN 0-03-083993-9.

[72] C. Giacovazzo, *Fundamentals of Crystallography - Third Edition* (Oxford University Press, 2011), chap. 1 Section 1.4.

[73] C. Giacovazzo, *Fundamentals of Crystallography - Third Edition* (Oxford University Press, 2011), chap. 3 Section 3.12.

[74] H. L. Monaco and G. Artoli, *Fundamentals of Crystallography - Third Edition* (Oxford University Press, 2011), chap. 5 Section 5.3.2.

[75] C. Kittel, *Introduction to Solid Sate Physics- Eighth Edition* (John Wiley and Sons, 2004), chap. 2.

[76] M. Milanesio and D. Viterbo, *Fundamentals of Crystallography - Third Edition* (Oxford University Press, 2011), chap. 6 Section 6.1.

[77] M. Milanesio and D. Viterbo, *Fundamentals of Crystallography - Third Edition* (Oxford University Press, 2011), chap. 6 Section 6.3.

[78] M. Milanesio and D. Viterbo, *Fundamentals of Crystallography - Third Edition* (Oxford University Press, 2011), chap. 6 Section 6.4.

[79] M. Milanesio and D. Viterbo, *Fundamentals of Crystallography - Third Edition* (Oxford University Press, 2011), chap. 6 Section 6.5.

[80] C. Giacovazzo, *Fundamentals of Crystallography - Third Edition* (Oxford University Press, 2011), chap. 2 Section 2.13.1.

[81] Bruker AXS Inc., *Smart* (2007).

[82] Bruker AXS Inc., *Rlatt* (2007).

[83] Bruker AXS Inc., *Saint* (2007).

[84] G. M. Sheldrick, *Xprep* (2001).

[85] G. M. Sheldrick, Acta Crystallogr. **A64**, 112 (2008).

[86] A. Altomare, G. Cascarano, C. Giacovazzo, A. Guagliardi, M. C. Burla, G. Polidori, and M. Camalli, J. Appl. Crystallogr. (1994).

[87] L. J. Farrugia, J. Appl. Crystallogr. (1999).

[88] A. P. Hammersley, S. O. Svensson, M. Hanfland, A. N. Fitch, and D. Häusermann, High Press. Res. **14**, 235 (1996).

[89] J. Taylor, O. Arnold, J. Bilheaux, A. Buts, S. Campbell, M. Doucet, N. Draper, R. Fowler, M. Gigg, V. Lynch, et al., B. Am. Phys. Soc. **57** (2012).

[90] C. Giacovazzo, *Fundamentals of Crystallography - Third Edition* (Oxford University Press, 2011), chap. 2 Section 2.13.

[91] A. Larson and R. Von Dreele, Los Alamos Nat. Lab. Report pp. 86–748 (2004).

[92] B. Toby, J. Appl. Crystallogr. **34**, 210 (2001).

[93] J. Rodrguez-Carvajal, Physica B: Cond. Matt. **192**, 55 (1993).

[94] V. Favre-Nicolin and R. Černý, J. Appl. Crystallogr. **35**, 734 (2002), ISSN 0021-8898, URL http://scripts.iucr.org/cgi-bin/paper?S0021889802015236.

[95] V. Favre-Nicolin and R. Černý, Z. Kristallogr. **219**, 847 (2004), URL http://www.oldenbourg-link.com/doi/abs/10.1524/zkri.219.12.847.55869.

[96] S. Klotz, J. M. Besson, G. Hamel, R. J. Nelmes, and J. S. Loveday, App. Phys. Lett. **66**, 1735 (1995).

[97] H. L. Monaco and G. Artoli, *Fundamentals of Crystallography - Third Edition* (Oxford University Press, 2011), chap. 5 Section 5.2.1.

[98] H. L. Monaco and G. Artoli, *Fundamentals of Crystallography - Third Edition* (Oxford University Press, 2011), chap. 5 Section 5.2.3.

[99] H. L. Monaco and G. Artoli, *Fundamentals of Crystallography - Third Edition* (Oxford University Press, 2011), chap. 5 Section 5.2.2.

[100] Diamond Light Source 2013 Ltd., *Diamond light source - technology - components of the machine - injection system and linac:* (2013), online; accessed 20-September-2013, URL http://www.diamond.ac.uk/Home/Technology/Components/linac.html#.

[101] Diamond Light Source 2013 Ltd., *Diamond light source - technology - generating the electron beam:* (2013), online; accessed 20-September-2013, URL http://www.diamond.ac.uk/Home/Technology/beam.html.

[102] P. J. Duke, *Synchrotron radiation : production and properties* (Oxford University Press, 2000), chap. 8.

[103] Diamond Light Source 2013 Ltd., *Diamond light source - technology - components of the machine - booster synchrotron:* (2013), online; accessed 20-September-2013, URL http://www.diamond.ac.uk/Home/Technology/Components/booster.html.

[104] Diamond Light Source 2013 Ltd., *Diamond light source - technology - key machine parameters:* (2013), online; accessed 20-September-2013, URL http://www.diamond.ac.uk/Home/Technology/Parameter.html.

[105] P. J. Duke, *Synchrotron radiation : production and properties* (Oxford University Press, 2000), chap. 5.

[106] P. J. Duke, *Synchrotron radiation : production and properties* (Oxford University Press, 2000), chap. 13.

[107] P. J. Duke, *Synchrotron radiation : production and properties* (Oxford University Press, 2000), chap. 14.

[108] Diamond Light Source 2013 Ltd., *Diamond light source - beamlines:* (2013), online; accessed 20-September-2013, URL http://www.diamond.ac.uk/Home/Beamlines.html.

[109] Diamond Light Source 2013 Ltd., *Diamond light source - beamlines - i15 - extreme conditions - beamline layout:* (2013), online; accessed 20-September-2013, URL http://www.diamond.ac.uk/Home/Beamlines/I15/layout.html.

[110] C. G. Windsor, *Pulsed neutron scattering* (Taylor & Francis, 1981), chap. 2.

[111] Science and Technology Facilities Council, *Isis - how isis works - in depth:* (2013), online; accessed 20-September-2013, URL http://www.isis.stfc.ac.uk/about-isis/how-isis-works---in-depth4371.html.

[112] C. G. Windsor, *Pulsed neutron scattering* (Taylor & Francis, 1981), chap. 3.

[113] Science and Technology Facilities Council, *Isis - pearl technical information:* (2013), online; accessed 20-September-2013, URL http://www.isis.stfc.ac.uk/instruments/pearl/technical/pearl-technical-information7262.html.

[114] Science and Technology Facilities Council, *Isis - sxd technical information:* (2013), online; accessed 20-September-2013, URL http://www.isis.stfc.ac.uk/instruments/sxd/technical/sxd-technical-information7351.html.

[115] H. L. Monaco and G. Artoli, *Fundamentals of Crystallography - Third Edition* (Oxford University Press, 2011), chap. 5 Section 5.3.1.

[116] B. T. M. Willis, *Experimental neutron scattering* (Oxford University Press, 2009), chap. 3 Section 3.3.

[117] B. T. M. Willis, *Experimental neutron scattering* (Oxford University Press, 2009), chap. 3 Section 3.3.1.

[118] G. Cicognani, *The yellow book : Guide to neutron research facilities* (2008).

[119] Anon, *D9: Hot Neutron Four-Circle Diffractometer User Guide* (2013).

[120] Institut Laue-Langevin, *Ill :: Neutrons for science : Simulated experiment:* (2013), online; accessed 20-September-2013, URL http://www.ill.eu/instruments-support/instruments-groups/instruments/d9/how-it-works/simulated-experiment/.

[121] C. E. Weir, E. R. Lippincott, A. Van Valkenburg, and E. N. Bunting, J. Res. Nat. Bureau Stand., Sec. A-Phys. Chem. **63A**, 55 (1959).

[122] H. K. Mao, Y. Wu, L. C. Chen, J. F. Shu, and A. P. Jephcoat, J. Geophys. Res.-Sol. Ea. **95**, 21737 (1990).

[123] K. V. Kamenev, J. Sanchez-Benitez, and S. Tancharakorn, High Press. Res. **27**, 189 (2007).

[124] G. Shen, H. K. Mao, R. J. Hemley, T. S. Duffy, and M. L. Rivers, Geophys. Res. Lett. **25**, 373 (1998).

[125] L. Merrill and W. A. Bassett, Rev. Sci. Instrum. **45**, 290 (1974), URL http://ieeexplore.ieee.org/xpls/abs_all.jsp?arnumber=4980110.

[126] J. M. Besson, R. J. Nelmes, G. Hamel, J. S. Loveday, G. Weill, and S. Hull, Physica B: Cond. Matt. **181**, 907 (1992), URL http://www.sciencedirect.com/science/article/pii/092145269290505M.

[127] J. M. Besson and R. J. Nelmes, Physica B: Cond. Matt. **213-214**, 31 (1995), ISSN 09214526, URL http://linkinghub.elsevier.com/retrieve/pii/092145269500055E.

[128] Institut Laue-Langevin, *Ill :: Neutrons for science : Simulated experiment:* (2013), online; accessed 20-September-2013, URL http://www.ill.eu/?id=11239.

[129] R. A. Forman, G. J. Piermarini, J. D. Barnett, and S. Block, Science **176**, 284 (1972), URL http://www.sciencemag.org/content/176/4032/284.short.

[130] J.-P. Poirier, *Introduction to the Physics of the Earth's Interior* (Cambridge University Press, 1991), chap. 4 Section 4.1.

[131] J.-P. Poirier, *Introduction to the Physics of the Earth's Interior* (Cambridge University Press, 1991), chap. 4 Section 4.3.

[132] O. Schulte and W. B. Holzapfel, Phys. Rev. B **52**, 10 (1995), URL http://prb.aps.org/abstract/PRB/v52/i17/p12636_1.

[133] D. J. Dunstan, Rev. Sci. Instrum. **60**, 3789 (1989), URL http://ieeexplore.ieee.org/xpls/abs_all.jsp?arnumber=4987752.

[134] E. C. Jameson, *Electrical Discharge Machining* (Society of Manufacturing, 2001), chap. 1, ISBN 0-03-083993-9.

[135] R. J. Hemley, A. P. Jephcoat, H. K. Mao, C. S. Zha, L. W. Finger, and D. E. Cox, Nature **330**, 737 (1987).

[136] J. S. Loveday and R. J. Nelmes, High Press. Res. **23**, 41 (2003), ISSN 0895-7959, URL http://www.tandfonline.com/doi/abs/10.1080/0895795031000109698.

[137] P. Loubeyre, R. LeToullec, E. Wolanin, M. Hanfland, and D. . Häusermann, Nature **397**, 503 (1999), URL http://www.nature.com/nature/journal/v397/n6719/abs/397503a0.html.

[138] J. S. Loveday, M. I. McMahon, and R. J. Nelmes, J. Appl. Crystallogr. **23**, 392 (1990), URL http://scripts.iucr.org/cgi-bin/paper?S0021889890005635.

[139] J. E. Bertie and M. R. Shehata, J. Chem. Phys. **83**, 1449 (1985), ISSN 00219606, URL http://link.aip.org/link/JCPSA6/v83/i4/p1449/s1&Agg=doi.

[140] A. F. Goncharov, R. J. Hemley, and H.-k. Mao, J. Chem. Phys. **134**, 174501 (2011), ISSN 1089-7690, URL http://www.ncbi.nlm.nih.gov/pubmed/21548693.

[141] C. W. F. T. Pistorius, E. Rapoport, and J. B. Clark, J. Chem. Phys. **48**, 5509 (1968), ISSN 00219606, URL http://link.aip.org/link/?JCP/48/5509/1&Agg=doi.

[142] T. C. Swinney and D. F. Kelley, J. Phys. Chem. **95**, 2430 (1991), ISSN 0022-3654, URL http://pubs.acs.org/doi/abs/10.1021/j100159a058.

[143] R. J. Angel, Rev. Mineral. Geochem. **41**, 35 (2000).

[144] J. I. Lunine and D. J. Stevenson, Icarus **70**, 61 (1987), ISSN 00191035, URL http://linkinghub.elsevier.com/retrieve/pii/0019103587900753.